The University Of Sheffield.

Analog Frontend Circuits for Avalanche Photodiodes

S M Akeel AUCKLOO

Department of Electronic and Electrical Engineering
University of Sheffield

A thesis submitted for the degree of
Doctor of Philosophy
October 2016

Acknowlegments

I would like to thank my supervisors Professor John David, Professor Richard Tozer and Professor Chee Hing Tan for their continuous and extensive support during this process. The work presented in this thesis was only possible because of their patience, guidance and financial support.

I extend my gratitude to Dr Jo Shien Ng for her constant encouragements, comments and suggestions on my X-ray work.

I am grateful to Dr Simon Dimler for sharing his expertise on analog electronics and for his help during various stages of this work.

I would like to thank Dr James Green for the hours of discussions, comments and suggestions on my work.

I would like to acknowledge J.S Cheong for providing me with the AlInP APDs and Dr. Xinxin Zhou for packaging the APDs used in this work.

Finally, I would have been unable to get to this stage in life without the continuous and unwavering support of my parents.

Abstract

The aims of this work is to design low noise electronics for optical sensing and X-ray spectroscopy using Sheffield-grown Avalanche photodiodes(APD).

A transimpedance amplifier(TIA) for a 2.0 µm LIDAR system is designed and tested as part of a project funded by ESA. Numerical analysis is provided for the TIA in addition to SPICE and experimental analysis. Characterisation of the TIA shows that a noise equivalent power of less than 100 fW/√Hz can be achieved with an optimised InAs APD. Preliminary results of a TIA-InAs module at 2.0 µm is presented.

A low noise charge sensitive preamplifier(CSP) with a novel local feedback is designed and characterised. The CSP shows a better noise performance than commercially available CSP such as the CoolFet 250. The CSP is also characterised for APD dark current of up 4 µA and the CSP is found to behave well for such relatively high dark current. Discrepancies between the SPICE model and measured characteristic of the CSP's input JFET is presented and discussed.

The first ever Aluminium Indium Phosphide (AlInP) APD X-ray spectroscopy measurement is presented in this work. $\mathrm{Al_{0.52}In_{0.48}P}$ is the widest band material that can be grown lattice-matched on a GaAs substrate. Due to its wide bandgap, AlInP can offer reverse dark current of less than $2\ \mathrm{pA}$ at gain of 100 for a $200\mu\mathrm{m}$ device, making it desirable for room temperature operation. An energy resolution of 647 eV is obtained for AlInP APD coupled to the CSP and exposed to ^{55}Fe X-rays.

Using the CSP presented in this work, previously reported GaAs/AlGaAs APD is characterised and compared with results obtained using a commercial CSP. A 21% improvement in X-ray energy resolution is reported, despite degradation in the APD.

Publications

- **A Auckloo**, R Tozer, J David, Chee Hing Tan, “A low noise op-amp transimpedance amplifier for LIDAR applications”, 21st IEEE International Conference on Electronics, Circuits and Systems (ICECS), pp.590,593, 7-10 Dec. 2014. /10.1109/ICECS.2014.7050054

- **A. Auckloo**, J.S Cheong, X Meng, C H Tan, J S Ng, A. Krysa, R.C Tozer and J.P.R David, “$Al_{0.52}In_{0.48}P$ avalanche photodiodes for soft X-ray spectroscopy”, Journal of Instrumentation, IOP.

- J. S. Cheong, **A. Auckloo**, J. S. Ng, A. B. Krysa, and J. P. R. David, “A High Sensitivity Detector for Underwater Communication Systems”, Conference on Unmanned/Unattended Sensors and Sensor Networks XI; and Advanced Free-Space Optical Communication Techniques and Applications, SPIE, France 2015.

- Jo Shien Ng, Xinxin Zhou, **Akeel Auckloo**, Benjamin White, Shiyong Zhang, Andrey B. Krysa, John P. R. David, Chee Hing Tan, “High sensitivity InAs photodiodes for mid-infrared detection” Electro-Optical Remote Sensing, SPIE 2016 (Invited Paper).

Table of Contents

Acronyms

AlInP	Aluminium Indium Phosphide
APD	Avalanche Photodiode
CSP	Charge Sensitive Preamplifier
CV	Capacitance Voltage
IV	Current Voltage
ENC	Equivalent Noise Charge
JFET	Junction Field Effect Transistor
BJT	Bipolar Junction Transistor
NEP	Noise Equivalent Power
PCB	Printed Circuit Board
SAM-APD	Separate Absorption and Multiplication Layer Avalanche Photodiode
SMU	Source Measure Unit.
SPICE	Simulation Program with Integrated Circuit Emphasis.
TIA	Transimpedance Amplifier.
Si	Silicon.
InAs	Indium Arsenide
Ge	Germanium
Opamp	Operational Amplifier
LIDAR	Light Detection And Ranging

Chapter 1 Introduction

The use of semiconductor detectors is becoming more popular in industrial applications due to their superior performance, low cost and usability compared to well-established and commonly used detectors such as photomultiplier tubes. Telecommunication, imaging and spectroscopy are the key application areas serving as the catalyst to the development of faster and low noise semiconductor detectors. Compound semiconductors provide the flexibility to engineer detectors to meet specifications for a given application. Speed, collection efficiency and spectral response are among the properties that can be optimised to adapt to the particular applications. For instance, in a Light detection and ranging (LIDAR) system, the detector would be optimised for speed and low light detection while for X-ray spectroscopy, high collection efficiency, to allow more collection of X-ray photons in a short time, is important. However, for virtually all applications, low noise front-end circuits are needed to condition and amplify the signals from the semiconductor detectors. A panoply of commercial front-end circuits is available but they are usually designed to work for a wide range of detectors, bandwidth and gain; meaning that they are often not optimised to match the detector characteristics or application specifications. As semiconductor detectors improve in terms of noise characteristic, the noise of the front-end electronics is often found to be the limiting factor.

The aims of the work described in this thesis were to:

(a) design a very low noise pre-amplifier that can be configured to match the detectors for soft X-ray spectroscopy.

(b) Improve the energy resolution of X-ray detection by combining low noise amplifiers with avalanche photodiodes (APDs)

(c) demonstrate a very low noise, high bandwidth and high gain amplifier for LIDAR.

1.1 LIDAR

Optical remote sensing techniques have been used in the last decade or so, in atmospheric research [1]. LIDAR, along with radar, is one of the key methods used to profile the atmosphere. LIDAR can cover ranges exceeding hundreds of kilometres, allowing the possibility for researchers to observe the atmosphere from ground level. Atmospheric constituents interact with light from a LIDAR system in various ways so that the basic atmospheric variables, such as temperature, pressure as well as measurement of aerosols and other particulates, can be determined.

The principle of LIDAR dates back to the 1930s before the discovery of lasers. The scattering intensity of searchlight beams on the upper atmosphere helped to measure air density profiles [2-4]. The height information was measured by scanning the continuous light beam with the help of a telescope. In 1938, researchers used pulses of light for the first time using a setup in which height information was obtained by measuring the round-trip time between the emitted and detected light pulses, forming the basis of modern LIDAR systems [5]. The use of searchlights was a common practice in the 1960s before pulsed lasers were developed. Hulbert reported some of the earliest atmospheric remote sensing using searchlights [6]. He describes photographing a searchlight beam, shone towards the sky, from a station located roughly 20 km away. The development of Q-switching by McClung and Hellwarth encouraged the advancement and use of lasers instead of searchlights [7]. McClung and Hellwarth generated short, pulses of laser energy using an optical ruby maser. After these successes in ground-based LIDAR, NASA carried out the first airborne LIDAR measurement in 1967 on-board a T-33 aircraft. Standford Research Institute airborne LIDAR project was carried out to perform lower tropospheric aerosol measurements in 1969 [8].

After the successes of early airborne LIDAR missions, it was clear that a spaceborne LIDAR system would provide enormous contribution to the scientific world. In the 1970s and 1980s, NASA and ESRO (now known as ESA) started research on the feasibility of satellite-based LIDAR system. The early LIDAR systems were found to be too heavy and had too high power requirement for a satellite. NASA and ESA have since funded various

technical feasibility studies, including some of the work reported in this thesis [9-16].

A LIDAR system consists of a transmitter and a receiver as in a conventional RADAR system. The transmitter emits a pulse of light with a selected wavelength which interacts with gas molecules, particles or any object in its path. A fraction of the light is absorbed or scattered by this interaction, with the backscatterred light commonly collected by a detector at the receiver. Since photons travel at the speed of light, the round trip time can be used to calculate the distance between the LIDAR system and the scattering gases or particles [17]. In addition, the intensity of the backscatterred light provides information on the concentration of the gas molecules. At the receiver, an optical filter is usually employed to reject background photons or sunlight to improve the system signal to noise ratio. Although there are significant potential applications for LIDAR, routine use of LIDAR technology has been limited until recently. In the last decade or so, NASA and ESA have made considerable use of LIDAR technologies for atmosphere and space exploration [18-21]. This has pushed the technology into the consumer market with car manufacturers offering auto-braking systems and self-parking/driving, which is partially made up of a LIDAR system, in their latest vehicles [22, 23].

In recent years, ESA and NASA, and other organisations have been developing LIDAR systems for carbon dioxide active remote sensing [24-31]. 1.6 μm and 2.0 μm LIDAR system are of special interest due to distinctive absorption lines for CO_2 at these wavelengths [32]. At the wavelength of 1.6 μm LIDAR systems can provide acceptable sensitivity when used with optimised APDs or photomultiplier tubes (PMTs). In a LIDAR system, sensitivity is the minimum acceptable value of received power needed to achieve an acceptable signal-to-noise ratio or performance. On the other hand at 2.0 μm, better CO_2 measurements can be achieved due to more than one order of magnitude stronger absorption lines at this wavelength. However, due to the limited availability of high sensitivity detectors operating at 2.0 μm, CO_2 LIDAR systems operating at this wavelength remains a challenge. An InGaAs pin detector was used in [33] but poor performance was obtained due to limitations in the detector's sensitivity. To overcome detectors' limitations, heterodyne detection have been developed but this increases the complexity and cost of such systems [24, 34]. Direct

detection using high performing detectors at 2.0 μm remains desirable and extensive research efforts are focused on developing LIDAR receivers for this wavelength. Lasers operating at this range of wavelength are also attractive as they are often deemed "eye-safe", making them suitable for open-air applications such as range-finding and military targeting in addition to atmospheric probing [35].

LIDAR has a significant advantage in some applications where RADAR is still used but the LIDAR technology is being held back due to the safety issues around the use of pulsed power laser transmitters that is capable of causing injury to the human vision system. The use of low power lasers for a LIDAR system is proposed in [36] but the use of PMT in the receiver makes the proposed system bulky. PMTs are fragile in comparison with solid-state alternatives and often require extensive cooling in order to operate with reasonable performance. For instance, the voltage divider circuit in a PMT draws continuous current which is converted to resistive heat. Moreover, to operate at high gain, they require high voltages, several hundreds and even up to 1 kV. In PMT operation, even a slight magnetic field can affect the trajectories of low-energy electrons travelling along a long path, causing variation in sensitivity on the anode. More crucially the quantum efficiency of PMT is considered low, with only 10-25 % of incident photons generating photoelectrons at the photocathode and not available at the wavelength of 2 μm.

Compound semiconductor APDs, on the other hand, are much smaller in size and are more physically robust than PMTs. APDs can operate at equivalently high gain with lower applied bias voltages. They also have the flexibility to be designed to be more responsive to a particular wavelength which makes them suitable for LIDAR receivers. The quantum efficiency of APDs ranges from 50-90 % and they are virtually insensitive to magnetic field. InAs has a bandgap of 0.35 eV and provides excellent detection efficiency at 2 μm. Sheffield-grown InAs APDs have shown quantum efficiencies of 70 % at 2.0 μm and high gain [37, 38], making them potentially suitable for a LIDAR receiver. The detector's leakage current can however lead to unacceptably high noise at room temperature but this problem can be overcome with moderate cooling. The low value of shunt resistance of InAs detectors can also be a problem in interfacing them with front-end amplifiers. The low shunt

resistance can lead to a high voltage gain in the amplifier. This can, in some cases, cause an undesirable DC offset voltage at the amplifier's output if the amplifier's input offset are high.

Despite all the challenges associated with InAs, there is a strong motivation to develop an InAs LIDAR receiver. Commercial amplifiers do not often have the desired input characteristics needed and do not offer the flexibility and ease of integrating the detectors close to and/or in the same package. There is a strong motivation to develop a front-end amplifier to match the operating characteristics and conditions of InAs, such as being cooled to sub-zero temperatures.

The amplifier presented in this work was designed and built as part of a European Space Agency contract. It is meant to be coupled to an InAs APD grown and fabricated in Sheffield and operated at a wavelength of 2 μm and cooled to 200 K.

1.2 X-ray applications

German physicist Wilhelm Röntgen first discovered and applied X-ray radiography. He is well known to have X-rayed his wife's hand to produce the first "röntgenogram" [39]. X-rays have since become the norm in medical diagnostic applications. X-ray is also widely used in industrial applications and security, with body scanning now used in airports. X-ray crystallography is an area of application where crystal structures are determined by examining the diffraction pattern produced by X-rays colliding on the crystal. One of the first breakthroughs in X-ray crystallography pattern of DNA was carried out by Rosalind Franklin in 1952 [40]. Her data helped Francis Crick and James D. Watson to determine the correct description of the helical structure of DNA [41].

X-ray is also widely used for non-destructive spectroscopy. Soft X-ray spectroscopy is one of the effective methods to analyse electronic structure and atomic concentration for instance. Semiconductor detectors are often used for soft X-ray detection and spectroscopy, with Si and Ge dominating most applications compared to compound semiconductors due to their mature fabrication process and growth. Semiconductor X-ray detectors can offer better energy resolution in comparison to detectors such as gas-filled detectors as the number of charges created in a semiconductor can be substantially more

than charges created in other detectors. Semiconductor X-ray detectors can also be compact and insensitive to magnetic field.

X-ray spectrometers are widely used in planetary mission rovers and landers for analysing planetary surfaces [42-44]. Elemental composition of a rocky surface can be analysed using X-ray fluorescence analysis with a view to determine its history and formation. It is necessary that detectors are capable of resolving X-ray lines that will enable the identification of the major rock forming elements. A low energy limit to include magnesium (Kα = 1.25 keV) and aluminium (Kα = 1.49 keV) is highly desired [45]. An upper limit to include iron (Kα = 6.4 keV) is required along with a spectral resolution sufficient to separate the low energy magnesium and aluminium lines. Ideally ~ 150 eV FWHM at 1.5 keV is needed to separate and resolve the magnesium and aluminium spectral lines.

As with LIDAR, APDs can be used to improve the signal to noise ratio. One of the first reported use of APDs for the detection of 5.9 keV X-rays was by Webb and McIntyre [46], with most of the work focused on analysing the effect of avalanche noise of the devices on the energy resolution. Squillante *et al.* presented the detection of 5.9 keV soft X-ray with a Si APD, and a FWHM of 590 eV is reported [47]. Low noise APDs which enabled the detection of low energy X-rays (< 10 keV) were demonstrated in [48] using a Si APD with a bevelled edge design. Extensive studies on bevelled edge devices manufactured by Advance Photonix were also carried out by Moszynski *et al.* [49, 50]. However, due to its low atomic number, Si suffers from low detection efficiency.

Compound semiconductors like CdTe and GaAs have been investigated as alternatives to Si for soft X-ray detection. CdTe is a popular compound semiconductor X-ray detector that provides high detection efficiency due to its high atomic number (48 for Cd and 52 for Te). GaAs has also shown promising results for X-ray detection. III-V semiconductor compounds such as GaAs are also at least two orders of magnitude more radiation-hard than hardened Si. An ideal X-ray detector needs to have high energy resolution, good detection efficiency, large active volume and have the capability to operate at room temperature.

For room temperature soft X-ray detection, wide bandgap semiconductors are preferable due to their lower dark current when compared to narrow bandgap material such as InAs for instance. Despite this, the dark current can still play a significant role in the measured energy resolution. The work reported here does not involve semiconductor optimisation but there is however scope to reduce the noise contribution down the measurement chain, namely the electronics. The main motivation behind this work, is to design a low noise preamplifier that provides the flexibility to match detectors with a wide range of capacitances and dark current to the input of the preamplifier. Commercial front-end amplifiers such as the CoolFet from Ametek can provide adequate performance but they do not provide much flexibility in matching the detectors' characteristics with the input characteristics of the amplifier.

1.3 Structure of the thesis

This thesis reports the design of two front-end amplifiers, one for LIDAR applications and one for X-ray detection, as well as characterisation of wide bandgap compound semiconductors AlInP and AlGaAs APDs for X-ray detection. Design procedures and experimental measurements are presented. The motivation for this work has been discussed in this chapter and progress in the respective areas is also presented.

Chapter 2 provides a review of front-end amplifiers for both LIDAR and X-ray detection. Different circuit topologies are presented and reviewed. An overview of commonly used photodetectors is also presented and interactions processes of optical and X-ray photons with the detectors are described. A detailed breakdown of various noise sources in a typical X-ray detection system is described.

Chapter 3 details some of the measurements that are routinely performed on new diodes and circuits that are fabricated at Sheffield, including frequency response, X-ray spectroscopy, current-voltage, photo-multiplication and capacitance-voltage. Additionally, new measurements were specifically devised for this work.

Chapter 4 presents design methodology and compromises for a transimpedance amplifier that form part of a novel InAs LIDAR front-end. This work was carried out on a

contract with the European Space Agency. The performance of the transimpedance amplifier was assessed numerically and experimentally. The work described, was presented at the 21st IEEE International Conference on Electronics Circuits and Systems. Part of this work were also presented at the Electro-Optical Remote Sensing conference, SPIE 2016 (Invited Paper). The transimpedance amplifier were used to charaterised AlInP photodiodes and the results were presented at the conference on Unmanned/Unattended Sensors and Sensor Networks XI; and Advanced Free-Space Optical Communication Techniques and Applications in France, 2015. The main results presented at the conference is shown in section 10.4.

Chapter 5 presents a novel charge sensitive preamplifier, built with commercially available discrete components, for X-ray spectroscopy measurements. The use of local feedback within the circuit makes it more stable than the state-of-the-art circuits reported in literature. A journal paper is currently being drafted to be submitted to IEEE Transactions on Circuits and Systems.

Chapter 6 reports the first X-ray spectroscopy measurements performed on novel $p^+ - i - p^- - n^+$ AlInP APDs. A FWHM energy resolution of 647 eV was obtained. The circuits presented in chapter 5 were used to characterise the APDs. A journal paper on the work has been published in IOP, Journal of Instrumentation.

Chapter 7 reports improved measurements from SAM-APDs processed from the same wafer as those presented in [51] by Gomes *et. al*. Noise performance of the improved system is provided and compared. A letter is being drafted to be submitted to IEEE Electron Devices.

Chapter 8 provides conclusions that can be drawn from the work carried out in this thesis. Suggestions for future directions are given.

Chapter 2 Background Theory

The previous chapter gave an introduction on LiDAR and X-ray applications and this chapter presents background theories related to the topics of this thesis.

2.1 Review of front-end circuits

This section briefly reviews several of the electronic circuits commonly used as front-end signal conditioners for photon detectors. The objective of the review is to provide some context in common methods of signal conditioning and amplification for detectors. Front-end amplifiers that interface electronic systems with photon detectors can be split in two categories: Current-to-voltage converters and charge-to-voltage converters. Current-to-voltage converter can be further split into three groups and they are:

- Low impedance amplifiers
- High impedance amplifiers
- Transimpedance amplifiers

The names used to describe these topologies can be somewhat misleading. Front-end amplifiers for photon detectors fundamentally convert the detected photocurrent into a voltage, making their transfer functions transimpedance in nature. Each of these front-end topologies will be discussed briefly to highlight their properties.

2.1.1 Low impedance amplifiers

Low impedance optical amplifiers consist of a photodiode, a load resistor and a low input impedance voltage amplifier as illustrated in Figure 2.1.

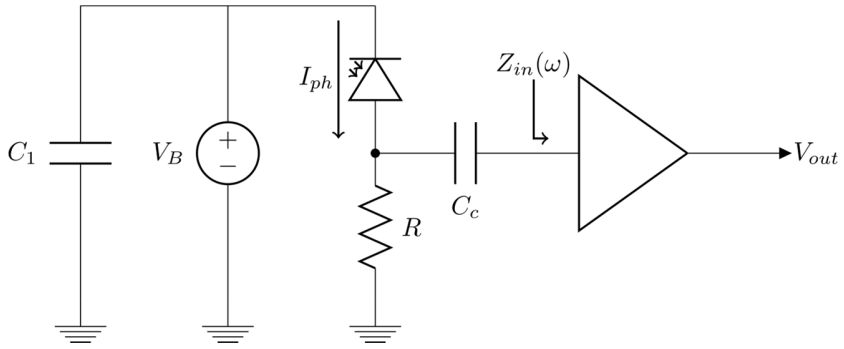

Figure 2.1: A generic AC-coupled low impedance amplifier

The load resistor R provides a path flow for the DC current and also create a voltage proportional to the photocurrent. A parallel combination of the input impedance $Z_{in}(\omega)$ and R is seen by the high-frequency components of the photocurrent. The low frequency components are blocked by the coupling capacitor C_c. C_1 is a decoupling capacitor for the bias source V_B. Commercially available wideband amplifiers are suitable for this application. They tend to be high bandwidth (in the GHz) and high gain with 50Ω input and output impedance [52].

In applications where the low-frequency components have important information, the photodiode is DC-coupled and the photodiode is loaded directly onto the input impedance $Z_{in}(\omega)$ as illustrated in Figure 2.2.

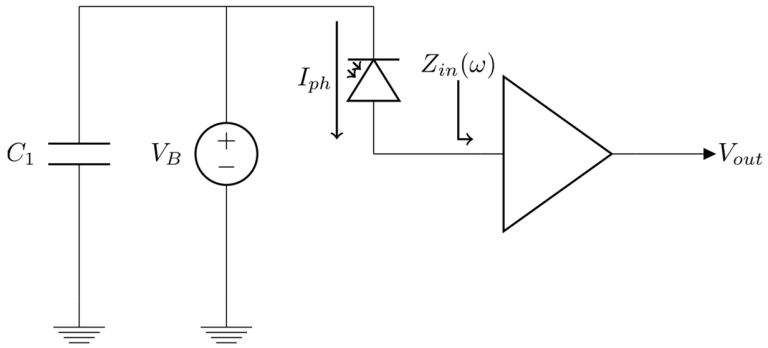

Figure 2.2: A generic DC-coupled low impedance amplifier

One of the advantages of the low-impedance topology is that the noise contribution due to the input impedance is lower than using a high impedance input amplifier for instance. Its simplicity and potentially high bandwidth makes it suitable for applications such as optical communication system. The input referred current noise is given by the thermal noise of the input resistance. For a 50Ω input impedance amplifier, the input referred current noise is $18\ pA/\sqrt{Hz}$ $\left(i_n = \sqrt{\frac{4kT}{R}}\right)$, where *k* Boltzmann's constant (1.38 × 10^{-23} J/K), *T* is the temperature in Kelvin (K), *R* is the resistance in ohms (50Ω in this case).

2.1.2 High impedance amplifiers

The high impedance amplifier was one of the first low-noise front-ends used in optical receivers and was originally based on vacuum tube amplifiers [53]. A generic high impedance amplifier is shown in Figure 2.3. A detector such as a PD or APD is connected to a resistor R and is reversed biased. When the detector is illuminated, a photo-current flows through resistor R and a voltage proportional to that photo-current appears across the resistor. The voltage developed across the resistor R is presented to an amplifier with an input impedance sufficiently large such that it does not load the detector-resistor network. The basic operating principle is to load the photocurrent with a large impedance (using a large value of R) in order to maximise the voltage developed at the input of the amplifier. The idea is that if the voltage is maximised, the effects of the amplifier noise sources will be reduced.

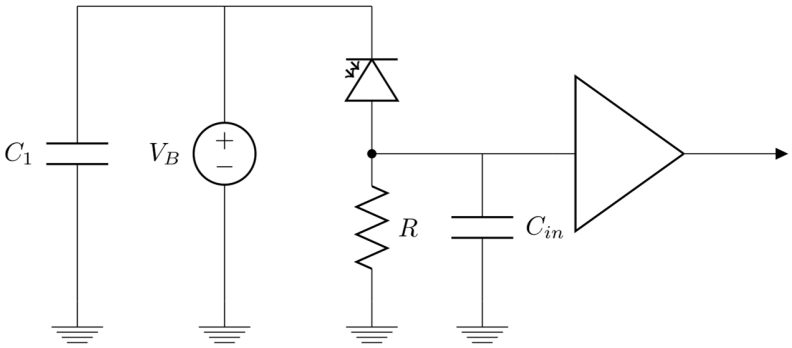

Figure 2.3: A generic high impedance amplifier

While this topology is simple, the low-frequency component is also amplified, introducing dynamic range constraints.

Another drawback with this topology is the fluctuation of the bias voltage across the detector due to the photo-current. Consider the detector-resistor combination as shown in Figure 2.4, with V_b fixed. Fluctuation in the power of the optical source on the detector will provide fluctuations in the photo-current and hence give rise to fluctuations in voltage across R and hence fluctuations in the voltage across the photodiode. Any fluctuations of bias voltage on an APD will lead to fluctuations in APD gain and hence any subsequent optical power falling on the APD will experience a modified gain.

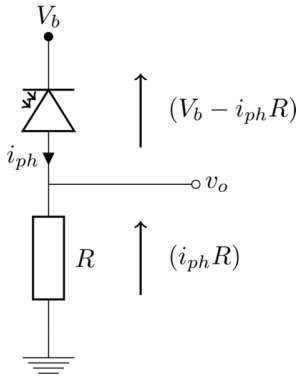

Figure 2.4: Detector-Resistor front-end

2.1.3 Transimpedance amplifiers

A generic opamp transimpedance amplifier (TIA) is shown in Figure 2.5. This topology is also sometimes called a shunt-shunt feedback TIA.

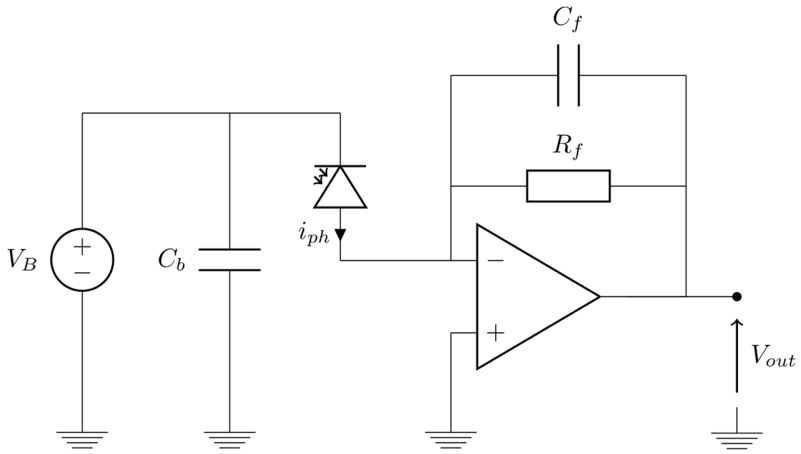

Figure 2.5: A generic opamp transimpedance amplifier

Operational amplifiers are often well suited for this application, requiring a few external components. The detector is connected to the inverting input which is held at virtual ground due to the grounded non-inverting input. The photo-current flows through the feedback resistor R_f leading to an output voltage equal to $\approx -R_f i_{ph}$. C_f provides compensation for the effects of the input node capacitance and stabilises the circuit.

Unlike for the high-impedance amplifier topology, the detector reverse bias voltage is almost independent of the photo-current for the TIA topology because the detector is loaded onto a virtual earth point. Opamp based TIA are also prone to instability with excess capacitance at the input, which can create excessive phase-shifts within the loop formed by the feedback network and the opamp. This can be analysed by plotting the frequency of the open-loop gain and the feedback factor β, illustrated in Figure 2.6. Consider a circuit without C_f and using a simplified equivalent circuit for the photodiode, the feedback network can be considered as a one-pole RC filter consisting of the feedback R_f and the total input capacitance on the inverting input. The reciprocal of the feedback factor is referred to as the noise gain.

The noise gain is given by:

$$\frac{1}{\beta(s)} = 1 + sR_f(C_T + C_f) \tag{2.1}$$

where C_T is the total capacitance on the inverting input of the opamp, consisting of the photodiode capacitance and the input capacitance.

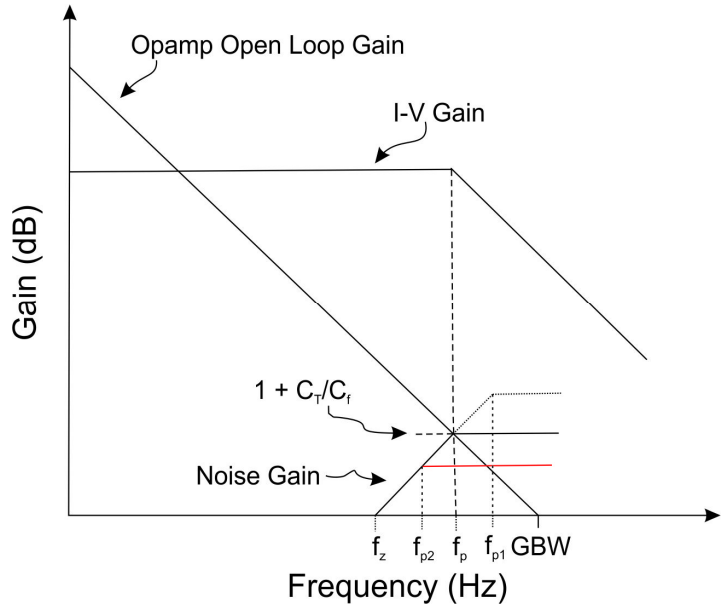

Figure 2.6: Bode Plot of Noise Gain Intersecting With Op Amp Open-Loop Gain

The rate of closure between the two curves can determine whether oscillation may occur and with the rate of closure, we can obtain the phase margin. If the rate of closure is 40 dB/dec, the TIA circuit will be unstable. Due to the inverting nature of the negative feedback, the phase shift of the feedback signal is 180° at low frequency. As frequency increases to the -20 dB/dec region of the Opamp Open loop gain, the opamp dominant pole will add phase margin of up to 90°. The pole introduced by the feedback path will also add a further 90° of phase shift. This will lead to a phase margin of 360° at $A\beta = 1$. From the Barkhausen stability criterion, with a phase margin of 360° at $A\beta = 1$, self-sustaining oscillation will results.

By using an appropriate value of C_f sufficient phase margin can be introduced to stabilise the circuit. The feedback capacitor C_f helps to maintain stability by creating a pole

f_p in the noise gain function, flattening the noise gain slope. This is illustrated in Figure 2.6. With the addition of C_f, a pole is introduced in the noise gain factor and the noise gain is given by:

$$\frac{1}{\beta(s)} = \frac{1+sR_f(C_T+C_f)}{1+sC_fR_f} \tag{2.2}$$

The modified noise gain has a zero at f_z given by:

$$f_z \approx \frac{1}{2\pi R_f(C_T+C_f)} \tag{2.3}$$

The optimum value of C_f is when the noise gain is equal to the opamp open loop gain at f_p. Excess capacitance at the input, C_T, will give a larger gain $1+\frac{C_T}{C_f}$, causing the pole to fall outside the open loop gain curve as illustrated by f_{p1} in Figure 2.6. If the slope of the open loop gain curve is -20dB/dec and the noise gain curve has a slope of 20dB/dec, the rate of closure will be 40dB/dec.

Overcompensating the feedback of a TIA, will create a pole inside the open loop gain curve, shown as f_{p2}, making the TIA unconditionally stable at the expense of reduced bandwidth.

Careful design of a TIA can provide a good compromise between stability, noise, bandwidth and gain. A concise review of other TIA topologies was carried out by Sackinger [54].

Front-end	Advantages	Drawbacks
Low impedance amplifier	Good dynamic Range	High noise contribution
	Simplicity	
	Commercially available microwave amplifier can be used	
High impedance amplifier	Thermal noise in the receiver is minimised.	Poor dynamic range
	Baseband receivers gives moderate bandwidth with the lowest obtainable noise.	Fluctuation in APD bias voltages.
Transimpedance amplifier	High bandwidth.	Stray capacitance affects bandwidth and stability.
	Response can be very stable with an optimally designed circuit.	Noisier than high-impedance but not as noisy as low impedance topology
	Receiver response can be very stable over time, temperature, etc. due to desensitizing nature of negative feedback.	

Table 2-1: Summary of optical front-end circuits

2.1.4 Charge sensitive preamplifiers (CSPs)

In X-ray spectroscopy, the energies of radiation events are detected by a semiconductor detector coupled to an analog front-end. A basic schematic is illustrated in Figure 2.7. The energy of X-ray photons is such that many electron-hole pairs are created in a photodiode for each X-ray photon – photodiode interaction. Since the photodiode is reverse biased, these carriers are swept out by the electric field in the photodiode causing a narrow current pulse in the external circuit. The current pulse contains the spectrographic information of interest. The photodiode can be either DC-coupled or AC-coupled to the CSP. Figure 2.7 shows a DC-coupled configuration.

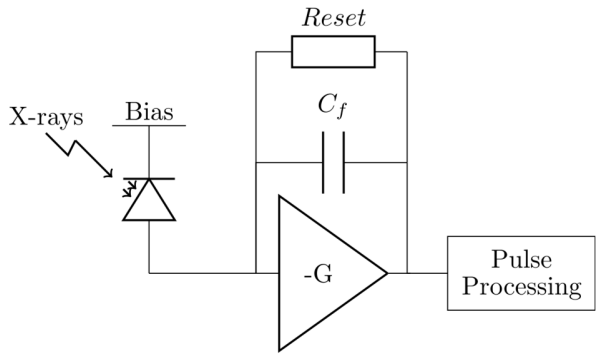

Figure 2.7: Schematic of a basic X-ray detection front-end

The signal from the detector can be considered as a Dirac current pulse with a pulse width in the region of several ns or less, as the collection time is very short for X-ray interactions [55, 56]. The time integral of the Dirac current pulse equals to the total generated charge *Q*. With the benefit of the high open loop gain of the CSP, the generated charge *Q* is integrated onto the feedback capacitor C_f giving rise to a step voltage having an amplitude of $\frac{Q}{C_f}$ at the CSP output. Ideally, the rise time should be equal to the photodiode current pulse width and not limited by the CSP. A reset mechanism is then applied to remove the charge on the capacitor C_f, assuring that the CSP is ready to collect subsequent current pulses from the photodiode. The easiest method of resetting is to include a resistor R_f in parallel with the feedback capacitor C_f, giving a decay time constant of $\tau = R_f C_f$ [56].

CSPs are widely used due their low noise performance and the input stage can be adapted to match the photodiode's specifications in order to reduce the total circuit noise. Further noise derivations are provided in the following sections. The gain of the a CSP-photodiode configuration is also insensitive to variations in the photodiode capacitance if the open-loop gain of the CSP is high. In addition to the use of a feedback resistor to reset the CSP, other methods have also been reported in literature [57-59]. The next few sections provide a concise review of the different reset methods.

2.1.4.1 **Charge Sensitive Preamplifier with a Feedback Resistor**

The most common and easiest way to build charge sensitive preamplifiers consists of a low noise preamplifier, often in the form of an operational amplifier, with a capacitor and a resistor making the feedback as illustrated in Figure 2.8.

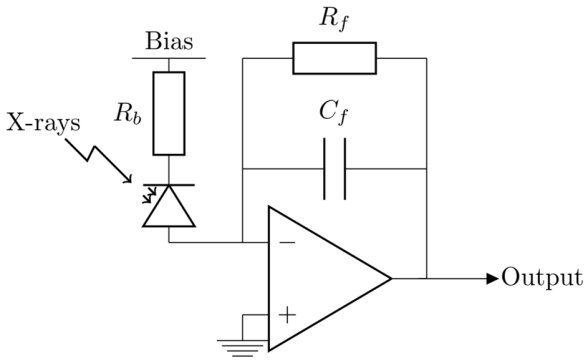

Figure 2.8: Simplified Schematic of a CSP with a feedback resistor

While Figure 2.8 shows that the detector is connected to a low input impedance virtual earth, the opamp itself has a high input impedance. The high input impedance of the preamplifier is usually achieved with an input FET. Current from the detector is integrated across the feedback capacitor C_f causing the voltage at the output to rise. The feedback resistor R_f, often referred to as a bleed resistor, discharges the capacitor at a decay rate given by $\tau = R_f C_f$. The resistor R_f also provides DC feedback to stabilise the operating points of the circuit and acts as a path for the leakage current from the detector. The voltage

created across the feedback resistor due to the detector's leakage current is a convenient way of monitoring that leakage. However, for high radiation count applications, there is insufficient time for C_f to fully discharge, meaning that there is always a voltage drop, that is not necessarily related to the leakage current, across R_f. To maximise the charge gain of the preamplifier, it is desirable to have a very small value of capacitance for C_f. For a high count rate, it is also important that the capacitor C_f discharges quickly after each radiation event in order to be ready for the next event. A low resistor value R_f is required to achieve a quick discharge but this is at the expense of increased noise contribution (discussed below). Various alterations of this topology, with the focus on the design of the operational amplifier, have been reported in literature. Implementation using both commercial opamps and CMOS designs is reported [60-65]. This topology of preamplifier is also available from companies such as Cremat [66] and Amptek [67]. However, the noise performance of this type of preamplifier is not low enough to provide acceptable energy resolution with a Sheffield-grown detector. The equivalent rms noise charge of those reported resistor-feedback preamplifiers ranges from 100 to a few 1000 electrons [60, 68-70].

The Johnson noise associated with the feedback resistor R_f appears directly at the output and makes a considerable contribution to the circuit total noise. The noise can be reduced by using a large value for R_f but this leads to longer time constant for the output voltage pulse tail. At high counting rate, a long time constant can lead to saturation of preamplifier output as the preamplifier cannot recover in time for successive input signals.

Alternative approaches such as pulsed optical feedback and transistor reset preamplifier do not require the resistive feedback and hence give a lower preamplifier noise.

2.1.4.2 **Transistor Reset Charge Sensitive Preamplifier**

To overcome the noise degradation due to the feedback resistor in a conventional charge sensitive preamplifier, researchers have devised and reported pulsed feedback system similar to the one illustrated in Figure 2.9 in a number of publications [58, 71-74].

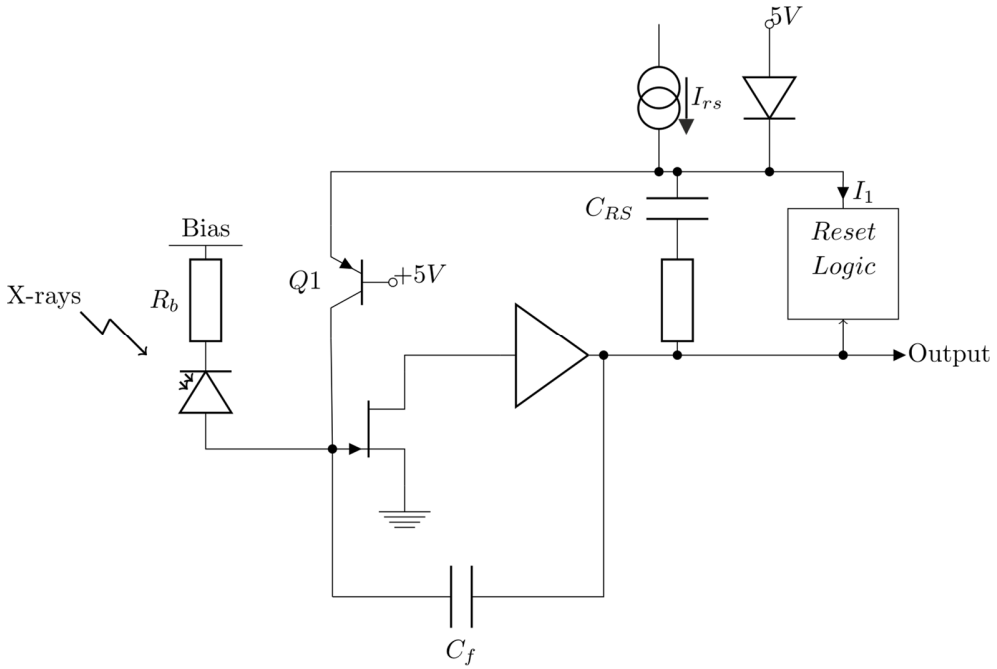

Figure 2.9: Simplified Schematic of a feedback-controlled transistor reset CSP. Redrawn from [58].

In this type of circuit, the output voltage level is sensed and when it exceeds an upper discriminator level, the reset logic circuit creates a path for the feedback capacitor C_f to discharge. Referring to Figure 2.9, during normal counting operation, charge from the detector is integrated across C_f. The reset circuit outputs a current I_1 which is larger than I_{rs}, clamping the emitter of $Q1$ to $+5V$ minus one diode drop. This puts $Q1$ in a non-conductive mode. When the output voltage reaches a level determined by an upper discriminator, I_1 is set to zero, allowing I_{rs} to flow in capacitor C_{rs} and thus raising the potential of the emitter of $Q1$. $Q1$ becomes conductive which allows a small portion of I_{rs} to flow through it, restoring the charge on the feedback capacitor C_f.

When the output voltage falls below a level determined by a lower discriminator, the current I_1 is restored and normal counting operation can resume. Variations of the circuit with a diode, that switches on and off to control the flow of current, instead of transistor $Q1$ is also proposed in [74].

A circuit that uses a field effect transistor instead of the pnp bipolar $Q1$ was proposed by Radeka [75] and the principle of operation is the same as discussed above.

Although this method of charge recovery is better than the conventional method in noise terms, there are still some noise components that are coupled to the input of preamplifier. The leakage current from $Q1$ and added capacitance at the input due to the reset transistor $Q1$ can cause some degradation in the signal-to-noise ratio. For high capacitance detectors, where the detector leakage current is substantial, the noise degradation due to this reset topology is negligible compared to conventional resistor feedback preamplifier.

2.1.4.3 **Pulsed Optical Feedback Preamplifier**

Pulsed optical feedback preamplifiers offer an advantage over transistor reset circuits as there is no physical circuit coupled to the input from the feedback. A simplified schematic of such circuit is illustrated in Figure 2.10.

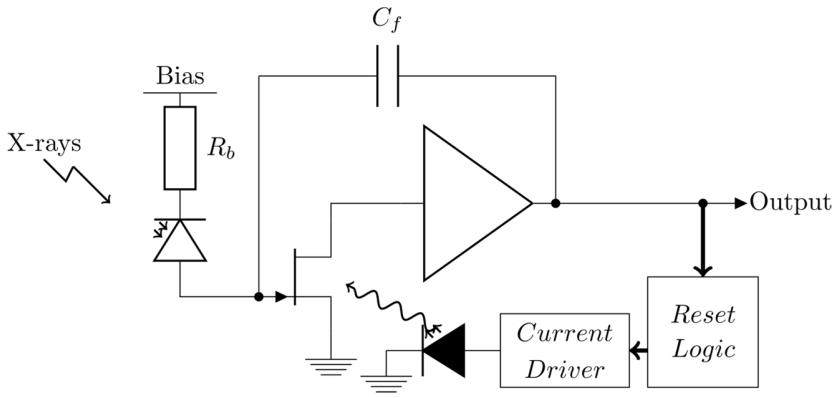

Figure 2.10: Simplified Schematic of a Pulsed Optical Feedback Charge Sensitive Preamplifier

Pulsed optical feedback can have a better noise performance over transistor reset CSP as stray capacitance at the input of the CSP is minimal [76]. The reset current only flows

during reset and thus no noise due to that current is introduced during normal counting mode. However, this circuit also have some drawbacks. The reset light can cause some after-effects in the FET and also in the detector if the detector is not properly shielded from the light. This can cause degradation in the energy resolution at high counting rate [77].

Like the transistor reset CSP, the output of the CSP is sensed by a reset logic circuit. When the output voltage exceeds an upper discriminator level, the current driver is turned on, firing the LED on. The light, which is directed onto the exposed input FET, causes the drain-gate junction to act as a photodiode. A substantial photocurrent then flows into the input FET's gate, discharging the feedback capacitor C_f at the same time. When the output voltage drops below a low discriminator level, the current driver is turned off and normal counting operation can resume [78, 79].

One of the major drawbacks of this system is the need to have an exposed input FET. When the detector is attached close to the FET and exposed to X-rays photons, they are also absorbed by the FET and this leads to spectra due to the detector and the FET. Goulding *et al.* also reported degradation in resolution for high counting rate [80]. Counting losses during the reset operation was also reported in [81].

2.1.4.4 **Forward-biased FET CSP**

In a conventional CSP consisting of a feedback resistor R_f, the thermal noise due to that resistor can be negligible compared to the shot noise associated with the leakage current of the detector and the input FET if an appropriate value of R_f is chosen [57]:

$$R_f > \frac{2kT}{q(I_d+I_f)} \tag{2.4}$$

where k is the Boltzman constant, T is the temperature in Kelvins and q is the electron charge. As already discussed in sections above, R_f can still limit the maximum signal-to-noise ratio of a high resolution spectroscopy system. Removing the feedback resistor altogether without adding any further reset circuit to the input can help achieve the lowest possible noise but it can be difficult to control the circuit bias conditions in the absence of an R_f.

A drain feedback method whereby the drain voltage is regulated according to the

input energy count-rate product is proposed in [82]. This method makes use of impact ionisation in the pinch-off channel region of the input FET. As the incoming photon flux absorbed by the detector increases, the output voltage also increases and this is supplied to the drain voltage of the input FET. This will cause avalanche generation in the FET which will help to restore the charges deposited on the feedback capacitor. In this mode of operation, the drain voltage cannot be adjusted independently and circuit behaviour is dependent on the FET characteristic. The critical drain voltage that causes impact ionisation will vary for different FETs, setting limitations of this type of circuit.

Radeka [83] proposed a circuit that uses the forward conduction of the gate-to-channel path of the input FET. Current pulses are applied to the input to periodically forward bias the gate-to-channel junction which allows the charge deposited after radiation events to be removed from the feedback capacitor. The frequency and amplitude of the current pulses needed are dependent on the FET characteristics and the radiation count rate. Thus it is difficult to achieve a reliable "out-of-the-box" design using this topology.

The method proposed by Bertuccio *et al.* removes almost all the need for adjusting the circuit prior to use [57]. In the proposed circuit, the gate-to-channel junction of the input n-channel JFET is always forward biased. A detector is connected in such a way that its leakage current flows into the gate towards the source as illustrated in Figure 2.11, forcing the input n-channel JFET to operate in a forward bias mode. The voltage at the preamplifier input is then a function of the current flowing through the gate to source diode. The random fluctuation of the current flowing through the gate to source diode will create an independent noise contribution, however the noise contribution is lower than other methods as no additional circuitry is coupled to the input. An ENC of 17 e^- r.m.s is reported at shaping time of 0.5 μs. This circuit has proven to give good energy resolution with silicon detectors [84, 85].

The circuit could in principle also be used with an input p-channel JFET and the detector is connected such that its leakage current flows away from the gate. P-channel JFETs that match n-channel JFETs characteristic and performance are not readily available. N-channel JFETs have a superior performance as for instance, the transit time of electrons

through the channel is a third of the transit time for holes, making the series noise lower by a factor of $\sqrt{3}$ compared to a p-channel JFET with the same dimensions[86]. P-channel JFETs are thus an unattractive option in this application. Due to the way that detectors are sometimes packaged, it might be difficult to connect them in such a way that allows the leakage current to flow into the gate. A modified circuit, with a n-channel JFET and an external forward-biased p-n diode connected between the gate of the JFET and ground, and based on [57], is proposed in [86] to avoid the use of a p-channel JFET.

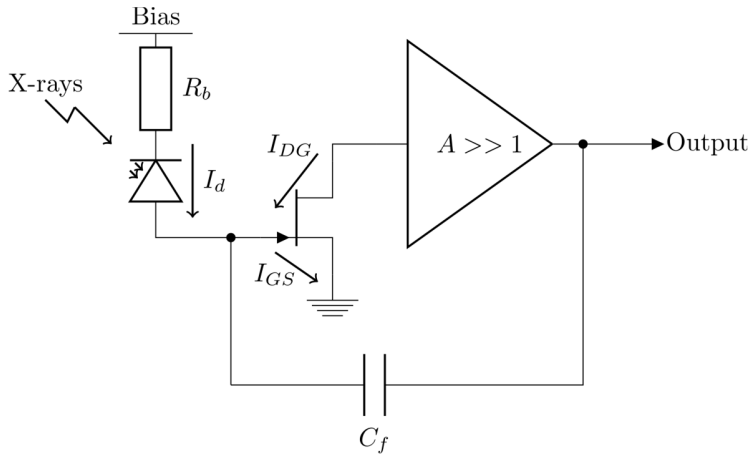

Figure 2.11: Simplified Schematic of a CSP with a forward-biased FET

Topology	Advantages	Drawbacks
CSP with feedback resistor	Simplicity.	High noise contribution.
	Good circuit stability	
	Commercially opamp can be used.	
Transistor Reset CSP	Better noise performance than Resistor Feedback CSP	Reset transistor can cause degradation in SNR.
Pulsed Optical Feedback CSP	Good noise performance	Exposed FET
Forward-biased FET CSP	Good noise performance	Relies on specific DC working points, making it challenging to replace the FET with different models.
	Simple to use, with minimum tinkering	

Table 2-2: Comparison of charge sensitive preamplifiers topologies

2.2 Review of Electro-optical detectors

2.2.1 Photomultiplier

Thermionic valves, particularly photomultiplier, were used to detect light prior to the discovery of the optical capability of semiconductors. Photomultiplier tubes fulfil similar applications to Avalanche photodiodes. A schematic of a photomultiplier tube is shown in Figure 2.12.

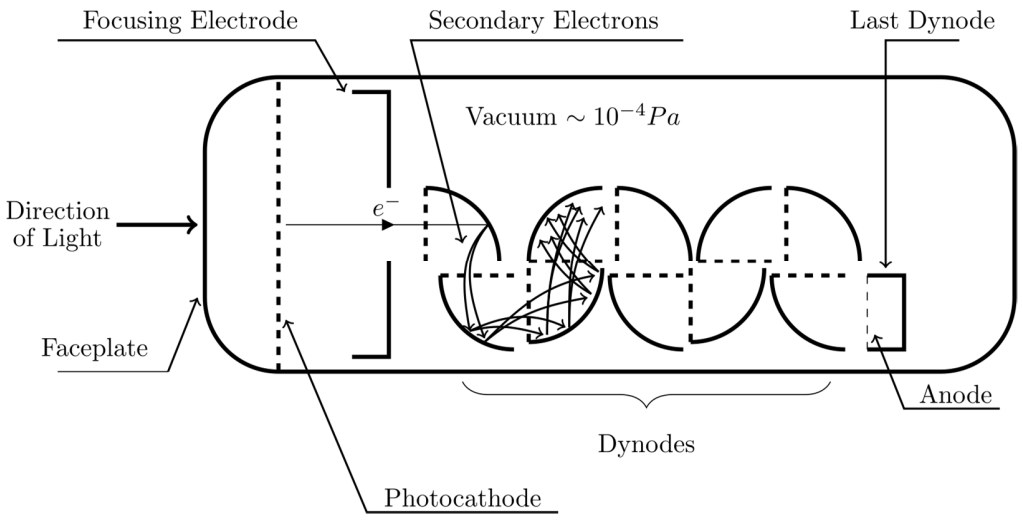

Figure 2.12: Schematic of a Photomultiplier tube. [87]

It is a sealed and evacuated glass vessel with an optically transparent faceplate. A photocathode coated with an alkali metal or a III-V semiconductor such as GaAs is placed behind the faceplate. Photons incident on the photocathode lead to emission of photoelectrons by the photoelectric effect. These photoelectrons are accelerated and focused by the focusing electrode onto the first of the dynodes, where they are multiplied by secondary electron emission. The dynodes are made of metal coated with a secondary emissive material such as Gallium Phosphide. Electrons are attracted to the dynodes by electrostatic means. Secondary electrons move to successive dynodes where they are multiplied further. The photoelectrons are eventually collected behind the anode after they reach the last dynode.

One of the biggest disadvantages of photomultipliers is their need for high voltages.

They are bulky and fragile. They are however still widely used in the medical sector and occasionally in the space sector. Several vidicon tubes have successfully made their way to the moon and returned interesting pictures. Due to their low dark noise, high sensitivity, and ultrafast response, photomultipliers are often coupled to scintillators and used for X-ray spectroscopy.

2.2.2 The p-n junction diode

The first $p-n$ junction was created accidentally by Russell Ohl in 1939 [88] . His work has revolutionised semiconductor electronics since, with all diodes being descendant of his work. The work presented in this thesis focuses on photon interactions with p-n juntions operated in photovoltaic and reverse biased mode.

In photovoltaic mode, the depletion region is not sufficiently wide such that most of the photons are absorbed outside the depletion region. Only photons absorbed near or in the depletion region contributes to photocurrent from the device. At best, one low energy photon will produce one electron-hole pair.

The p-n junction diode can be operated with a large reverse bias, which will induce a large electric field in the depletion region. The large electric field accelerates carriers drifting in the field such that they gain sufficient energy to free further carriers upon collision with atoms in the depletion region. This is known as impact ionisation.

One major drawback of a $p-n$ diode is that the diffusion process can be slow and hence the current gain-bandwidth of such device can be small.

2.2.3 pin diode

The $p-n$ junction can be modified to include a middle intrinsic layer as illustrated in Figure 2.13. The pin diode offers a wide depletion region and hence provides better absorption. An example of an electric field profile is also shown. The intrinsic layer can be slightly n-type (or p-type) doped and ohmic contacts on the p^+ and substrate are shown. The device is reverse biased with a voltage source as illustrated in Figure 2.13. A circular top metal contact is used to allow light to enter through the optical window on the p^+ layer.

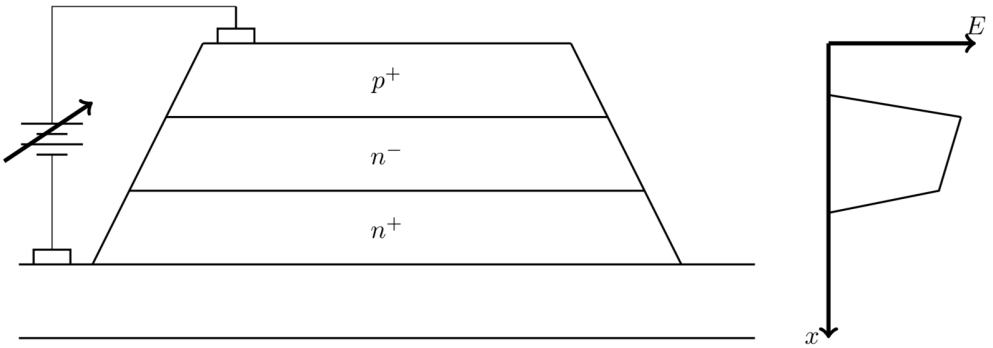

Figure 2.13: Generic pin with electric field profile on the right

The depletion region of a pin structure usually extends into the heavily doped p^+ and n^+ regions in order to achieve charge balance. A reverse bias ensures that the depletion region extends all the way through the i-layer. This then causes an electric field greater than the diffusion field to develop across the device. The depletion region contains ionised atoms that create the diffusion field in addition to the electric field created by the reverse bias voltage. Carriers created near or in the depletion width are accelerated by the electric field towards the diodes contacts, contributing to current in the external circuitry. If photons are absorbed entirely in the p^+ layer and all the carriers are generated outside the depletion region, then the minority electrons will diffuse until they recombine with the majority holes or reach the depletion region. Only carriers freed near or in the depletion region lead to current.

The efficiency of light to current conversion depends on the construction of the photodiode. Doping densities and depletion width are key parameters when designing a photodiode. A thick depletion region will increase the quantum efficiency of a device as a larger fraction of the incident photons will be absorbed. On the other hand, a thin depletion region will reduce the transit time of carriers allowing high speed operation. A trade-off between speed and quantum efficiency needs to be considered at the time of device design.

In this structure, more than one electron-hole pair can be created for each incident photon through a process called impact ionisation. Impact ionisation is the process by which energetic electrons (or holes) lose their energy upon interaction with atoms in the crystal

lattice, resulting in the creation of electron-hole pairs. An energetic electron (or hole) loses its energy to an electron in the valence band, promoting it to the conduction band. A newly created hole is left in the valence band. In effect, one energetic carrier creates two carriers after an interaction. The newly created carriers can in turn create further electron-hole pairs as they travel through a high electric field region. This process is illustrated in Figure 2.14. The photo-generated electron and hole are swept towards the n and p layer respectively and during their travel through the i-layer, creating a new electron-hole pair through impact ionisation. The impact ionisation process is often characterised by the impact ionisation coefficients, α and β for electron and hole respectively. Impact ionisation coefficient is defined as the total number of ionisations per unit distance and the distance travelled by a carrier between two successive ionisation events is referred to as the ionisation path length.

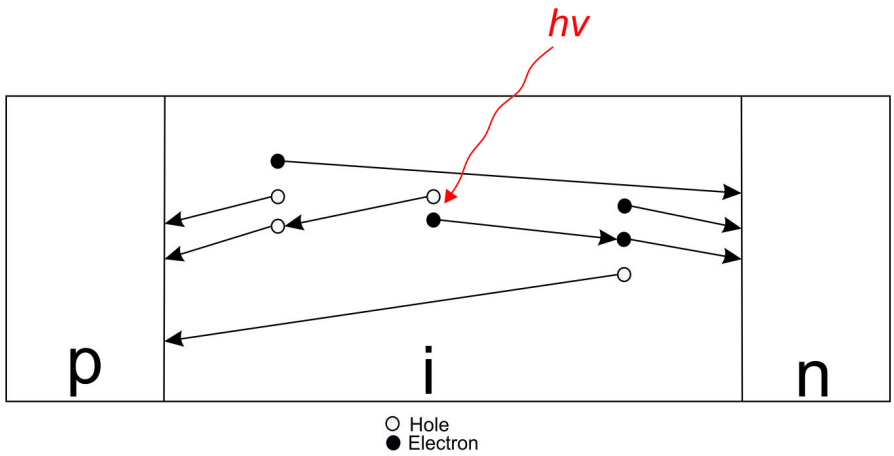

Figure 2.14: Illustration of impact ionisation process

2.2.4 Avalanche Photodiode

For low photon intensity applications, avalanche photodiodes (APD), which contains an internal region where multiplication occurs, can provide significant advantages over a simple three region device. The Avalanche photodiodes operate at bias voltages close to their breakdown where impact ionisation takes place.

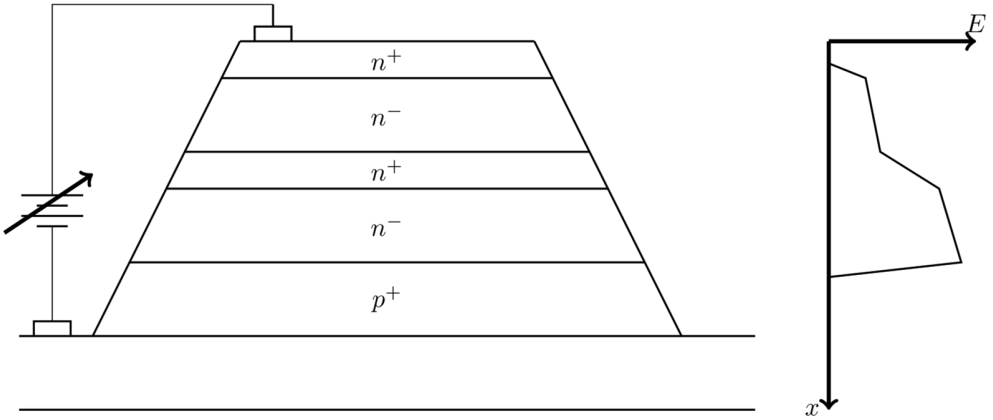

Figure 2.15: Generic SAM-APD with electric field profile on the right

Figure 2.15 shows a five region separate absorption and multiplication region Avalanche photodiode (SAM-APD) with a typical electric field profile shown on the right. An optical window is etched on top of the n^+ layer to allow photons to enter the first region. If the majority of carriers are generated in the top n^- region where the electric field is low, the carriers will be swept through that layer and experience multiplication in the lower n^- region.

For a SAM-APD, the electric field extends close to the surface allowing more carriers to be collected by the field and hence minimising recombination in the n^+ cap. For a three region structure, for carriers to contribute to current, they must diffuse into the field region. For a SAM-APD, carriers generated in the absorption region experience a low field which sweeps them into the multiplication region. This leads to a higher carrier velocity for the SAM-APD when compared to the three region device where the field is high enough to support impact ionisation.

A SAM-APD can be manufactured with two different semiconductor compound to

form a heterostructure. For instance, the absorption region can be made of a compound suited for a particular wavelength of light and the multiplication region can be made with a material that provide low dark current and high gain. A further benefit of a SAM-APD structure is the device lower capacitance in comparison to a three region device exhibiting similar breakdown. This is due to the wider depletion region in the SAM-APD.

2.2.5 Reachthrough APD

An alternative APD structure to the SAM-APD is the Reach-through APD (RAPD). A basic structure of a RAPD is shown in Figure 2.16 with its associated electric field profile on the right. The RAPD contains a much wider low field absorption region and a narrow region of high field where multiplication takes place. Photons absorbed in the absorption region leads to the creation of electron hole pairs. The electrons drift towards the high field where they avalanche. The primary holes in the low field region, drift to the top towards the p-contact and secondary holes drift into the low field, hence reducing the gain due to holes and the risk of breakdown. One drawback of such structures and SAM-APDs is that dark current also undergoes electron multiplication, resulting in higher shot noise. This structure maximises absorption and have good quantum efficiency for applications such as X-ray spectroscopy.

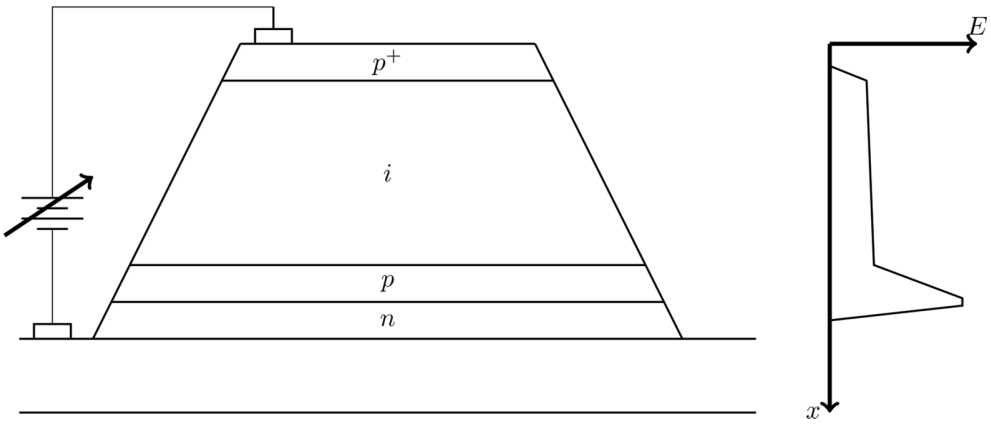

Figure 2.16: Generic Reach-Through APD with electric field profile on the right

RAPDs have been reported to provide good resolution for X-ray spectroscopy [89-91]. The internal gain of the device is reported to provide a considerable improvement to

the measurement. Kataoka et al. reports a FWHM of 379 eV when a cooled commercial Si RAPD was exposed to a ^{55}Fe X-ray source [89]. RAPDs coupled to scintillators have also been proven successful as an alternative to PMTs coupled to scintillators [92].

2.3 Noise Equivalent Power

In optical communication, Noise equivalent power (NEP) is a figure-of-merit that have historically been used to define the performance of an optical receiver. However, NEP has little significance unless additional information such as the system bandwidth is specified. NEP is the signal power required to achieve unity signal-to-noise ratio at bandwidth of 1 Hz. The signal power is given by:

$$(MR_oP_{in})^2 \tag{2.5}$$

where R_o is the responsivity of the APD without the multiplication factor M and P_{in} is the optical power. R_oP_{in} gives the unmultiplied photocurrent. The noise power consists of the multiplied bulk dark current noise power, multiplied photocurrent noise power and TIA noise power given by:

$$Noise\ Power = 2eBM^2FI_{db} + 2eBM^2FR_oP_{in} + (i_{on})^2 \tag{2.6}$$

where i_{on} is the average equivalent current noise of the pre-amplifier, F is the excess noise factor, B is the bandwidth and I_{db} is the unmultiplied bulk dark current. For NEP calculations, signal-to-noise ratio (SNR) is unity and thus signal power = noise power. Using B = 1 Hz, NEP is given in $\left(W/\sqrt{Hz}\right)$ by:

$$NEP = P_{in} = \frac{2eFR_o + \sqrt{(2eFR_o)^2 + 4R_o^2\left[2eFI_{db} + \left(\frac{i_{on}}{M}\right)^2\right]}}{2R_o^2} \tag{2.7}$$

In analog optical receivers, the use of NEP is most suited as SNR is a familiar measure of performance.

2.4 Interaction of X-rays in photodiodes

X-ray photons interact with a semiconductor material in three major ways: photoelectric effect, Compton scattering and pair production. Pair production occurs only when the photon energy is larger than twice the rest mass energy of an electron, 1.02 MeV. The probability of pair production is small for energy less than 1 MeV. X-ray photons used in this work range from 5 keV to 30 keV and hence this process can be discounted. For a consideration of pair production, see [93]. Compton interactions involve a partial transfer of the photon energy to an electron which is then referred as a recoil electron.

Compton scattering occurs when an incident photons interact with an electron in the absorber, partially transferring its energy to the recoil electron. The photon is deflected through an angle and because any deflection angle is possible, the proportion of energy transferred to the electron will vary for every interaction. For photoelectric effect interactions, an incident photon interacts with an absorber atom and an energetic photoelectron is ejected by the atom from one of its bound shells. The energy of the incident photon is completely transferred in this case. The probability of Compton effect is negligible for energy up to 30 keV. Most of the work reported in this thesis involves the interaction with soft X-rays and hence the photoelectric effect is the dominant interaction process.

2.4.1 Photoelectric effect

Photoelectric effect is the dominant mechanism for soft X-rays and the interaction cannot occur with free electrons. The interaction only takes place with an absorber atom. An X-ray photon ionises an absorber atom, freeing an electron named the photoelectron. The incident X-ray photon's energy *hv* is completely transferred and the ejected photoelectron energy is given by:

$$E_{e^-} = hv - E_{bind} \tag{2.8}$$

where E_{bind} is the binding energy of the electron in its original shell. This vacancy is

then filled by rearrangement of the electrons in the atom or by the capture of a free electron from the material. When the vacancy is filled by rearrangement, energy is liberated either in the form of a characteristic X-ray (also known as fluorescence) or by the emission of an Auger electron. The energy of both, the characteristic X-ray and the Auger electron, depends on the electronic configuration of the ionised atom. The characteristic X-ray is either absorbed by the material or escapes. When a characteristic X-ray of energy, E_{flu}, escapes, an escape peak energy appears in the collected energy spectrum and is given by:

$$E_{esc} = E - E_{flu} \tag{2.9}$$

where *E* is the initial X-ray photon's energy. Characteristic X-rays are usually reabsorbed close to the original interaction. If the X-ray photons are absorbed close to the surface, then the characteristic X-ray may escape without re-absorption resulting in an escape peak in the collected energy spectrum. A schematic of the photoelectric process is shown in Figure 2.17.

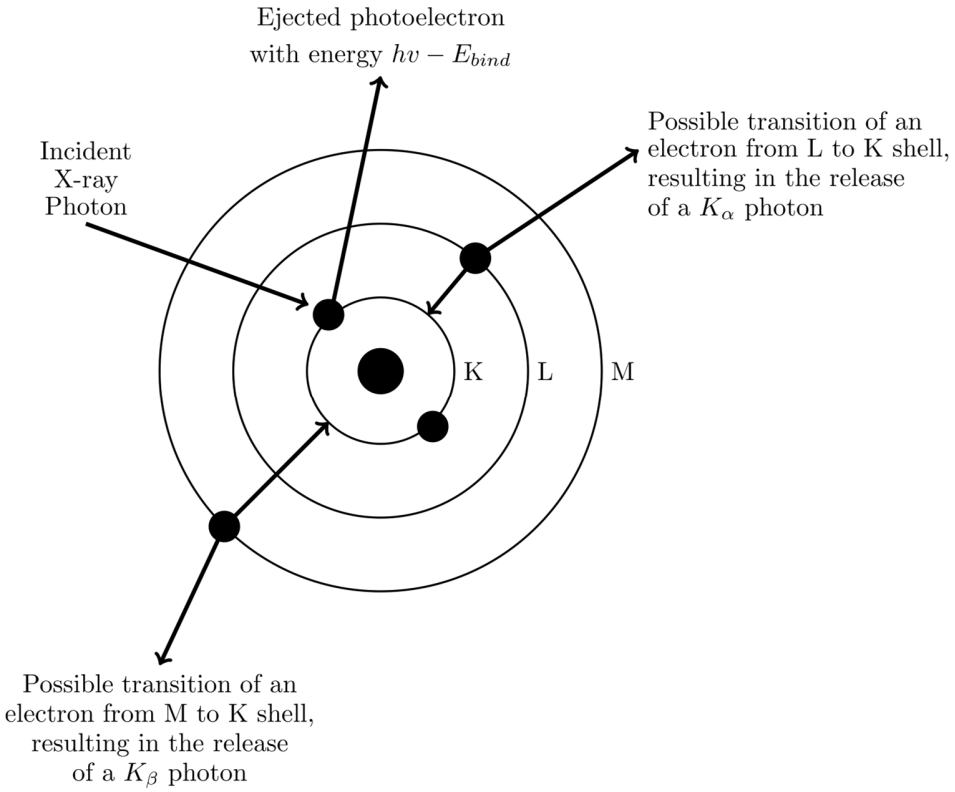

Figure 2.17: Schematic of Photoelectric effect

The energy of an Auger electron also depends on the electronic configuration of the ionised atom. The ratio of the ejection of an Auger electron to the emission of secondary X-rays is dependent on the atom and its fluorescence. The probability that a vacancy in the ionised atom will result in a radiative transition determines the fluorescence yield.

2.4.2 Beer-Lambert law

X-rays incident on a material are attenuated as they go through it, according to Beer-Lambert law. The intensity of the X-rays as they travel through a material is given by:

$$I(\xi) = I_o e^{-\phi\xi} \tag{2.10}$$

where $I(\xi)$ is the intensity at depth ξ, I_o is the intensity of the incident X-rays and ϕ is the linear attenuation coefficient of the material. The absorption at depth ξ can then be expressed as:

$$I_o(1 - e^{-\phi\xi}) \tag{2.11}$$

The absorption needs to be maximised in order to detect a larger proportion of the incident X-rays and to achieve that, the absorption layer's linear attenuation coefficient, ϕ, and depth, ξ, need to be maximised. In a SAM-APD structure, it is thus desirable to have a thick absorption region. However the maximum desirable thickness of the absorption region is also limited by the growth quality and the charge carrier mobility in the detector [94]. The linear attenuation coefficient can be expressed as follows:

$$\phi = \left(\frac{\vartheta}{\rho}\right)\rho \tag{2.12}$$

where ρ is the density of the material in $\mathrm{gm\,cm^{-3}}$ and $\frac{\vartheta}{\rho}$ is the mass attenuation coefficient of the material in $\mathrm{cm^2\,gm^{-1}}$. The linear attenuation coefficient varies with the material density but stays the same for the same material for a particular energy. The linear attenuation coefficient, ϕ can be maximised by selecting a detector material with a high atomic number Z. The probability, that a photon is absorbed at a depth ξ in a material, is given by:

$$P(\xi) = 1 - e^{-\varphi\xi} \tag{2.13}$$

where φ is the mass attenuation coefficient.

The mass absorption coefficient of the semiconductor compound containing more than one element is a weighted average of the mass absorption coefficients of its constituent elements. The mass absorption coefficient of a compound is given by:

$$\left(\frac{\vartheta}{\rho}\right)_{compound} = w_1\left(\frac{\vartheta}{\rho}\right)_1 + w_2\left(\frac{\vartheta}{\rho}\right)_2 + w_3\left(\frac{\vartheta}{\rho}\right)_3 + \cdots \quad (2.131)$$

where w_1 , w_2 , w_3 , … are the weight fractions of elements 1, 2, 3, … and $\left(\frac{\vartheta}{\rho}\right)_1$, $\left(\frac{\vartheta}{\rho}\right)_2$, $\left(\frac{\vartheta}{\rho}\right)_3$, … represent their mass absorption coefficients.

2.4.3 Charge generation and transport

The absorption of an X-ray will lead to the creation of an average number of electron-hole pairs (EHPs) given by:

$$N = \frac{E}{\varepsilon} \quad (2.14)$$

where E is the X-ray photon initial energy and ε is the electron-hole pair creation energy. Equation 2.14 is only true when no electrons escape the detector. While equation 2.14 gives the average number of electron-hole pairs created for a particular energy E, the actual number of electron-hole pair varies randomly from one photon absorption event to the next. A smaller electron-hole pair creation energy, ε will lead to a larger amount of EHPs, hence a larger amount of charge and thus improving the signal to noise ratio of a radiation detection system. For semiconductor compound such as AlInP, ε is large; leading to a smaller amount of charge. In that case, other solutions for improving the SNR is implemented.

2.4.4 Energy resolution of an X-ray spectroscopy system

The ability to measure and resolve X-ray characteristic lines is the foundation of an X-ray spectroscopy system. The energy resolution of an X-ray detector defines how close X-ray energy lines can be in terms of energy and still be distinguishable from each other. A smaller (better) energy FWHM allows X-ray lines close to each other to be more clearly resolved.

There are various factor that causes fluctuation in the measured energy spectra of a single X-ray photon energy. The FWHM energy resolution of a semiconductor X-ray

detector can be expressed as follows:

$$\delta E = 2.35\varepsilon\sqrt{\frac{FE}{\varepsilon} + R^2 + A^2} \tag{2.15}$$

Where ε is the creation pair energy for the semiconductor, *E* is the energy of the incident photons, *F* is the Fano factor(described below) [95], *R* represents the equivalent noise charge due to movement of charges to the contacts in the detector (in e^- r.m.s) and *A* refers to the equivalent noise charge introduced by the detector leakage current, detector's capacitance and the electronics which includes noise due to stray capacitance and gate current of the input JFET (in e^- r.m.s) [96]. In an X-ray spectroscopy system, it is desirable to minimise *R* and *A*. If the contribution of *R* and *A* is small, the spectral resolution is said to be Fano limited.

2.4.4.1 **Energy resolution of an X-ray detector**

The intrinsic detector noise is defined by the statistical fluctuations of the number of electron hole pairs created by each photon event and this limits the lowest possible energy resolution that can be measured by a semiconductor detector, known as the Fano limit. Fano [95] showed that there is a fluctuation in the number of ions created by the ionisation of gas by radiation. In the same way in a semiconductor compound, each X-ray photon will create a different amount of carriers depending on where it was absorbed and this will lead to a distribution of carrier numbers over time.

If the process of creating electron-hole pair is Poissonian, the standard deviation, σ, of *N* is given by $\sqrt{N}$. For X-ray APDs, *N* tends to be typically large and the final distribution follows the central limit theorem and approaches a normal distribution, with the FWHM given by:

$$FWHM = 2.35\sigma \tag{2.16}$$

The Fano factor *f* describes the variance in the total number of charge carriers *N* during each photon interaction and *f* can be quantify as follows:

$$f \equiv \frac{Observed\ Variance\ in\ N}{Predicted\ Poissonian\ Variance\ in\ N} \tag{2.17}$$

The Fano limited resolution of a detector can be expressed in terms of energy as follows:

$$E_F[eV] = 2.35\varepsilon\sqrt{fN} = 2.35\varepsilon\sqrt{\frac{fE}{\varepsilon}} \tag{2.18}$$

2.4.4.2 **Parallel white noise**

Parallel white noise arises from the shot noise of the currents flowing into the input of the preamplifier. The currents are mainly made up of the leakage current $I_{leakage}$ of the detector and the gate current I_G of the preamplifier in the case of a JFET input topology. Other contribution to the parallel white noise stem from the resistors connected to the input, such as the feedback resistor in a conventional charge sensitive preamplifiers. For AC coupled detectors, the biasing resistor will contribute to the parallel white noise [97]. The spectral noise power density due to parallel white noise can be expressed as follows:

$$S_{PW} = 2q\alpha\left(I_{leakage} + I_G\right) + \frac{4kT}{R_f} \tag{2.19}$$

where q is the charge on an electron, k is the Boltzmann constant, T is the temperature in Kelvin and R_f is the resistance of the preamplifier feedback resistor. For charge sensitive preamplifiers without a feedback resistor, the last term can be omitted. The equivalent noise charge contribution to the term *A* from equation 2.19 can be written as:

$$ENC_{PW}[e^{-}r.m.s] = \frac{1}{q}\sqrt{\frac{A_3}{2}S_{PW}\tau} \tag{2.20}$$

where τ is the shaping time and A_3 is a constant dependent on the type of signal shaping [98].

2.4.4.3 **Calculating A_3**

The value of A_3 depends on the specifications of the shaping amplifier. In this work, an Ortec 570 is used to shape the output from the CSP. A_3 is given by:

$$A_3 = \int_0^\infty [f(x)]^2 \, \mathrm{d}x \tag{2.21}$$

where $x = \frac{t}{\tau}$ and $f(x)$ is the shaping function [98]. The ortec 570 has a semi-gaussian function given by:

$$f(t) = \left(\frac{t}{\tau}\right)^n e^{(-t/\tau)} \tag{2.22}$$

where $n = 2.2$ for the Ortec 570[56]. Using equations 2.21 and 2.22, A_3 was calculated to be 2.68 for the Ortec 570 shaping amplifier.

2.4.4.4 **Series white noise**

Series white noise is primarily due to the input JFET's drain current thermal noise. Stray resistance in series with the JFET's gate can also contribute to the series noise but it is negligible. The series white noise power spectral density, S_{SW}, can be approximated to:

$$S_{SW} = \gamma \frac{4kT}{g_m} \tag{2.23}$$

where $0.7 \leq \gamma \leq 1$, depending on the JFET structure and characteristics [99]. The contribution of S_{SW} to the equivalent noise charge in e^- r.m.s is given by:

$$ENC_{SW} = \frac{1}{q}\sqrt{\left(\frac{A_1}{2}\right) S_{SW} C_T^2 \frac{1}{\tau}} \tag{2.24}$$

where A_1 is a constant dependent on the type of signal shaping [98] and C_T represent the total capacitance seen at the input of the preamplifier. ($C_T = C_d + C_i + C_f + C_s$, where C_d is the capacitance of the detector, C_i is the JFET input capacitance, C_f is the feedback capacitance and C_s represents any stray capacitance.)

2.4.4.5 **Calculating A_1**

A_1 is given by:

$$A_1 = \int_0^\infty [f'(x)]^2 \, \mathrm{d}x \tag{2.25}$$

where $x = \frac{t}{\tau}$ and $f'(x)$ is the first derivative of the shaping function [98]. Using equation 2.25, A_1 was calculated to be 0.79 for the Ortec 570 shaping amplifier.

2.4.4.6 **1/f series noise**

The $1/f$ series noise contribution stems from the drain current noise of the input JFET. The spectral noise density is given by:

$$S_{1/f} = \frac{A_f}{f} \tag{2.26}$$

where A_f is a JFET characteristic constant. The contribution of $1/f$ series noise to the equivalent noise charge is given by:

$$ENC_{1/f} = \frac{1}{q}\sqrt{A_2 \pi A_f C_T^2} \tag{2.27}$$

where A_2 is a constant dependent on the type of signal shaping and ranges from 0.64 to 2 [98].

2.4.4.7 **Dielectric noise**

Dielectric noise contribution to the term *A* originates from dielectric in close proximity to the preamplifier input. Sources of this noise stem from the packaging of the JFET and the detector, the feedback, test capacitors and the printed circuit board. The dielectric equivalent noise charge (in e^- r.m.s) is given by:

$$ENC_D = \frac{1}{q}\sqrt{A_2 2kTDC_{dielectric}} \tag{2.28}$$

where $C_{dielectric}$ is the capacitance of the dielectrics, *D* is the dissipation factor of the dielectrics [100]. To minimise the dielectric contribution, it is desirable to reduce the total capacitance of the dielectrics, for example by packaging the input JFET with the detector. An integrated detector-FET assembly can also help minimise the dielectric noise contribution as reported in [101].

2.4.4.8 **Induced gate current noise**

Fluctuations in the JFET gate curent leads to an induced gate current noise. The fluctuation is caused by the drain current noise giving rise to induced charge fluctuations through the capacitance between the channel and the gate. The power spectral density of this induced current noise is derived in [102] and is given by:

$$S_{ig} = S_{SW}\omega^2 C_{gs}^2 \delta \tag{2.29}$$

where C_{gs} is the gate-to-source capacitance, δ is a dimensionless factor which depends

on the JFET's biasing conditions and S_{SW} is given by equation 2.23. Experimental methods to measure δ are given in [103].

Being parallel with the input, the current noise generator S_{ig} gives rise to a white noise spectrum which is correlated to the series white noise given by equation 2.23.

Equation 2.23 can then be modified to take S_{ig} into account and is given by[102]:

$$S_{SWE} = S_{SW} G_c \tag{2.30}$$

The equivalent noise charge contribution is then given by:

$$ENC_{SWE} = \frac{1}{q}\sqrt{A_1 S_{SW} G_c C_T^2 \frac{1}{\tau}} = ENC_{SW}\sqrt{G_c} \tag{2.31}$$

Experiments carried by Bertuccio *et al.* [97] showed that a value of $\sqrt{G_c} \equiv 0.8$ can be used to take the induced gate noise into account.

2.4.4.9 **Combination of noise sources**

The ENC contribution due to parallel white noise is proportional to τ as shown by equation 2.20 and this contribution can be significant at longer shaping time. The detector dark current, being the most readily measurable parameter, can be used as a tool to optimise future detectors in terms of active area for instance. For example, at 293 K, GaAs detectors have dark current densities up to a few $\mathrm{nA/mm^2}$ [104-106] and this puts a constraint on the maximum active area. The parallel white noise contribution is however comparable with the series white noise contribution at the optimum shaping time.

The input stage of the preamplifier also contributes to the parallel white noise due to the gate current in the case of a JFET-input or due to the base current for a BJT-input preamplifier. A good silicon JFET will have gate current below 1 pA at room temperature. GaAs based MESFETs and HFETs have gate current ranging from 100 pA to 10 nA at room temperature and they usually require cooling to operate with acceptable noise performance [107]. Heterojunction FETs also have gate current in nA, making them potentially unsuitable for spectroscopy systems [108]. Bipolar transistors operate with base current in the region of tens of nA. The transconductance can be small for low current gains which also leads to higher series white noise.

The spectral power densities of the series (S_s) and parallel (S_p) white noise sources for a bipolar transistor is given by:

$$S_s = \frac{2kT}{g_m} + 4kTr_b + \frac{A_f}{f} \tag{2.32}$$

$$S_p = 2qI_b + \frac{B_f}{f} \tag{2.33}$$

where g_m is the transconductance, I_b is the base current and r_b is the base spreading resistance. A_f and B_f are coefficient which are independent of frequency f [109]. The value of r_b can be reduced by using a BJT with an optimised emitter area. The downside is that such BJT will operate at lower collector current and thus low transconductance.

From equation 2.24, it is shown that the series white noise contribution is dependent on the total capacitance seen at the input of the preamplifier. So, for higher resolution, detectors with low capacitance is desirable. Having a small input capacitance JFET will reduce the total capacitance and hence reduce the total contribution of the series white noise. The transition frequency of a JFET is inversely proportional to the gate-to-source capacitance and using a JFET with the highest transition frequency and a high transconductance can minimise the total noise contribution. A small total input capacitance will also lead to a smaller contribution from the $1/f$ series noise.

Like $1/f$ series noise, the dielectric noise contribution is independent of shaping time. For room temperature operation, the dielectric noise can seriously limit the resolution of an X-ray spectroscopy system [110]. The dielectric noise can be reduced by optimising circuit layout and using PCB substrates with a lower dielectric constant.

The dependence of the series white noise and parallel white noise on $1/\tau$ and τ respectively, allows an optimum shaping time which will minimise the combined noises and lead to a higher resolution is a spectroscopy system.

The next chapter presents some standard measurement techniques that are applicable for the work presented in this thesis.

Chapter 3 Measurement Techniques

The previous chapter presented background theories on circuits and detectors commonly used for X-ray spectroscopy and LiDAR. In this chapter, some standard measurement techniques are discussed. These measurements are performed when a new diode sample is available or a new circuit is designed. The APDs and PDs presented in this work were evaluated in terms of their dark current-voltage (IV) characteristic, capacitance-voltage (CV) and avalanche gain. Doping profile and depletion width were estimated from capacitance-voltage (CV) characteristics by modelling the CV profile. Photomultiplication measurements were carried out to evaluate the avalanche gain of the APD with increasing reverse bias voltage. The performance of APDs as an X-ray detector was evaluated with a simple spectrometer setup. Circuit characterisation techniques are also presented in this chapter.

3.1 Photodiode Characterisation

3.1.1 Electrical characterisation

Reverse current-voltage measurements (IVs) are one of a number of fundamental ways of assessing APDs. The tests are usually performed shortly after devices are manufactured. An HP 4140B picoammeter was used to measure the IVs presented in this work. The IV measurements are carried out in the dark to avoid the photo-generation of carriers. From the reverse IV characteristics, the significance of bulk and surface leakage currents are assessed by normalizing the dark current to area and perimeter respectively. The breakdown voltage and IV uniformity over a significant sample size are also obtained from the IV characteristics. The breakdown voltage can be used, in conjunction with capacitance voltage characteristics, to model doping densities.

The origin of the breakdown can be determined if different diameter devices of the same structure and compound are available. Bulk breakdown, which is preferable, occurs when the maximum electric field that the material type can support is exceeded.

Devices with consistent IV characteristics were selected and packaged. IV measurements were carried out on devices prior to and after packaging to assess any

degradation caused by the packaging process.

Forward current-voltage characteristics were used to assess whether devices have an exponential behaviour, therefore obeying the Shockley equation 3.1. [111].

$$I_f = I_s \, exp\left(\frac{q(V_a - I_f R_s)}{nkT} - 1 \right) \tag{3.1}$$

where I_f is the total current, I_s is the saturation current, q is the electron charge, k is the Boltzmann's constant, T is the absolute temperature, V_a is the terminal voltage, n is the ideality factor and R_s is the series resistance. The ideality factor indicates the nature of the current flow across the region. Usually an *n* close to 1 indicates a diffusion dominated process while an *n* close to 2 indicates the dominance of recombination process.

Doping profile and depletion region width of devices were determined by reverse capacitance voltage (CV) characteristics in conjunction with data provided by other experimental results, such as secondary ion mass spectroscopy (SIMS). The CV measurements were performed using a HP 4275 LCR meter. Reverse CV of the devices from the same wafer should scale with area. CV data, in conjunction with IV characteristics, can be used to determine the intrinsic region width in devices. Most of the CV data presented in this work was obtained after devices were packaged in suitable headers. Methods to derive and determine doping densities and depletion width can be found in [112].

3.1.2 Photo-Multiplication

Photo-multiplication measurements were performed on reverse biased APDs to determine their multiplication factor M, using the system shown in the block diagram of Figure 3.1. Light from the laser is modulated using an optical chopper and the chopper trigger signal is fed to the lock-in amplifier (LIA). The light from the laser is focused on the top of the diode by a microscope objective. For fiber-coupled diodes, an electronically modulated fiber-coupled laser is used. Photocurrent from the diode is translated to a voltage by the TIA and

measured with the LIA. The photocurrent is measured as a function of reverse bias voltage provided by a Keithley 2400 source-measure unit. The gain is then as $M(V) = I_{ph}(V)/I_{pr}(V)$, where I_{pr} is the primary photocurrent and I_{ph} is the total photocurrent.

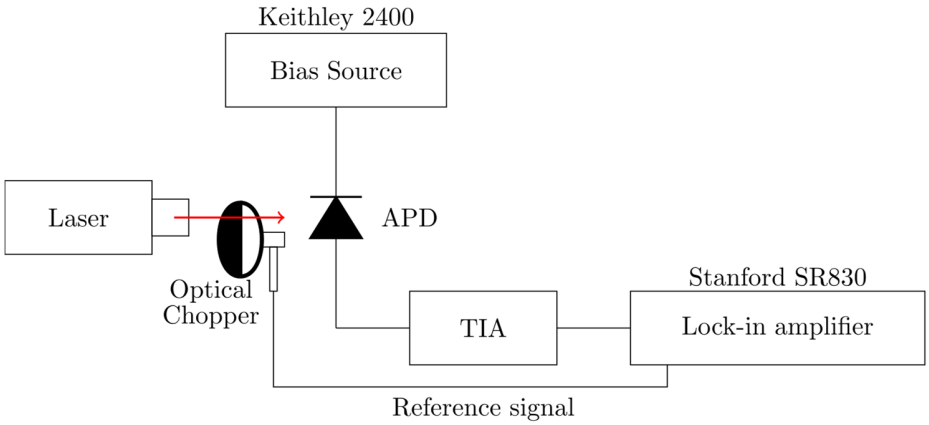

Figure 3.1: System block diagram of AC photo-multiplication measurement setup

Photo-multiplication measurement of diodes, with a dark current significantly lower (at least two orders of magnitude) than the primary photocurrent, can be treated as a reverse IV measurement with the exception that the diodes are illuminated.

3.2 X-ray Spectrometry

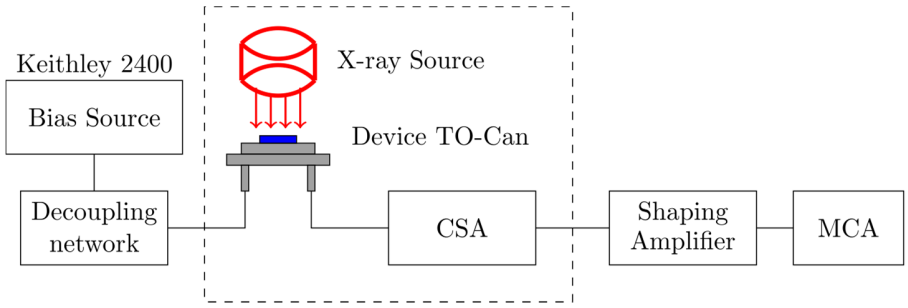

Figure 3.2: System block diagram of a simple X-ray spectrometer

A simple X-ray spectrometer system diagram is shown in Figure 3.2. X-ray characterisation consists of collection of pulse height spectra of a detector APD irradiated with characteristic X-ray photons. Spectral resolution of the detected known energy peaks can then be determined. The noise peak is represented as the 0keV peak.

The detector is often packaged in a TO-header to facilitate measurements. The detector is DC-coupled to the charge sensitive preamplifier (CSP) and biased with a source-measure unit through a series of decoupling networks. The X-ray source is placed $\approx 1\text{cm}$ away from device. The X-ray source, TO-header and the CSP are placed in a diecast boxed lined with lead sheet to prevent radioactive leaks. The CSP output is connected to an Ortec 570 shaping amplifier. The shaping amplifier provides further amplification to the signal from the CSP. The amplified signal is then digitized with an Ortec EasyMCA-8k multichannel analyser (MCA) interfaced to a computer yielding pulse height spectra. The CSP is discussed in Chapter 5.

3.3 TIA characterisation

Voltage amplifiers (V to V) are the most common type of amplifiers and their bandwidth and gain can be easily measured using a spectrum analyser or a network analyser. The amplifier receives signal from an RF voltage source at its input while its output is connected to the analyser. For transimpedance amplifiers (I to V), it is slightly more challenging to measure the bandwidth and the gain as the amplifier requires a current input as opposed to a voltage input.

A voltage to current converter can be used to convert the voltage signal from the RF voltage source into a current signal, before feeding it to the input of the TIA. This can be in the form of an APD approximation test circuit that consists of a chain of resistors, as shown in Figure 3.3. It is however essential that the frequency response of the APD approximation circuit is constant over the frequency range of interest for the TIA.

For the circuit in Figure 3.3, at low frequency, the circuit's gain is expected to be constant but as the frequency increases the parasitic capacitances of the resistors become significant such that the gain of the resistor chain changes and a phase shift is introduced. It is virtually impossible to accurately simulate this circuit in SPICE as it is difficult to incorporate all the parasitic capacitances associated with the resistors and PCB layout in the SPICE models. Therefore extensive tests and measurements were carried out to find a practical combination of resistors that provided a large bandwidth. The circuit shown in Figure 3.3 was found to be satisfactory. The corresponding frequency response (measured using an Agilent Technology/HP 4396B network analyser) is shown in Figure 3.4. The gain remains relatively constant (within 3 dB) up to 100 MHz before the parasitic capacitances start to dominate. The value of capacitance C_j shown in Figure 3.3 is chosen to represent the total capacitance to ground that will be seen at the input of the TIA.

The measured power shown in Figure 3.4 corresponds to the power measured between V_{in} and V_{out} (from Figure 3.3) and with an RF source of 0 dBm feeding the input.

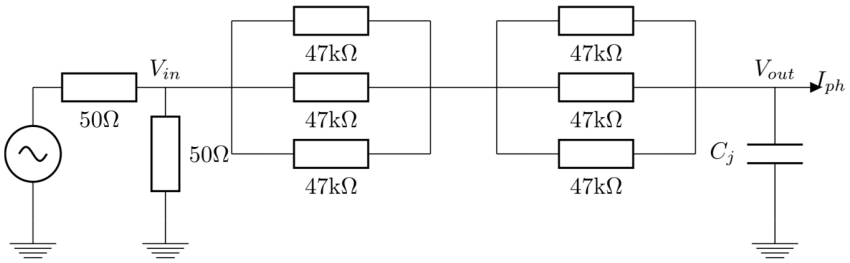

Figure 3.3: APD approximation circuit

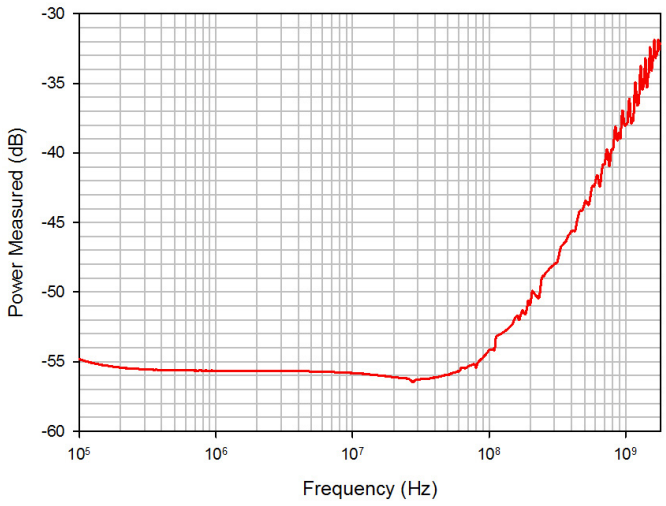

Figure 3.4: Frequency response of APD approximation circuit

Using the APD approximation circuit, the bandwidth of the TIA can be measured with a network analyser in a setup depicted in Figure 3.5. The network analyser's RF source is fed through a power divider into the APD approximation circuit, which converts the voltage into a current before presenting it to the input of the TIA. The output of the TIA is connected to the input A of the network analyser. The bandwidth can be automatically measured by the network analyser. The bandwidth can then be easily deduced from the data of parameter sweep.

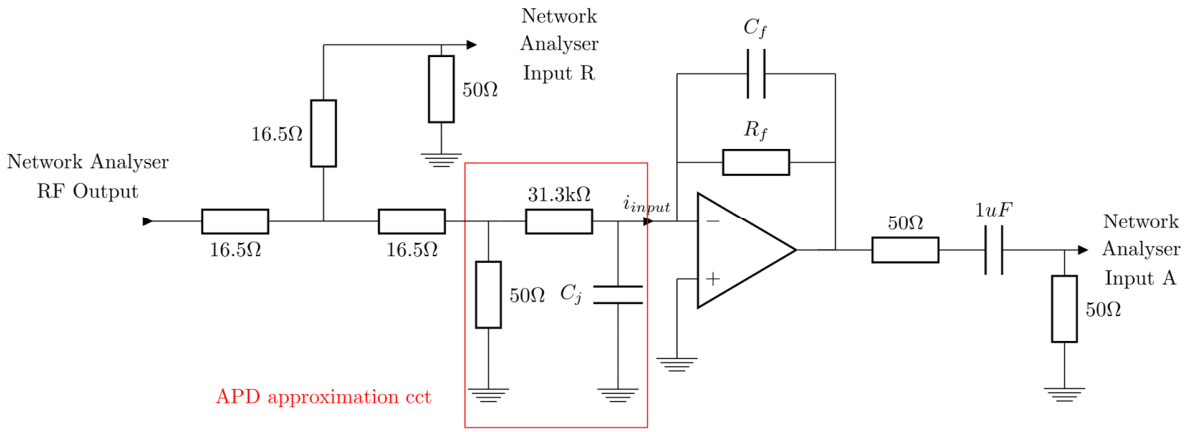

Figure 3.5: Schematic of TIA frequency response measurement set-up (The 50 Ω input impedance of the analyser is also shown)

3.4 Characterisation of charge sensitive preamplifiers

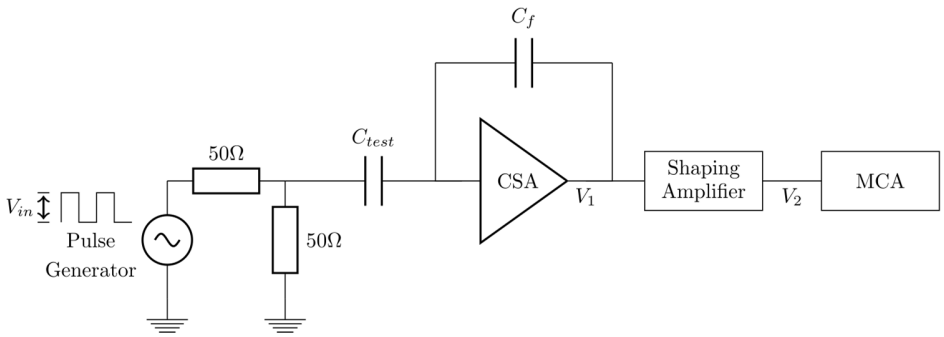

Figure 3.6: System block diagram of CSP characterisation

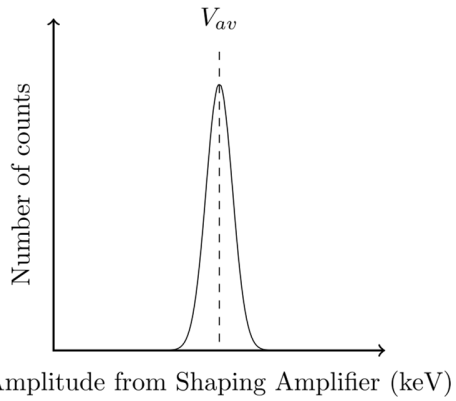

Figure 3.7: Amplitude distribution of the shaping amplifier measured using a multichannel analyser

In a typical X-ray spectroscopy system, it is usually the noise from the electronics rather than that from the detector that limits the energy resolution of the system. The setup shown in Figure 3.6 is used to characterise the noise performance of charge sensitive preamplifiers (CSP). A pulse generator together with a calibrated test capacitor is used to inject a test charges into the input of the CSP. A surface mount ceramic capacitor, with a 0906 package, is used as a test capacitor. A square pulse with a rise time of $\sim 10ns$ is used to apply voltage pulses to one side of the capacitor. Charges are applied to the input only during transition time given by $Q = C_{test}V_{in}$, where Q is the total charge transferred, V_{in}

is the amplitude of the square pulse and C_{test} is the value of the test capacitor. The exact value of the test capacitor is measured with an LCR meter.

The output of the CSP is shaped with an Ortec 570 shaping amplifier and a multichannel analyser is used to measure the amplitude distribution of the pulse trains coming from the it. The MCA is calibrated with two different voltage amplitude V_{in} which correspond to two different energy levels (in keV).

In a noise-less system, one amplitude of V_{in} will give rise to a Dirac impulse in the MCA energy spectrum. However, due to the noise present in the system, a Gaussian distribution, with a mean value corresponding to amplitude of the pulses is obtained in the energy spectrum as illustrated in Figure 3.7. The vertical axis represents the total number of pulses collected after a certain period of time, with V_{av} being the average amplitude. The horizontal axis represents the amplitude of the pulses expressed in equivalent radiation energy keV.

The standard deviation, σ, of the Gaussian is worked out by performing a fitting on the collected spectrum and the FWHM can be obtained in keV by $\mathrm{FWHM} = 2.35\sigma$. The ENC of the circuit can then be calculated by:

$$ENC = \frac{FWHM}{2.35\varepsilon} \tag{3.2}$$

where ε is the energy required to create an electron-hole pair in a detector. In silicon, the ε value is 3.62 eV at 300K.

Referring to Figure 3.6, the voltage V_1 out of the CSP is given by equation 3.3. The gain of the amplifier, often referred as "charge gain", is given by equation 3.4. The equation 3.4 shows that a small value of C_f will lead higher charge gain.

$$V_1 = \frac{C_{test}V_{in}}{C_f} \tag{3.3}$$

$$Gain = \frac{V_1}{Q} = \frac{1}{C_f}\ (V/C) \tag{3.4}$$

Using the method described above with a calibrated test capacitor, it can be difficult to know the exact value of the injected charge as some of the injected pulses are also transfer to the stray capacitances. To overcome this problem, a photodiode is connected to the input together with the test capacitor as illustrated in Figure 3.8. The photodiode is then exposed to a ^{55}Fe X-ray source and the MCA is calibrated in term of energy in keV by using the 5.9 keV collected energy peak and the noise peak for the 0keV energy. Pulses are then injected into the test capacitor to get the pulser peak. The pulser peak FWHM can then be obtained in terms of energy in keV.

The ENC measurement is also carried out with a biased APD detector connected to the input of the CSP as also illustrated in Figure 3.8. The biased APD is included because its capacitance and leakage current is often a significant factor in the overall system noise performance.

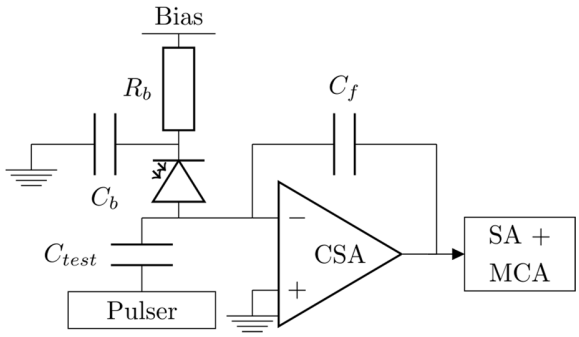

Figure 3.8: Simplified block diagram of the CSP noise measurement setup

Chapter 4 A Low Noise Transimpedance Amplifier for LIDAR Application

The previous chapter presented some of the measurement techniques used to characterise semniconductor devices and electronic circuit presented in this thesis. This chapter presents a low noise front-end that was designed for a LIDAR system, specified by the European Space Agency (ESA). This chapter reports the design methodology, implementation and characterisation of a low noise transimpedance amplifier. An equivalent input noise current of $\approx 2.6pA/\sqrt{Hz}$ with a bandwidth of 26 MHz is achieved, making it suitable for low noise LIDAR applications. The transimpedance amplifier was designed with a view to working with an APD that has an unmultiplied leakage current of up to 20nA and a junction capacitance of up to 5pF. The motivation has been presented in section 1.1. Design procedures and compromises are also discussed and the circuit performance is presented.

4.1 Design Requirements

The technical specifications in the contract with ESA are listed in table 1 and these define the design objectives of the TIA.

Parameter	Value	Comments
Input signal	Maximum pulse repetition frequency: 1 kHz/100 kHz Number of photons arriving in 50-200 ns period: Minimum: 8000 Maximum: 2×10^6	To be used for LIDAR mode measurements. Useful dynamic range over which specified performance is to be achieved.
Bandwidth	At least 20 MHz	APD-TIA Combination
Linearity	0.1% r.m.s.	Deviation from best linear fit over useful dynamic range, at the output of pre-

		amplifier.
NEP	100fW/√Hz	With an operating wavelength of 2000 nm

Table 1: Technical Specifications for TIA

Linearity can be simply defined as the characteristic of data such that a straight line provides a good fit using the least-squares criterion. Nonlinear regression dynamic fitting were carried out using the Sigmaplot software to determine linearity of data in this thesis.

The design requirements for the front-end amplifier were derived from the predicted performance of the detector's specifications as agreed with ESA. The NEP has been derived in section 2.3 and is reproduced here.

$$NEP = P_{in} = \frac{2eFR_o + \sqrt{(2eFR_o)^2 + 4R_o^2\left[2eFI_{db} + \left(\frac{i_{on}}{M}\right)^2\right]}}{2R_o^2} \quad (4.1)$$

By considering a Sheffield-grown InAs APD with a responsivity ,R_o, of 1.29 (equivalent to 80% quantum efficiency at the wavelength of 2000 nm), an excess noise factor F = 1.8 and a multiplication factor M = 100 [38], NEP calculations against TIA equivalent input noise current, i_{on}, were carried out for three different values of unmultiplied bulk APD dark current. Typical parameters of the InAs APD are shown in Appendix 10.1. The predicted NEP is presented in Figure 4.1. It can be seen that for highest APD dark current of 20 nA, a TIA equivalent current noise of up to $7\mathrm{pA}/\sqrt{\mathrm{Hz}}$ will be required to produce an NEP of close to $100fW/\sqrt{Hz}$.

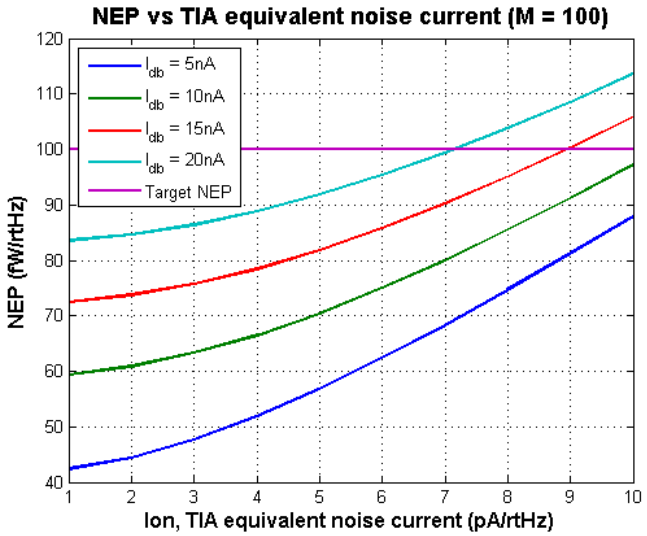

Figure 4.1: NEP vs TIA equivalent noise current for M=100

Using ESA's technical specifications and NEP calculations shown above, the following set of specifications were identified.

- Transimpedance gain of approximately 5000 V/A (2500 V/A terminated).
- -3 dB bandwidth of at least 20 MHz with a device junction capacitance of 5 pF.
- DC coupling of the APD to the TIA.
- Guaranteed stability with an APD capacitance of up to 5 pF.
- TIA input equivalent current noise of up to $7\text{pA}/\sqrt{\text{Hz}}$
- Stable with APDs with a shunt resistance of $1k\Omega$.

4.2 TIA Design & analysis

4.2.1 Stability & bandwidth

Although the TIA circuit introduced in section 2.1.3 appears quite straightforward, at high frequencies the presence of reactances causes complications. An APD or PD can be represented by a current source in parallel with a shunt resistance r_s and a capacitance C_j as shown in Figure 4.2. C_j is made up of the APD junction capacitance and any parasitic capacitance due to packaging for instance. Instability in a negative feedback circuit, such as a TIA, will lead to excessive ringing in the time domain and peaking in the frequency domain.

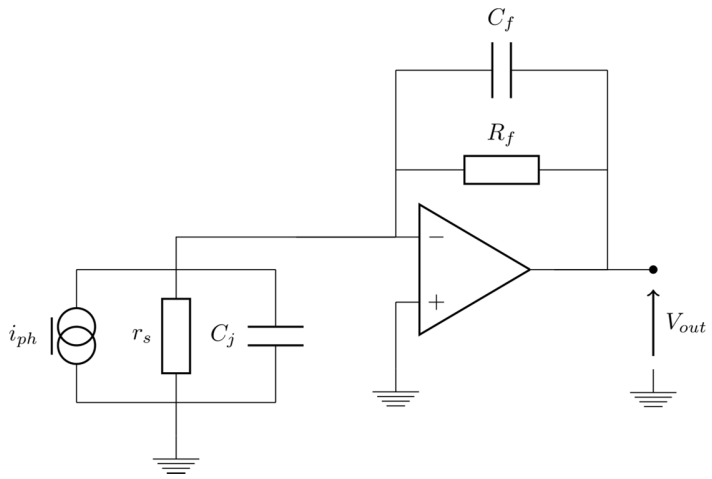

Figure 4.2: Opamp TIA with APD Small Signal model

The simplest opamp open loop transfer function will be of the form $A_v = \frac{A_0}{1+s\tau_0}$ where $\frac{A_0}{\tau_0}$ is the amplifier angular gain bandwidth product. Unfortunately, C_j interacts with the open loop transfer function in a way that promotes instability. However, compensation in the form of C_f in the feedback network allows stable working conditions. The interaction gives a second order transimpedance relationship which has a DC transimpedance gain of $-R_f$ and given in the form of equation 4.2.

$$\frac{v_{out}}{i_{ph}} = -R_f . \frac{1}{1+\frac{s}{\omega_0 q}+\frac{s^2}{\omega_0^2}} \tag{4.2}$$

The well-known peaking characteristic of a second order system can allow the perfect working conditions for the TIA to be derived. The damping factor ξ, given by $\frac{1}{2q}$, can provide a figure of merit in evaluating the performance of the opamp TIA.

An undamped natural frequency given by equation 4.3 and a damping term given by equation 4.4 can be derived numerically by considering the circuit in Figure 4.2. C_f has a small effect on ω_0 but a much more significant effect on the damping term.

$$\omega_0 \approx \sqrt{\frac{A_0}{(C_j+C_f)R_f\tau_0}} \tag{4.3}$$

$$\text{Damping term} = \frac{1}{C_fR_f+\frac{C_fR_f}{A_0}+\frac{C_jR_f}{A_0}} \tag{4.4}$$

The damping factor ξ can be shown to approximate to equation 4.5. A more detailed equation for the damping term is provided in appendix 10.1.

$$\xi \approx \frac{\sqrt{R_f}}{2\sqrt{(C_f+C_j)\tau_0}}\left(C_f+\frac{C_j}{A_0}\right) \tag{4.5}$$

Referring to equation 4.5, if C_f was zero, the damping factor would be relatively small as C_j is divided by A_0, causing the circuit to be underdamped. The inclusion of C_f allows good control of the TIA's stability and prevents its tendency to produce damped oscillation due to the presence of capacitance at its input.

The transimpedance $\frac{V_{out}}{i_{ph}}$ derived with a first order opamp model is given as:

$$\frac{V_{out}}{i_{ph}} = \frac{-A_0R_fr_s}{(A_0r_s+R_f+r_s)\left(1+\frac{R_fr_s\tau_0(C_f+C_j)s^2}{A_0r_s+R_f+r_s}+\frac{((A_0+1)C_fR_fr_s+R_fC_jr_s+\tau_0(R_f+r_s))s}{A_0r_s+R_f+r_s}\right)} \tag{4.6}$$

In reality, opamps have a third order response of the form:

$A_v = \frac{A_0}{(1+s\tau_1)(1+s\tau_2)(1+s\tau_3)}$. The first, second and third poles occur at phase shift of $-45°$, $-135°$ and $-225°$ respectively and can be extracted from the opamp open loop frequency response. However, with a third order opamp model, it is difficult to analytically understand the effect of the feedback capacitor C_f on the circuit stability.

A first order and a third order opamp model were used to numerically analyse the frequency response of the TIA. Numerical results are presented in the following sections.

4.2.2 TIA Noise

The noise performance of a TIA can also be assessed numerically by using a standard opamp noise model comprising equivalent noise current and noise voltage generators, V_n^2 and I_n^2 together with the other circuit components. The signal source, the APD or photodiode, is represented by its internal components, i_{ph}, r_s and C_j. From a noise perspective, the TIA circuit can be represented by Figure 4.3. The voltage noise source due to the feedback resistor R_f is represented by V_{nf}^2.

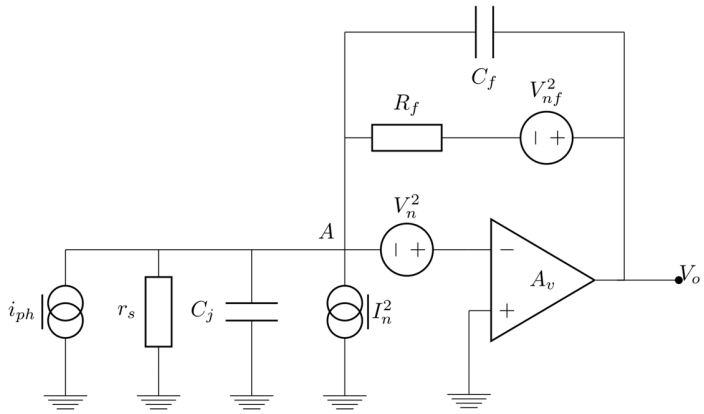

Figure 4.3: Schematic of the TIA noise model showing all of the noise generators and the photocurrent

The total noise at the output V_o is the superposition of each source multiplied by the noise gain from the source to the output. The resulting noise voltages are combined as the rooted sum of the squared values. The output noise voltage resulting from the opamp equivalent voltage noise generator V_n is given by:

$$V_n = -\frac{\left((C_f+C_j)s+\frac{1}{R_f}+\frac{1}{r_s}\right)A_0 V_n}{\tau_0(C_f+C_j)s^2+\left(A_0C_f+C_f+C_j+\frac{\tau_0}{r_s}+\frac{\tau_0}{R_f}\right)s+\frac{A_0}{R_f}+\frac{1}{r_s}+\frac{1}{R_f}} \tag{4.7}$$

The output noise voltage resulting from the resistor R_f, V_{nf}, is given by:

$$V_{nf} = \frac{A_0 V_{nf}}{R_f \tau_0 (C_f + C_j) s^2 + R_f \left(A_0 C_f + C_f + C_j + \frac{\tau}{r_s} + \frac{\tau_0}{R_f} \right) s + A_0 + \frac{R_f}{r_s} + 1} \quad (4.8)$$

The noise voltage resulting from the opamp equivalent input noise current, I_n, is identical to the transimpedance expression (4.6), since it is connected between the inverting input and ground, same as the signal current source. The equivalent noise current and noise voltage generators, V_n^2 and I_n^2 are opamp-dependent and cannot be optimised on a circuit design level. Opamp with suitable V_n^2 and I_n^2 can however be chosen to provide the desired noise level. The only noise component that can be optimised is V_{nf}^2.

4.2.3 Selection of a commercial opamp

Several commercially available opamps (available at the time of design) were reviewed for their noise performance, gain bandwidth product and usability as a TIA. Table 4-1 shows the specifications of some of the reviewed opamp.

Opamp	I_n (pA/√(Hz))	V_n (nV/√(Hz))	Gain Bandwidth Product (MHz)
LMH6624 [113]	2.3	0.92	1500
LMH6702 [114]	18.5	1.83	1700
LMH6733 [115]	18.6	2.1	1000
LMH6629 [116]	2.6	0.69	900
LMP7717 [117]	0.01	5.8	88
MAX4225 [118]	20	2	1000
EL2125C [119]	2.4	0.83	175
EL5166 [120]	19	1.7	1400
THS3202 [121]	20	1.65	2400
AD8432 [122]	2	0.85	200
AD8003 [123]	36	1.8	1500

ADA4899-1 [124]	2.6	1.0	600
OPA695 [125]	27	2.9	1700
OPA3691 [126]	18	2.9	280
EL5130 [127]	1.1	1.8	300

Table 4-1: A list of commercially available opamps reviewed

SPICE simulations of TIAs, built using the opamps from table 2, were carried out. The simulated noise at the output was measured for each opamp TIA. For consistency, a fixed value of 1pF was used for the feedback capacitor and the feedback resistor was varied to look at its effect on the input referred noise current. No optimisation to improve stability and bandwidth was carried out during the initial simulation. From the simulation, TIAs built with LMH6624, EL5130 and ADA4899, among others, showed relatively low level of current noise as presented in Figure 4.4.

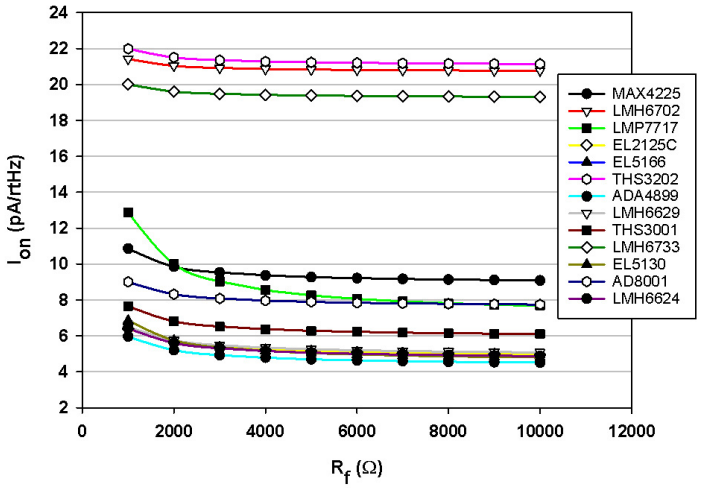

Figure 4.4: Input referred current noise vs R_f for various opamps

The LMH6624 opamp was chosen primarily due to its relatively low input voltage and current noise of $0.92\ \mathrm{nV}/\sqrt{\mathrm{Hz}}$ and $2.3\ \mathrm{pA}/\sqrt{\mathrm{Hz}}$ respectively as an initial opamp for more in-depth analysis and design. The LMH6624 opamp combines a wide bandwidth (1.5 GHz) with low dc-errors to provide precise and wide dynamic range. The LMH6624 opamp is also well suited for high gain wideband operation, with low input current and voltage

offsets.

Noise and bandwidth SPICE simulations for the LMH6624 TIA with different value of feedback resistor are shown in Figure 4.5. A value of 1 pF was used for both the feedback capacitor and for the capacitance seen at the input of TIA circuit.

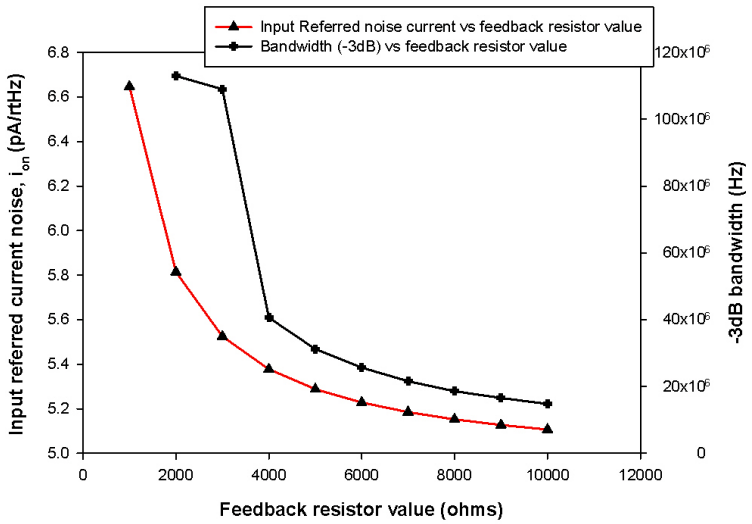

Figure 4.5: Input referred current noise and bandwidth (-3dB) vs R_f for LMH6624 opamp

The SPICE simulation shows an equivalent referred current noise of below the specified $7\ \mathrm{pA}/\sqrt{\mathrm{Hz}}$ for the range of feedback resistor shown. An R_f of $5\ \mathrm{k}\Omega$ will provide the desired minimum transimpedance of 5000 V/A while maintaining a -3dB bandwidth of 31 MHz as shown in Figure 4.5.

4.3 TIA characterisation

Analytical, SPICE and experimental methods are used to assess the TIA based on the LMH6624 opamp. Optimisation of the circuit stability by component selection is explored within the limitations of the specifications listed in section 4.1.

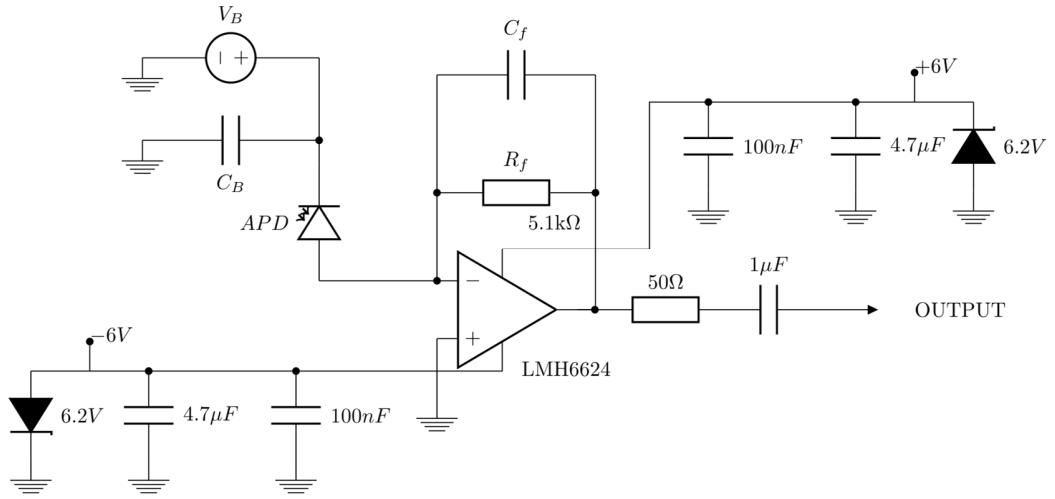

Figure 4.6: Schematic of Transimpedance Amplifier built with LMH6624 Opamp

Section 2.1.3 showed that the opamp TIA's DC transimpedance is equal to the feedback resistor R_f and hence to meet the design specifications, a value of $5.1\text{k}\Omega$ was chosen for R_f.

Using the transimpedance expression given by equation 4.6 and values given in Table 4-3, the frequency response was numerically analysed. A_0 and τ_0 were obtained from the opamp datasheet [113]. The results are shown in Figure 4.7.

R_f	C_j	r_s	A_0	τ_0
5.1kΩ	5pF	1GΩ	6300	1.9μs

Table 4-2: Parameters for 1st order numerical analysis

R_f	C_j	r_s	A_0	τ_1	τ_2	τ_3
5.1kΩ	5pF	1GΩ	6300	1.9μs	0.841ns	0.226ns

Table 4-3: Parameters for 3rd order numerical analysis

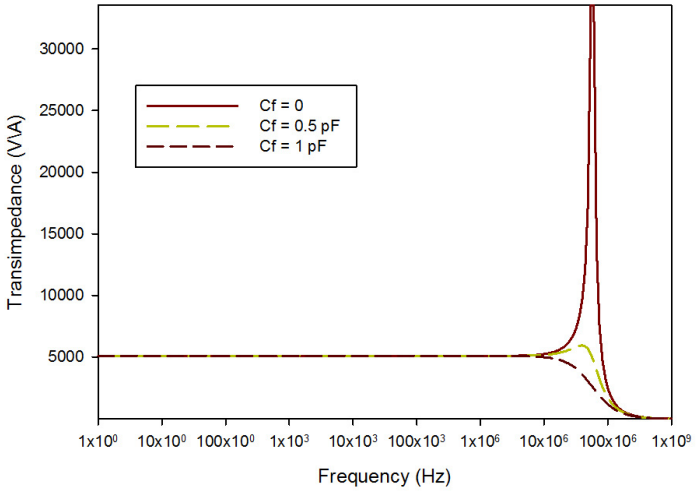

Figure 4.7: Results of numeral analysis of TIA with different C_f

With a feedback capacitor C_f of 0 and 0.5 pF, the circuit is underdamped; resulting in peaking in the transimpedance frequency response as shown in Figure 4.7. A flat response is observed with a C_f of 1 pF. A damping factor of 0.06 and 0.49 is numerically obtained for C_f of 0 and 0.5 pF respectively. With a C_f of 1 pF, a damping factor of 0.89 can be obtained, hence agreeing with the flat response obtained. It should be noted that the response would be maximally flat with a damping factor of 0.7.

The TIA was built and characterised by the method described in section 3.3. The analytical amplitude responses for both first order and third order are shown in Figure 4.8. SPICE simulation with r_s = 1 GΩ and C_j = 5 pF is also presented along with experimental measurement.

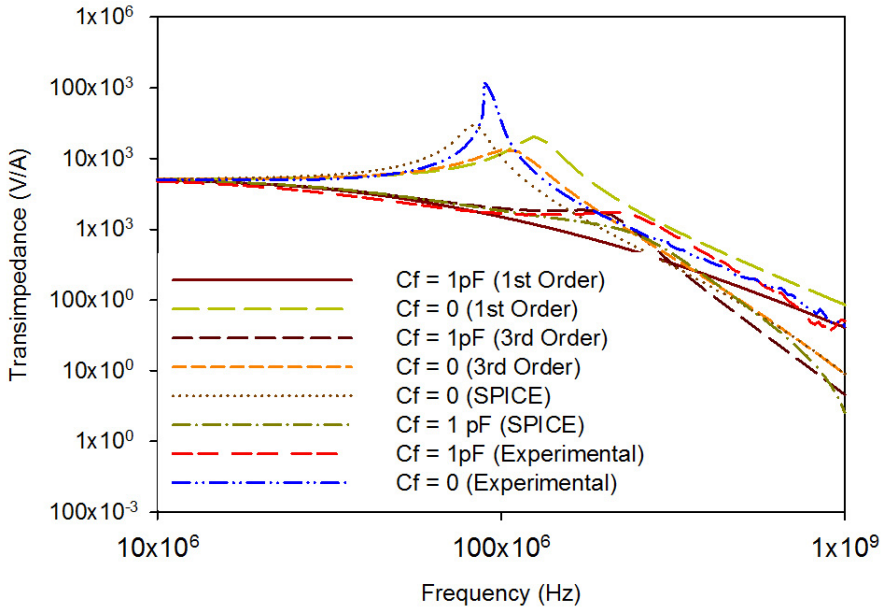

Figure 4.8: Plot of analytical, SPICE and experimental amplitude response of the TIA

The near equivalence of the first order analytical model and the experimental data is depicted in Figure 4.8. An early roll-off can be observed for the first order analytical model. The third order analytical model with more poles and zeros shows slightly better agreement with experiment but the improvement is too small to justify the complication of dealing with a third order analytical model. The first order opamp model is a good predictor of TIA performance over the frequency range of interest.

The TIA was further characterised using the APD approximation circuit described in chapter **3**. The capacitance C_j was varied and the circuit frequency response was measured. The results for C_j ranging between 1 pF to 20 pF are presented in Figure 4.9.

A -3 dB bandwidth of approximately 25 MHz is obtained using the APD approximation circuit with an input capacitance C_j ranging from 0 pF to 8 pF (hence meeting the 7 pF requirement indentified earlier). With an input capacitance of 8 pF, the higher order pole seen in the frequency spectrum around 200 MHz disappears and a -3dB bandwidth is extended to 30 MHz. SPICE simulations showed a -3dB bandwidth of 33 MHz

with C_j of zero, with the bandwidth extending to 42 MHz with a C_j of 8 pF. The peaking around 200 MHz is due to a higher order pole of the opamp.

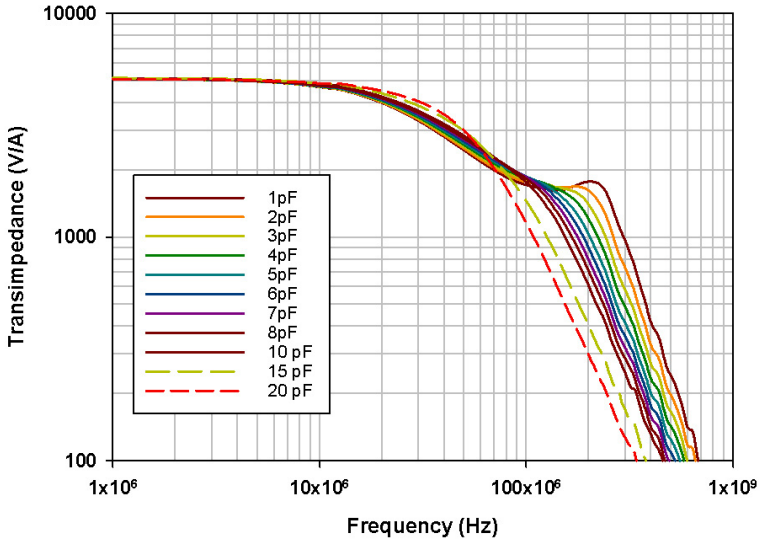

Figure 4.9: Plot of measured frequency response of the TIA with C_j ranging from 1pF to 20pF

4.3.1 Linearity and NEP measurement

It is important that the TIA shows linear response over a wide range of input signals. A fiber-coupled Fujitsu FPD5W1KX InGaAs/InP APD was used to facilitate linearity measurements of the TIA. A block diagram of the measurement system is shown in Figure 4.10.

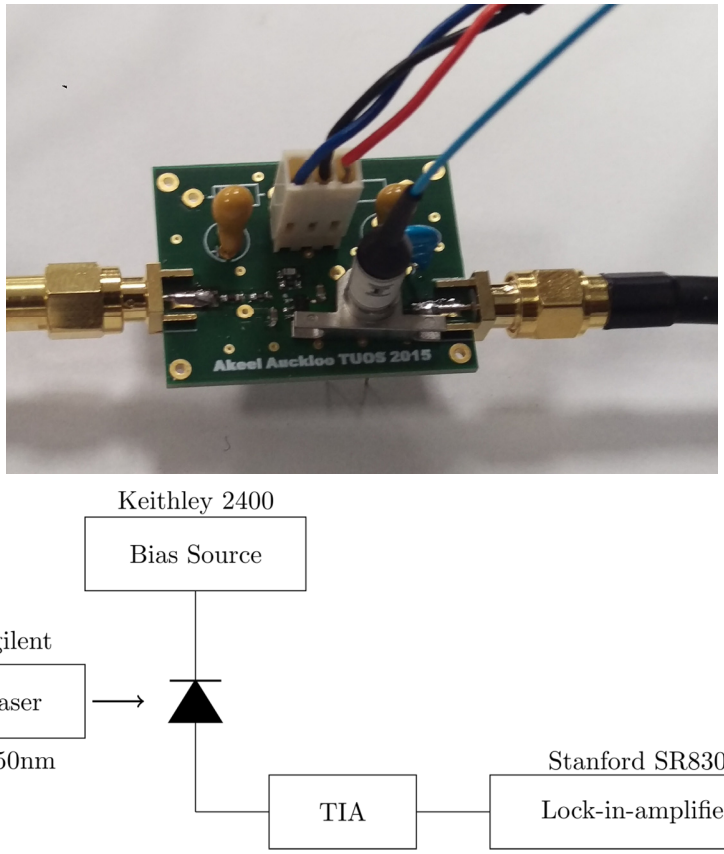

Figure 4.10: TIA with a Fujitsu APD and System block diagram of measurement system

An Agilent 81662A laser modulated at 50 kHz was coupled to the APD. The output of the TIA was connected to a lock-in-amplifier and the APD was biased with a Keithley 2400 SMU. Photomultiplication measurements were carried out on the device and the result is presented in Figure 4.11.

The optical power of the laser was varied and the output voltage of the TIA was measured with a lock-in-amplifier. The measurements were carried out with the APD biased at 30V, 35V and 40V corresponding to avalanche gain of 2, 2.6 and 3.6 respectively as shown in Figure 4.11. Figure 4.12 shows a linear response for an optical laser power ranging from

$\sim 10\ \text{pW}$ to $\sim 35\ \mu\text{W}$. As expected the TIA output increases and is linear for input signal ranging from $\sim 10\ \text{pW}$ to $\sim 35\ \mu\text{W}$ .The maximum laser power available is limited to the maximum deliverable power of the laser itself, the loss in the fiber and the responsivity of the APD. The Standard Error of Estimate of 2.1 x 10^{-18} of the graph shown in Figure 4.12 was obtained by performing a non-linear regression - dynamic fitting in Sigmaplot. This is smaller than the define 0.1% specified in the design requirements.

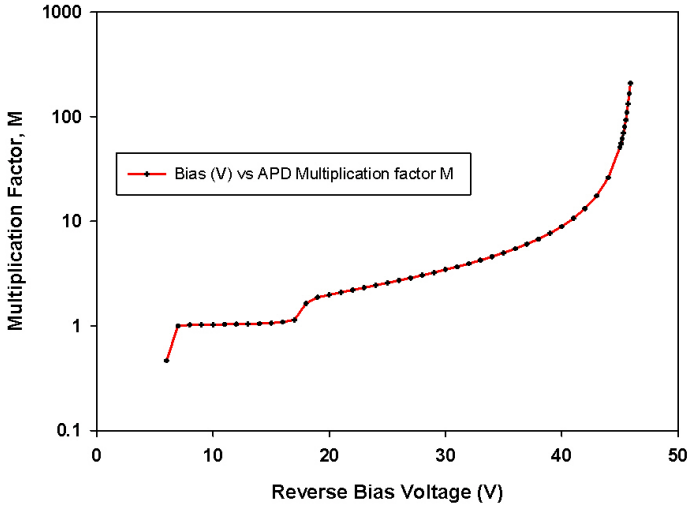

Figure 4.11: Fujitsu APD gain curve

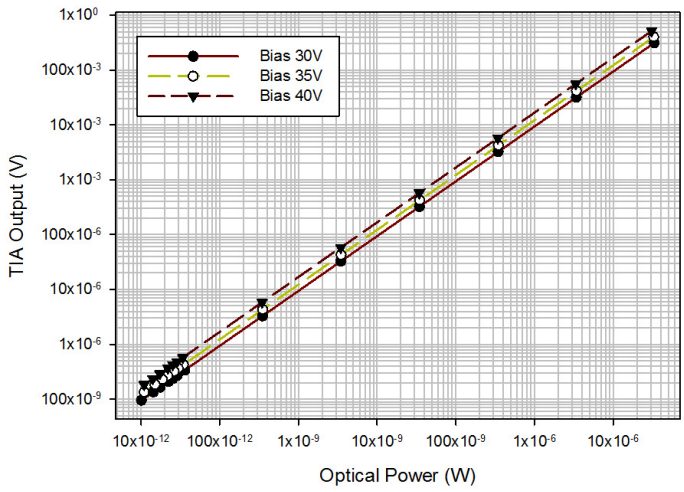

Figure 4.12: Graph showing experimental measurements of optical power vs TIA output voltage

Using the NEP equation 4.1 and parameters shown in Table 4-4, the calculated minimum detectable laser power was found to be ~1 pW. The calculated value only takes noise contribution from the APD and TIA into account; noise from the biasing source were not included.

Dark Current	150 nA
TIA input referred noise	3 pA/√Hz
APD multiplication factor	200
Excess noise factor F	18
Responsivity	0.8 A/W

Table 4-4: Parameters used to calculate NEP for Fujitsu APD with the TIA

To obtain the minimum detectable laser power, the response of the APD+TIA to the 1550 nm laser was measured on a spectrum analyser. The spectrum analyser centre frequency was set to 50 kHz and a span of 100 Hz was used. The resolution bandwidth of the spectrum analyser was set to 1 Hz. The laser optical power was reduced until the signal was not detectable on the spectrum analyser. The APD was biased close to breakdown (46 V) to get the maximum APD gain and the laser power was varied down to ~2 pW. The results are presented in Figure 4.13 and the laser power is shown in the legend box. The lowest detectable laser power was found to be ~2.6 pW with the fibre losses taken into account.

However, it should be pointed out that the dark current of the APD is relatively high and will contribute to the noise of the setup. In an ideal setup, it is usually desirable to have APDs with dark current low enough such that their noise contribution is negligible. The gain of the APD was varied and the response of the setup was measured with a fixed laser power of 26 pW. The data is shown in Figure 4.14. From 44.8V to 45.5V, it can be observed that the signal, at 50 kHz, increases due to the benefit of the APD gain while the noise floor remains relatively consistent. With the bias voltage pushed beyond 45.5V, the noise floor increases due to increased dark current.

The same experiment was performed using the APD and commercial low noise

transimpedance amplifier (Standford Research SR570). The gain of the commercial TIA was set to 5000 V/A. The results, presented in Figure 4.15, shows a minimum detectable laser signal power of 26 pW. The noise floor of the SR570 is considerably higher than the noise floor of the designed TIA. The minimum detectable laser power is ten times higher for the SR570.

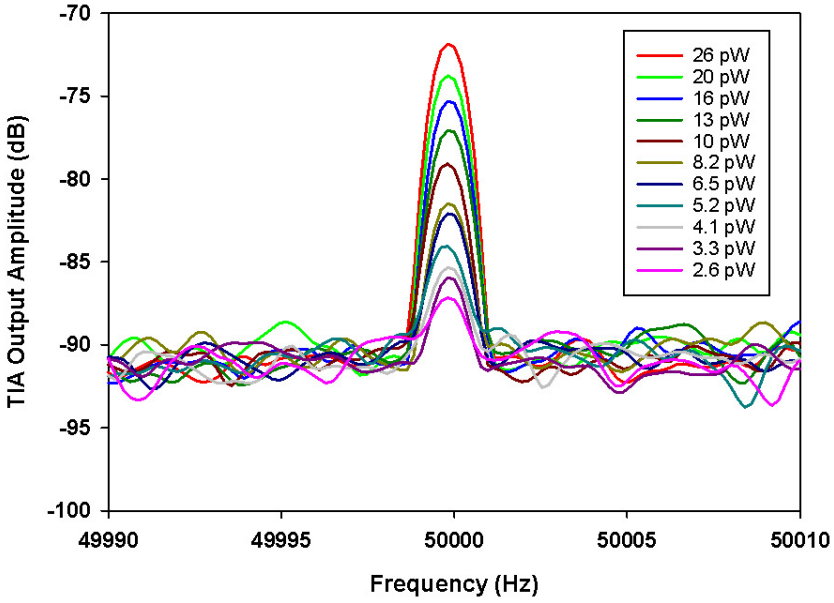

Figure 4.13: Data of TIA output Amplitude with varying laser power

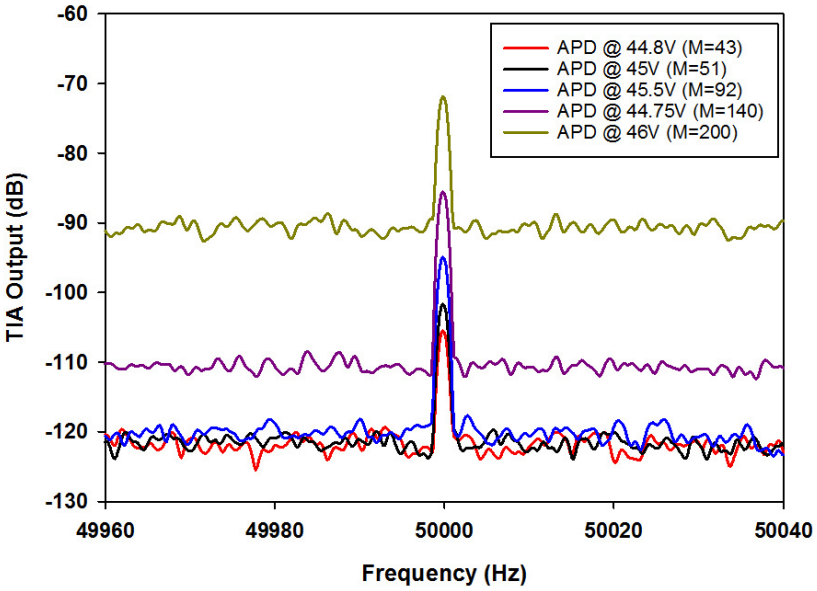

Figure 4.14: Data of TIA output Amplitude with increasing APD Gain and fixed laser power of 26 pW

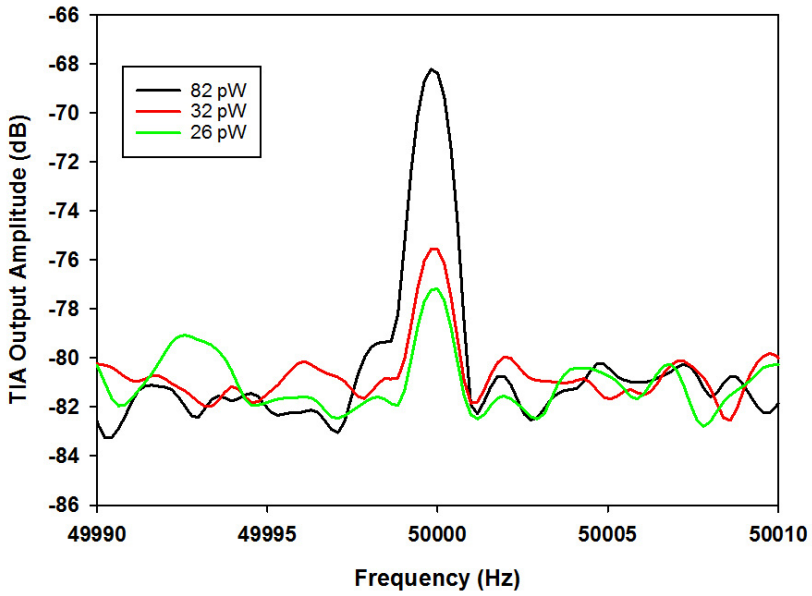

Figure 4.15: Data of Fujitsu APD connected to commercial SR570 TIA

4.3.2 Miniature pre-amplifier

For the early prototypes of the miniaturised pre-amplifiers, the frequency responses were not measured as they were expected to have the same responses as the full sized ones. It is also difficult to reliably measure the responses due to the limited ways of making connections to the bond pads.

Figure 4.16 shows a miniaturised TIA with a Si photodiode connected at the input. All the connections were soldered to the bond pads. This TIA was however found to be susceptible to interference due to the small copper tracks and the unshielded cable behaving similar to antennas, also known as trace antennas. The noise spectrum of this setup is presented in the noise section. The setup shown in Figure 4.16 provided unreliable measurement due to its susceptibility to background interference. To overcome some of the problems, a test rig also shown in Figure 4.16 was built. A 633 nm laser chopped at a frequency of close to 3 kHz was shone on the BPX65 with TIA + rig. The output of the pre-amplifier is shown in Figure 4.17.

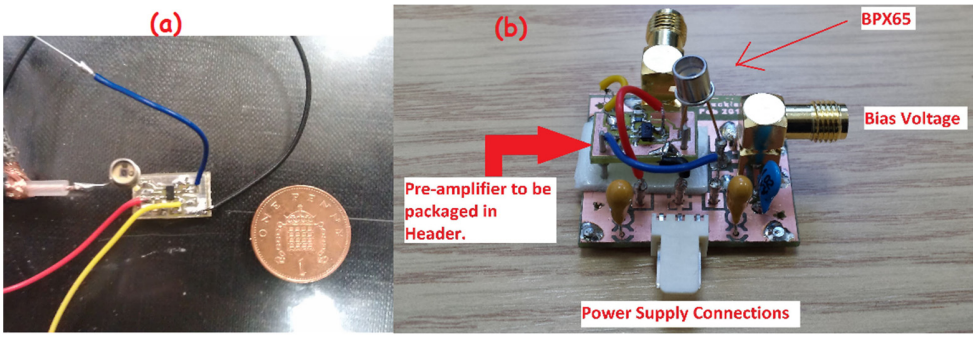

Figure 4.16: Miniaturised TIA with (a) BPX65 and (b) with test rig

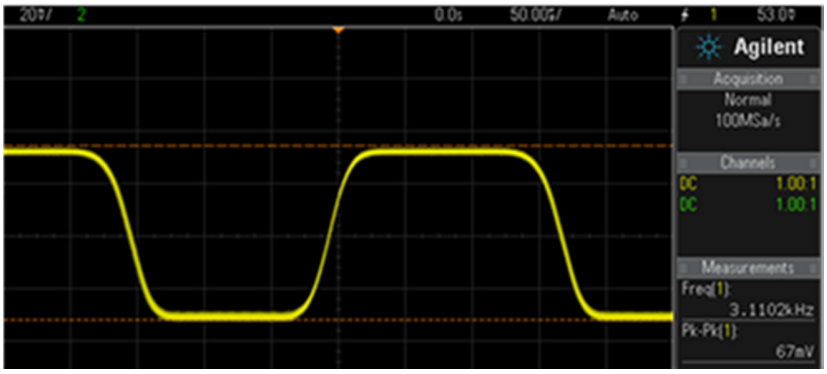

Figure 4.17: Output of test rig +TIA when a Si diode was illuminated using a 3 kHz modulated laser

4.3.3 Noise measurement

For initial noise characterisation of the miniature PCB, the input of the pre-amplifier was grounded with a 50 Ω resistor. Figure 4.18 presents the measured noise and simulated noise in $V/\sqrt{Hz}$ while Figure 4.19 shows a simplified schematic of the pre-amplifier with all the major noise sources. The output of the pre-amplifier was connected directly to the input of the HP 4396B spectrum analyser and the noise was measured in dBm/Hz.

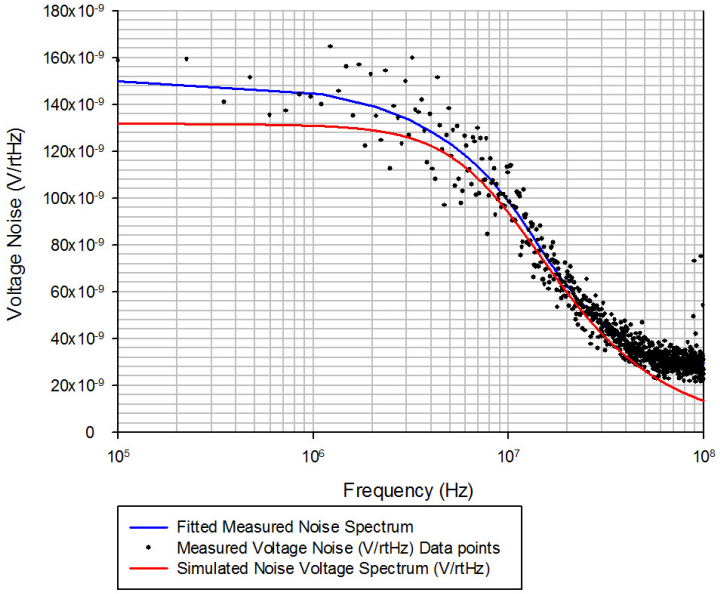

Figure 4.18: Measured and Simulated Noise Spectrum of the TIA with input grounded through 50 Ω

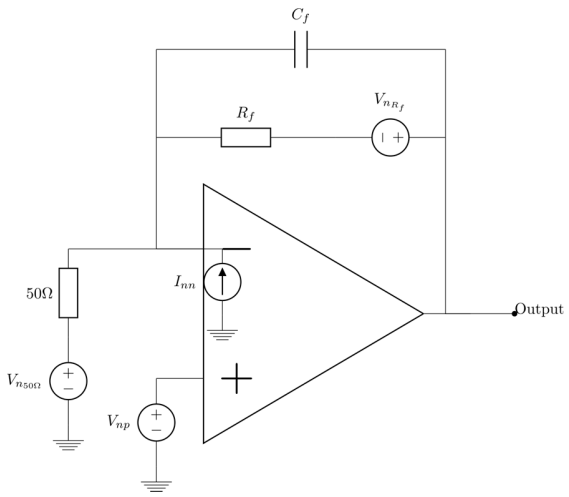

Figure 4.19: Noise Model of TIA

Using a 50 Ω resistor at the input of the pre-amplifier confirmed that the spice simulations are in agreement with actual circuit measurement. To further evaluate the pre-amplifier with a detector, a biased Si photodiode (BPX65) was connected at the input. A Keithley SMU was initially used to bias the photodiode but was found to couple undesirable noise components to the pre-amplifier causing a higher voltage noise to be measured from the pre-amplifier output. A more accurate voltage noise was measured by using lead acid batteries to bias the photodiode. The schematics of the circuit used with the BPX65 is shown in Figure 4.20

The noise voltage at the pre-amplifier output was found to be small relative to the noise floor of the HP4396B spectrum analyser. A MiniCircuit ZFL-500LN was used to amplify the noise before being measured by the spectrum analyser. The result is presented in Figure 4.21.

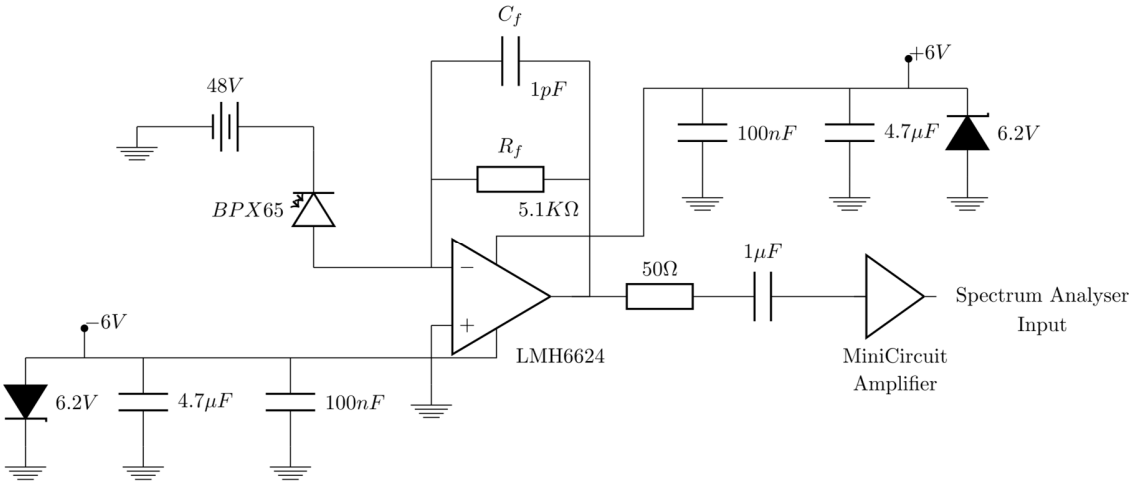

Figure 4.20: Schematic for noise measurement with Si BPX65

Analytical and SPICE noise performance are also shown in Figure 4.21. The analytical model was derived with the third order opamp model. All data presented in Figure 4.21 are for 50Ω matched systems.

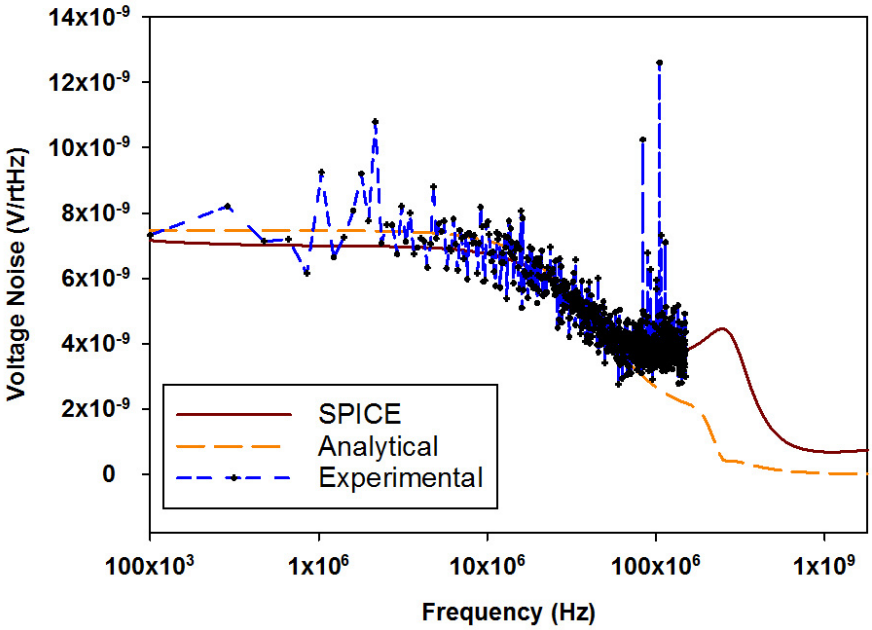

Figure 4.21: Noise spectrum of the TIA

The experimental noise spectrum was measured using a spectrum analyser that was capable of measuring noise density at frequencies up to 150MHz. The sharp peaks around 100 MHz are due to background FM transmission.

Figure 4.21 shows that the analytical, SPICE and experimental results are comparable in terms of trend and voltage noise. A voltage noise density of approximately 7 $\mathrm{nA}/\sqrt{\mathrm{Hz}}$ is observed at the lower end of the frequency range and this corresponds to a input noise current density of $\approx 3\ \mathrm{pA}/\sqrt{\mathrm{Hz}}$.

The noise current spectrum was integrated over the bandwidth of the circuit to get an average input noise current of $\approx 2.6\ \mathrm{pA}/\sqrt{\mathrm{Hz}}$. SPICE simulation for a frequency range of 1 Hz to the -3dB bandwidth gives an input equivalent current noise of $\sim 2.8\ \mathrm{pA}/\sqrt{\mathrm{Hz}}$. The start frequency for the measured noise response was however set to 100 kHz due to the limitation of the spectrum analyser. This could account for the lower equivalent input noise current.

4.3.4 Temperature stability of the TIA

An attempt to measure the temperature stability of the TIA was carried out. An unbiased InAs diode was placed at the input of the TIA and the output voltage of the TIA was sampled with a digital multimeter in order to get a gain stability value. Here the stability is defined as follows:

$$Stability(\%) = \frac{Standard\ Deviation\ of\ sampled\ voltages}{Mean\ Value\ of\ the\ sampled\ voltages} \times 100 \qquad (4.9)$$

The APD and the TIA (shown in Figure 4.22) were placed in a custom-made box kept at a constant temperature by means of a Peltier cooler. The temperature inside the box was kept at 20°C.

The box, used to facilitate the measurement, is shown in Figure 4.23. A Keithley 2510 TEC Sourcemeter was used to control the temperature inside the box. The Peltier is attached to the outside of the diecast box and causes the whole box to become cold which subsequently cools the air inside the box to 20°C. The temperature of the air inside the box was monitored using a platinum RTD sensor and logged using a Labview program. The

temperature of the box was allowed to settle to 20°C ±0.1°C before the output from the pre-amplifier was recorded.

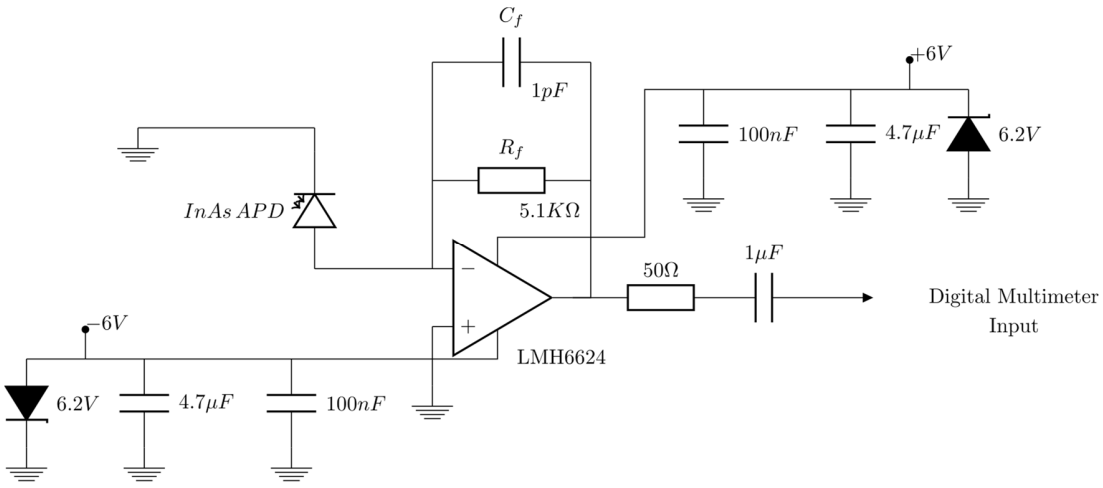

Figure 4.22: Setup for stability test

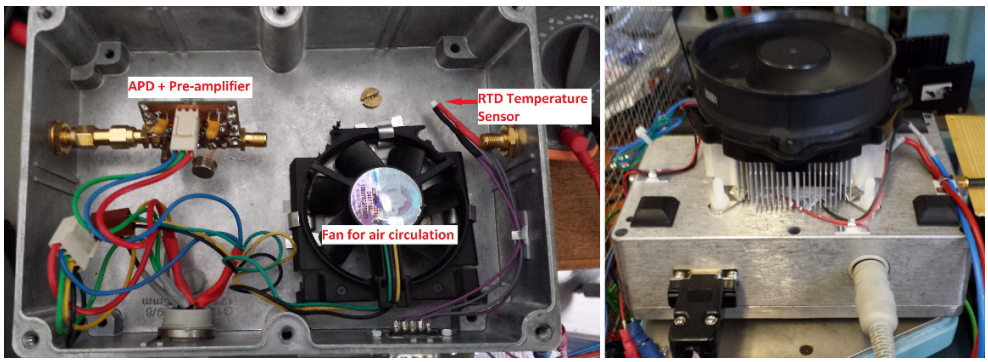

Figure 4.23: Box used to facilitate stability measurement-inside and outside views

An Agilent 34401a digital multimeter was used to sample the output of the pre-amplifier. The multimeter was set to measure AC RMS Voltage. The waveform shown in Figure 4.24 represents measured pre-amplifier output voltage against sample number (time). The x-axis represents sample count. The sampling rate used was 0.5 sample/second. Due to the unoptimised PID control, it takes more than 1000 s before the temperature

stabilizes. Taking samples between 1000 to 2500 s into account, a stability of 0.21 % was obtained at the output of the TIA. It is thought that this fluctuation is caused by the dark current from the InAs diode.

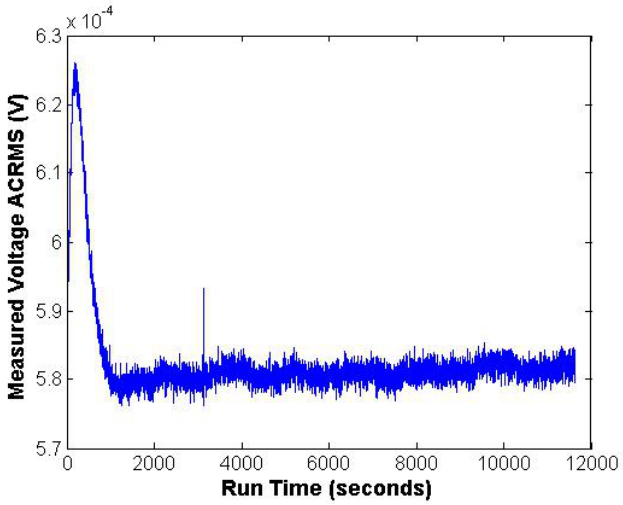

Figure 4.24: Measured Pre-amplifier output vs time

4.4 Testing of final TIA

The TIA design was manufactured on various PCB substrates (FR4, Ceramic, RogerCorp) and the TIA circuit showed no improvement over standard FR4 in terms of noise. As a result, the TIA was manufactured on a 1.6 mm FR4 substrate with a 35 μm layer of copper using standard PCB manufacturing process. The bond pads were finished with an Electroless nickel immersion gold.

The miniature TIA presented an attractive way of packaging both the APD and the TIA in a single module. The size of the TIA is constrained by the size of the components and the PCB track size. The size of the PCB was reduced so that it would fit in a 9-pin HHL package without compromising the performance of the TIA. Figure 4.26 shows an assembled TIA.

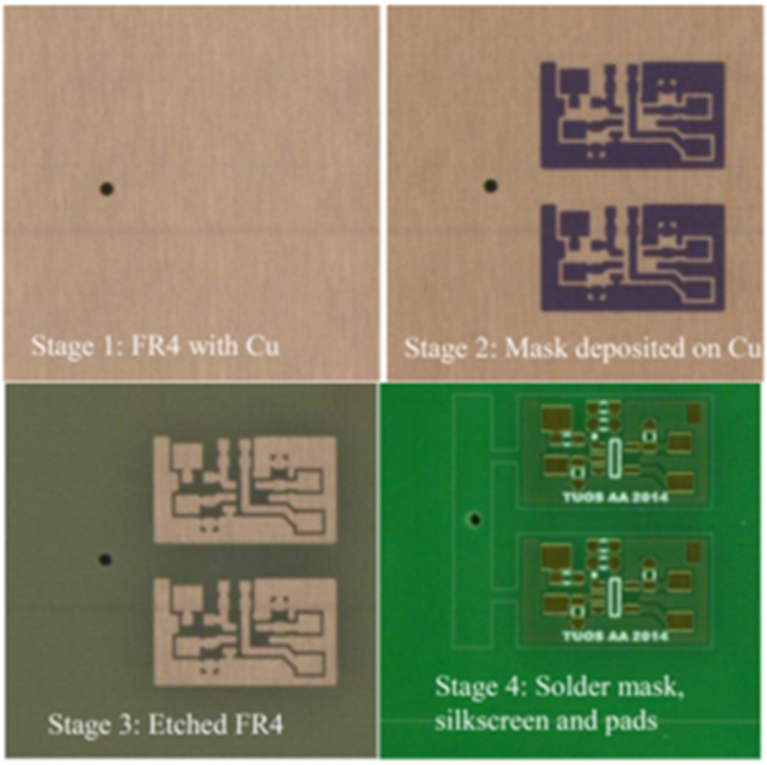

Figure 4.25: PCB manufacturing stages

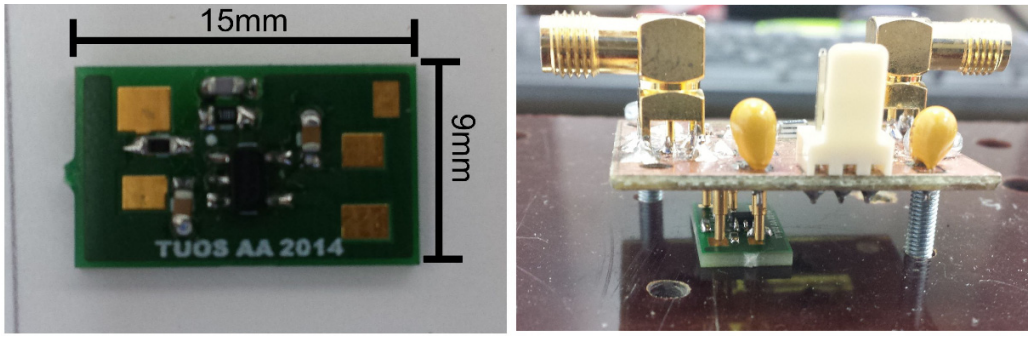

Figure 4.26: TIA with bond pads and mounted on a test rig.

Good connections to the gold-plated bonding pads are essential to allow a reasonable testing to be carried out but however it is vital that the pads are not damaged during testing, therefore making soldering inadequate in this case. A test rig with spring loaded probes was built to enable the testing of the TIAs (also shown in Figure 4.26). The

test rig consists of the APD approximation circuit and facilitates the measurement of the TIA frequency response.

The network analyser's RF output power was changed from -60 dBm to 0 dBm. The experimental results are shown in Figure 4.27. The decaying trend between 100 kHz and 200 kHz is due to measurement errors and is associated with the network analyser. A (-3 dB) bandwidth of 22 MHz is observed. This is lower than previously reported (25 MHz). The reduced bandwidth is due to the reduced contact between the spring loaded probes and the TIA. The bandwidth is expected to be 25 MHz when packaged in the header.

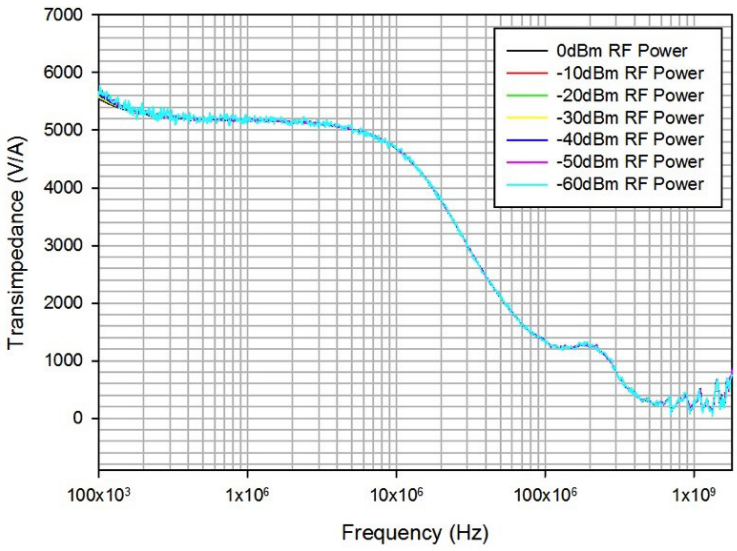

Figure 4.27: Frequency Response of one of the assembled TIA

4.4.1 Performance of the TIA with an InGaAs APD

Due to the delay in acquiring InAs APDs, the TIA was packaged with an in-house InGaAs/InAlAs APD on a ceramic header as shown in Figure 4.28. The TIA and the APD were hand-bonded with silver epoxy and gold wires. The measured capacitance and dark current as functions of reverse bias voltage of the InGaAs APD are shown in Figure 4.29. It can be seen that when fully depleted the APD with a radius of 208 μm has a capacitance of

10pF, while the breakdown voltage is approximately 40 V.

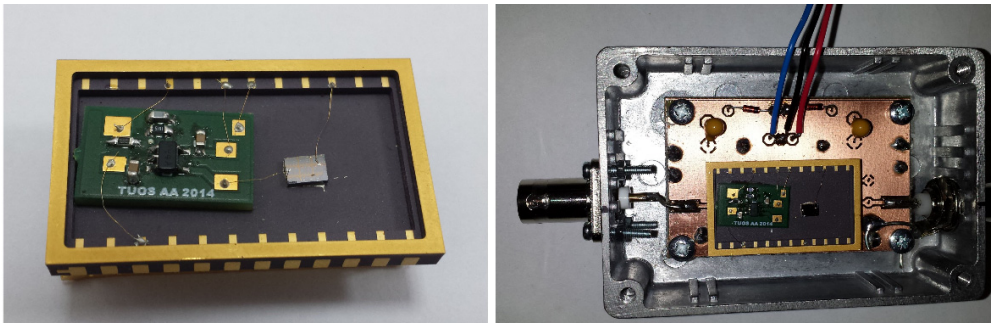

Figure 4.28: TIA Packaged with a home-grown InGaAs APD and mounted in a diecast box

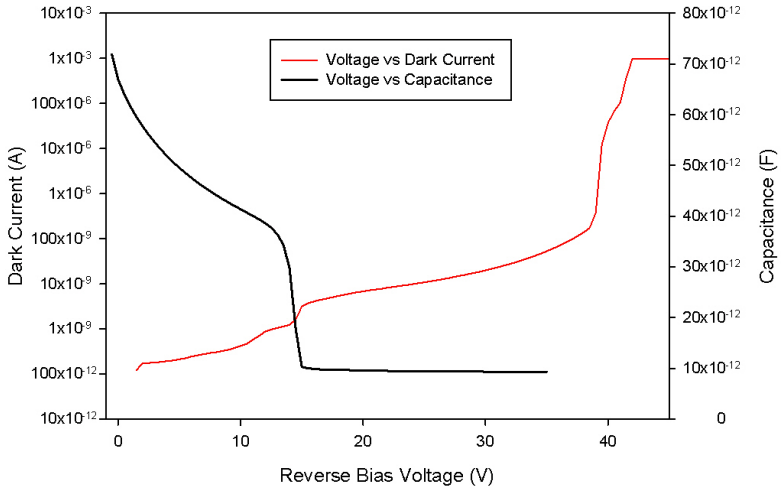

Figure 4.29: Capacitance-Voltage and Dark Current-Voltage measurements of the InGaAs/InAlAs APD

The header was soldered to a PCB and placed in a diecast box in order to facilitate testing as shown in Figure 4.28. The APD was biased past punch-through to 15 V with a Keithley source measure unit. A -/+ 6 V linear power supply was used to power the preamplifier. A pulsed injection laser from Advanced Laser Diode Systems (EIF1000D) together with a 1550 nm laser head were used to shine optical signal onto the APD. The

pulses emitted by the laser have a width in the region of ≈50 ps; this value was obtained from the datasheet of the equipment. The preamplifier output was connected to an Agilent oscilloscope. A pulse repetition ranging from 50 kHz to 1 MHz was used. Figure 4.30 show the measured output with repetition of 1 MHz. The measured pulse width was less than 50 ns. It is not possible to determine whether the system is limited by response of the InGaAs/InAlAs APD but the results showed that the amplifier will be suitable for pulses of 50 ns or longer.

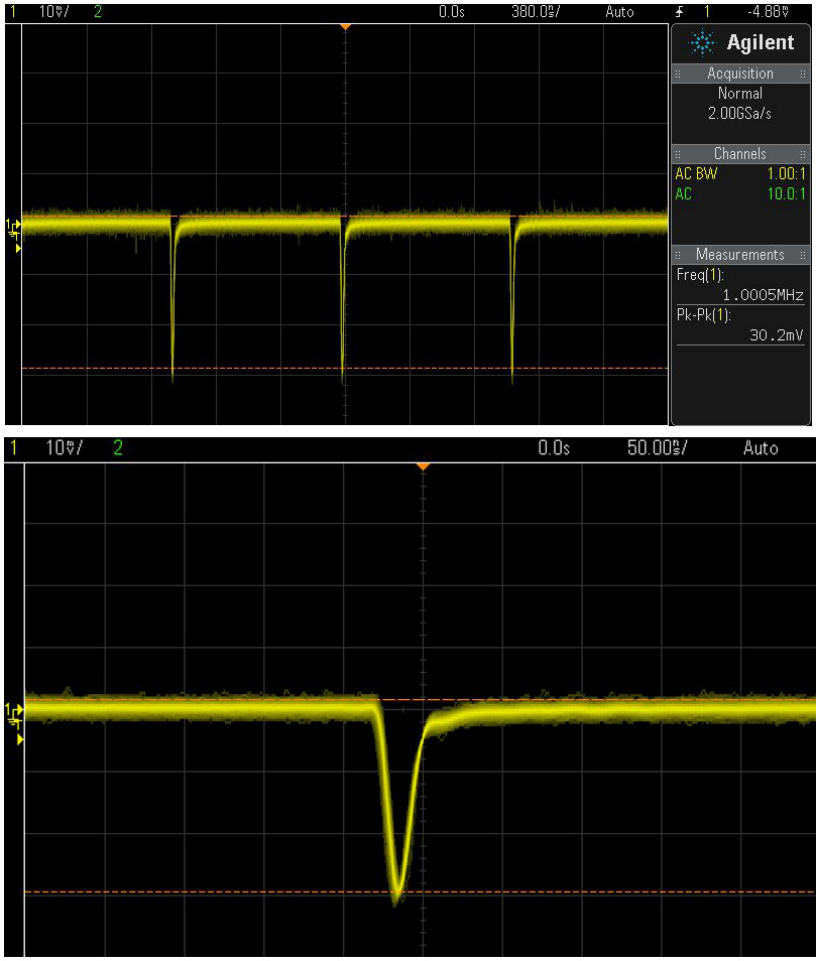

Figure 4.30: Output of preamplifier with a pulse repetition of 1 MHz and with a width of less than 50 ns

4.5 Comparison with other published TIAs

Several TIAs mainly built for excess noise measurement systems are reported in literature and comparison between reported work and this work may be drawn. Signal-to-noise ratio of several TIAs is reported in [128]. For the signal-to-noise ratio calculations presented in [128], the signal is taken as full shot noise defined by 1 μA.

The signal-to-noise ratio is given by:

$$\mathrm{SNR} = \frac{2qI}{(\text{Input noise current density})^2} \tag{4.10}$$

where I is 1 μA and q is the charge of an electron.

Table 5: Comparison of published TIAs

Author	SNR (dB)
Bulman *et al* [128]	-36.72
Xie *et al* [129]	-31.58
Ando and Kanbe [130]	-23.98
Brain *et al* [131]	-33.37
Lau *et al* [132]	-25.70
Green *et al* [128]	-34.75
This work	-27.43

Table 5 shows a comparison of signal-to-noise ratio (SNR) of published TIAs [128-132]. Lau *et al* [132] and Ando et al [130] show the best SNR and this work demonstrating similar SNR. However, Lau *et al* [132] TIA has a smaller bandwidth compared to the design described here. The authors in [128] argue that no noise specifications are given for the Ando and Kanbe TIA and that only the noise power available within a specific bandwidth is compared with the signal, which makes the value given in table 5 for SNR not suitable for comparison.

4.5.1 InAs LIDAR receiver

As part of the contract with ESA, several TIA circuits along with Sheffield-grown InAs APD were sent to ISDEFE, a sub-contractor, for packaging and testing. The results presented in this section were carried out by ISDEFE.

A photograph of a packaged APD-TIA module is shown in Figure 4.31. The APD is mounted on a four stage Peltier and is bonded to the TIA with gold wire and silver epoxy. The power supply contacts and output of the TIA are also bonded to the pins with gold wire and silver epoxy. The TIA circuit is mounted on polyphenylene sulfide (PPS) pillars. PPS was used as they are insulating, preventing the heat from the back of the case to be transferred to the PCB.

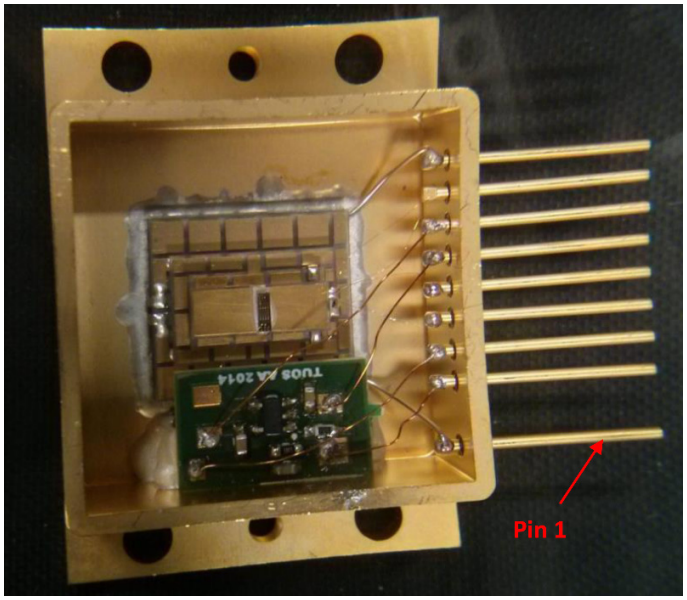

Figure 4.31: Photograph of a packaged APD-TIA (Courtesy of ISDEFE)

A pulsed laser was used to obtain the temporal response of the APD-TIA module. The response of the module to a 50 ns laser pulse, 8000 photons per pulse and a 100 kHz repetition rate is shown in Figure 4.32. Figure 4.33 shows the response of the module with a laser pulse repetition frequency of 1 kHz and 2×10^6 photons per pulse. These values were specified by ESA.

The response of the module to a laser modulated at 80 Hz is shown in Figure 4.35.

The linearity of the module versus optical power was measured and is presented in Figure 4.34. The APD-TIA combination is linear in the range of interest (2×10^6 photons per pulse of 50 ns to 8000 photons per pulse of 200 ns).

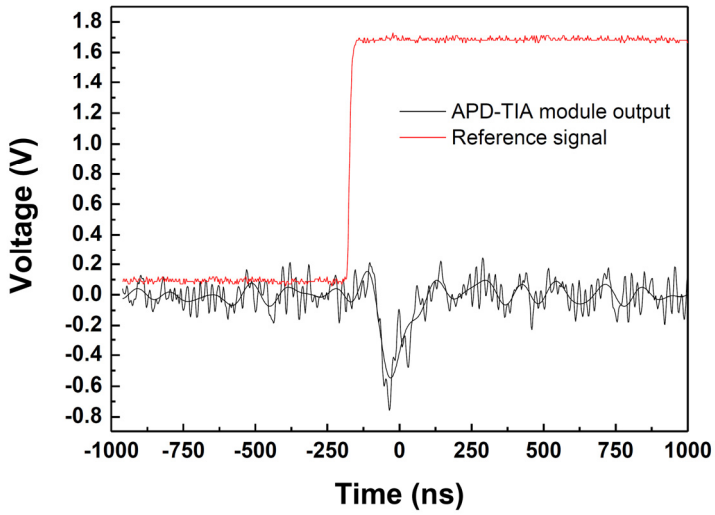

Figure 4.32: Temporal response of a detected pulse of 50 ns for a repetition rate of 100 kHz at 208 K.(Courtesy of ISDEFE)

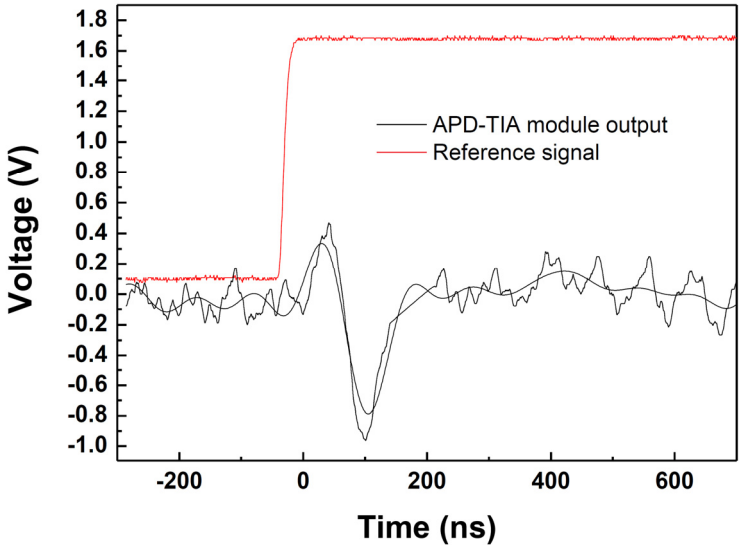

Figure 4.33: Temporal response of a detected pulse of 50 ns for a repetition rate of 1 kHz at 207 K. (Courtesy of ISDEFE)

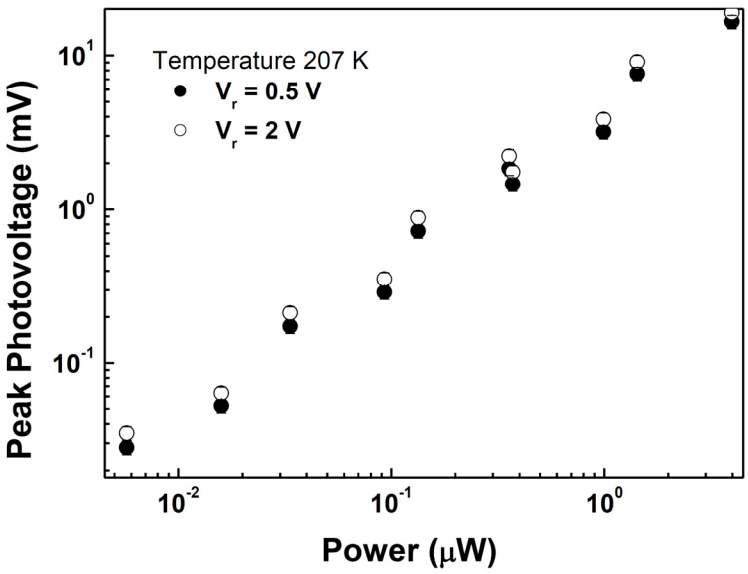

Figure 4.34: APD-TIA module output voltage versus laser optical power (Courtesy of ISDEFE)

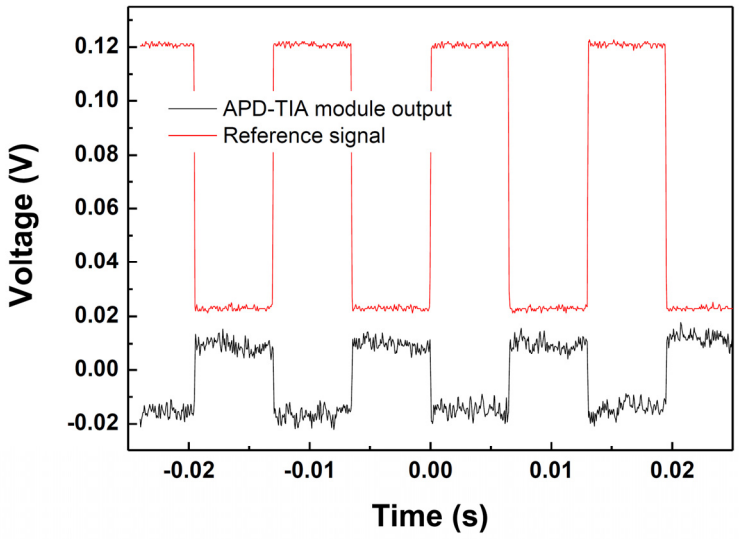

Figure 4.35: Response of the APD-TIA module with a modulated laser signal (Courtesy of ISDEFE)

The module was also tested with a square-modulated laser and the results are shown in

Figure 4.35. The results shows a square transient response with no underdamped behaviour.

4.6 Conclusion

Numerical analysis has been used to facilitate and verify the design of an opamp TIA. A near equivalence of the first order analytical model and the experimental data was observed. The third order analytical model with more poles and zeros shows slightly better agreement with experiment but the improvement is too small to justify the complication of dealing with a third order analytical model. The first order opamp model is a good predictor of TIA performance over the frequency range of interest. The TIA was built and tested with various semiconductor devices. Although the TIA circuit looks simple, careful design procedures has been undertaken using analytical and SPICE method to provide the best performance within the ESA specifications.

The proposed TIA circuit was compacted in a physically small package with bondpad and was packaged with an InAs APD as part of the contract with ESA. The InAs TIA-APD module were successfully tested by Isdefe and were deemed to meet the specification of ESA. The -3dB bandwidth is greater than the specified 20 MHz. Low noise performance was achieved with minimal design and construction cost.

The TIA was tested with Sheffield-grown InGaAs/InAlAs APD and a commercial InP Fujitsu APD. Resonable NEP was achieved with the InP APD. Further testing of the circuit with InAs APD should be carried out when the APDs are grown and fabricated.

The following chapter presents a low noise charge sensitive amplifier suitable for low energy X-ray spectroscopy.

Chapter 5 A Low Noise Charge Sensitive Amplifier

The previous chapter presented a low noise TIA, a circuit capable of converting a current signal into a voltage signal. This chapter presents a low noise Charge Sensitive Amplifier for converting a charge signal into a voltage signal.

5.1 Introduction

The interaction of X-ray photons with a semiconductor photodiode detector leads to creation of charges within the photodiode which then appear as charge pulses at the detector terminal. For wide bandgap semiconductors, the electron hole pair creation energy is relatively high resulting in a small amount of created charge for each absorbed X-ray photon. The amplitude of the current pulse is then small, making it challenging to measure. For high energy radiation detection, the noise level of commercially available electronics can be sufficiently low compared to the inherent detector noise contributions, giving acceptable energy resolution since the total charge created by photons is relatively high. However, for the measurement of X-ray photon energy below a few keVs, the contribution of noise of the electronics can be significant. Therefore, for soft X-rays spectroscopy below a few keV, there is still a strong motivation to reduce the noise contribution of the electronics.

Since it is the total charge created by the X-ray photon - photodiode interaction that is of interest, the current pulse from the photodiode is usually integrated by a charge sensitive amplifier. Charge sensitive amplifiers operate by converting a quantity of charge into a voltage by collecting the charge on a capacitor. The simplest scheme would be a capacitor followed by a voltage amplifier but the noise contribution of the voltage amplifier can be significant.

A better scheme is to integrate the input charge in a capacitor in the feedback path of an inverting amplifier configuration as shown in Figure 5.1. C_1 is the parasitic input capacitance and C_2 the integrating feedback capacitance. The amplifier *U1* may or may not be an integrated opamp.

Since the amplifier has a large inverting gain, *Av*, the Miller effect makes C_2 look like

a much larger value of capacitance $(C_2(1-A_v))$ in parallel with C_1. If a suitable value of Av is chosen, the Miller multiplied C_2 will be much larger than C_1 so most of the input charge will end up in C_2. The voltage across C_2, which is approximately equal to v_{out}, will then be $v_{out} \approx Q_{in}/C_2$.

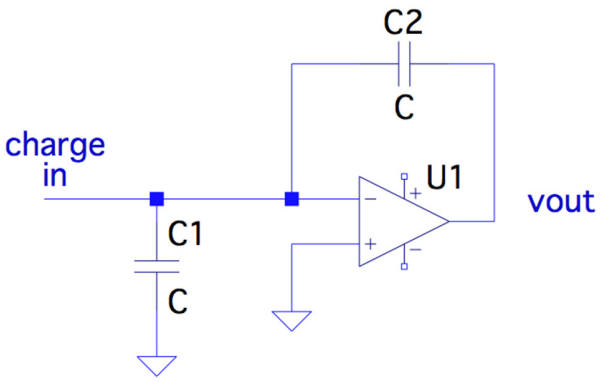

Figure 5.1: Charge integrator

This circuit ensures that most of Q_{in} ends up in C_2 even though C_2 can be much smaller than the parasitic capacitance at the input, C_1. For X-ray spectroscopy applications, the nature of U_1 is of crucial importance; the noise performance of the charge amplifier is a key player in the resolution of the system. One of the most effective charge amplifiers in the literature is one by Bertuccio [57] and the work described in this chapter builds on his design.

Bertuccio [57] [133] reported a novel low noise charge sensitive preamplifier with an equivalent noise charge (ENC) of 19.5 electrons r.m.s with a shaping time of $10\mu s$. Bertuccio's CSP is the lowest noise discrete circuit reported in literature. Advances in CMOS and ASIC have led to lower noise integrated circuit [134-136]. Bertuccio [137] has demonstrated a ultra low noise ASIC CSP, with an ENC of 5.2 electrons r.m.s at a shaping time of 2 µs dropping to 3.9 electrons r.m.s. with a shaping time of 12 µs.CSPs are also available commercially from companies such as Amptek. Amptek quotes an ENC of 76 electrons r.m.s for their cooledFET product [67]. However discrete analog circuits still

remain a viable option for designing low noise charge sensitive preamplifier due to cost and adaptability for measuring Sheffield-grown semiconductor detectors with different range of capacitance and leakage current.

Most commercial charge sensitive preamplifiers come with a pre-packaged fixed value biasing resistor and this can be problematic under particular conditions when APDs are characterised. When APDs are operated at high gains, a small drop in bias voltage can cause a significant drop in APD gain. Bias resistors are usually connected in series between the bias voltage source and the APD and the APD's leakage current flows through the bias resistor, causing a voltage drop across that resistor. This voltage drop is then taken into account to work out the voltage across the APD. Any changes in the APD's leakage current, due to a change in temperature for instance, will cause a change in the bias resistor's voltage drop and hence a change in the APD gain. Fluctuations in APD gain can be detrimental to energy resolution. An in-house CSP can provide more flexibility in the value of the bias resistor. In some cases, if the bias voltage source is electrically clean and stable, the bias resistor can be removed and the bias source can be applied directly to the APD.

This chapter describes the design and characterisation of a low noise charge sensitive preamplifier, built using commercially available discrete components.

5.2 Practical low noise CSP circuits

The CSP circuit described in this work was based on a circuit used by many low energy X-ray spectrometrists. The circuit uses a discrete FET input amplifier with an integrating capacitor in its feedback circuit as shown in Figure 5.2.

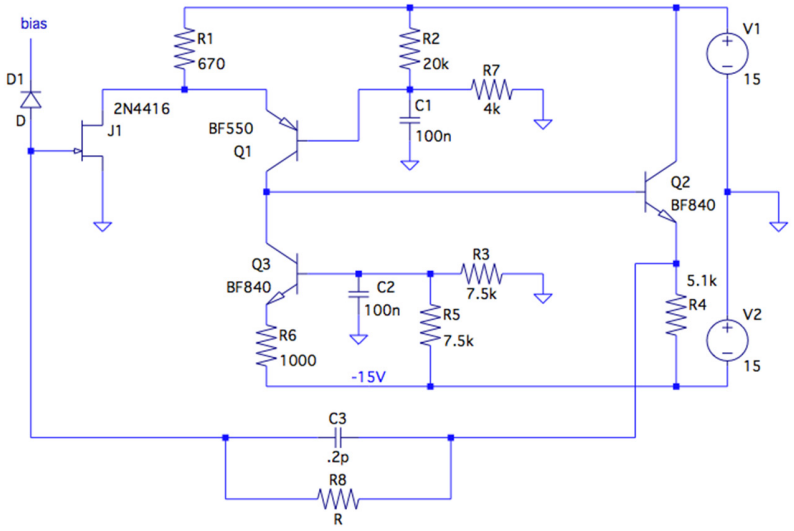

Figure 5.2: Practical low noise CSP circuit

The input FET, J1 together with Q1 forms a folded cascode input stage. The folded cascode circuit behaves in a similar way to a normal cascode circuit but has the advantage that it can, with careful design, be made to provide a dc output which can be set at around zero volts.

The circuit of Figure 5.2 “resets” the charge integrator capacitor, C3, by using a high value resistor, R8. Any detector dark current will flow through R8 and will generate a voltage across it. A high dark current will require a relatively low R8 if amplifier saturation is to be avoided; a low dark current allows the choice of a much larger R8. For example a dark current of 1 nA through an R8 of 1 GΩ would produce a dc offset of 1 V at the output, a figure that would normally be acceptable. For this type of reset to work properly one would want τ = C3.R8 to be very long compared to the width of the current pulse caused

by X-ray interaction with the detector and short compare to the time interval between these interactions. These are not easy conditions to satisfy.

The presence of R8 also degrades the noise performance of the circuit [57]. Because of the noise implications of R8, many current circuits (Private conversation with Dr J Lees, Leicester University and Dr A Barnett, University of Sussex) operate without an R8 and use instead the gate – source junction to reset the integrator and they report a much better noise performance than the traditional circuit. In the absence of R8 and of detector dark current, the drain gate leakage current in J1 will forward bias its gate source junction just sufficiently to conduct that leakage current to the source. The forward bias required to support this leakage current conduction varies from FET to FET but is typically around 100 mV. Figure 5.3 shows the 2N4416 FET characteristics and they are clearly well behaved with a positive gate-to-source voltage.

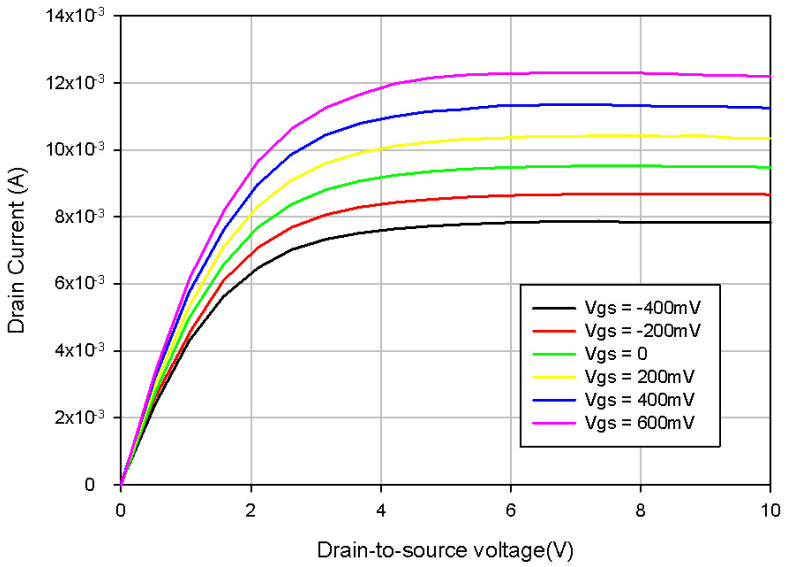

Figure 5.3: Drain current vs drain-to-source voltage as a function of gate-to-source voltage for the 2N4416 JFET

In the conventional circuit shown in Figure 5.2, R8 provides dc feedback and stabilizes the circuit working conditions against the effects of temperature change. If R8 is omitted from this high gain circuit it is virtually impossible to find component values that will ensure

proper working conditions over normal operating temperature ranges. In effect, working without R8 is equivalent to trying to operate a medium gain opamp with no dc feedback. The 2N4416 FET was chosen due to its modest g_m of 4 to 5 mA/V. The BF862 FET was also considered due to its low noise parameters but its rather large g_m of 25 – 30 mA/V makes it prone to saturate the output in a DC feedback-less circuit. The input capacitance of the BF862 is also larger than for the 2N4416 which leads to a higher parallel noise contribution.

This problem was recognised in the first published description of a CSP with no resistive feedback [57]. The solution proposed in [57] was to introduce a frequency dependent feedback loop into the circuit so that the dc gain was low and the ac gain over the frequency range of interest was high.

A similar approach as that used in [57] has been used in the design described here but the frequency dependence has been achieved in a different way such that the output DC operating voltage of the circuit is close to zero; meaning that minimal baseline restoration is required on the output signal.

5.3 Resistor-less CSP circuit with internal frequency dependent feedback.

The circuit used for the measurements described in this thesis is shown in Figure 5.4. The SPICE schematic used to simulate the circuit is presented in Appendix 10.5.

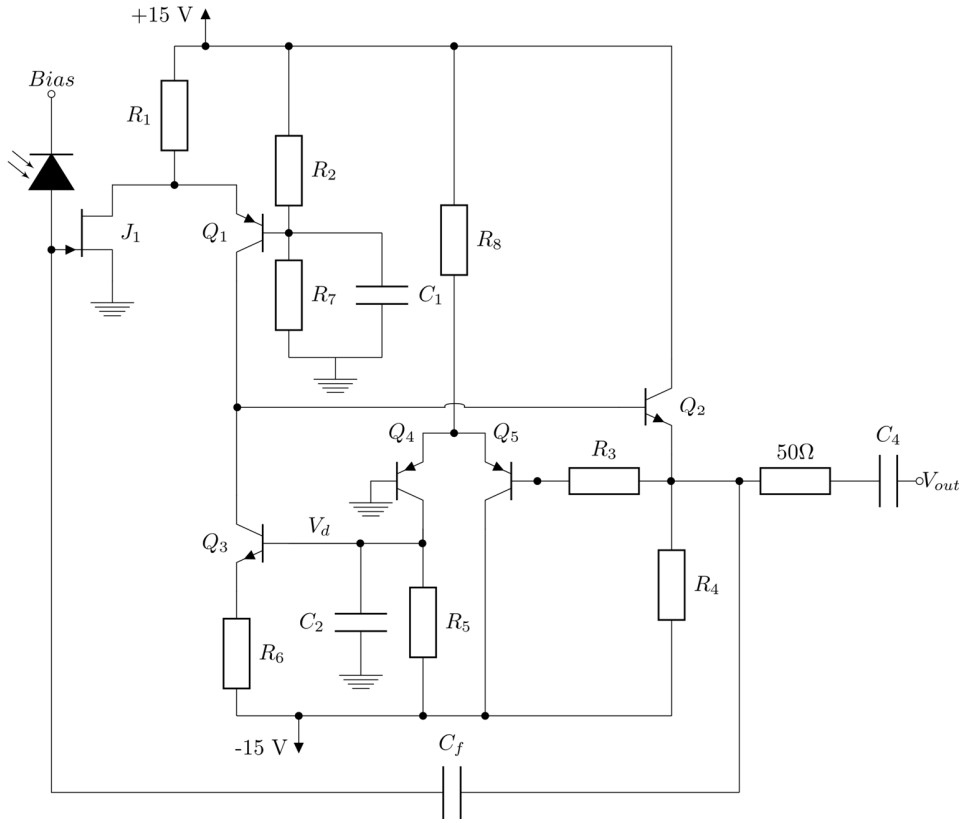

Figure 5.4: Resistor-less CSP circuit

The circuit is the same as that of Figure 5.2 with the exception that R_3 and R_5 in Figure 5.2 have been replaced by R_3, Q_4, Q_5 and R_5 in Figure 5.4. The idea of the internal feedback loop is that the "constant" current source realized by Q_3 is adjusted automatically in such a way as to maintain the output, the voltage at the emitter of Q_2, at a value close to zero. C_2 prevents this feedback process from working at high frequencies.

Transistor Q_4 and Q_5 form a single ended differential circuit, with the base of Q_5

connected to the output of the CSP. The voltage on the collector of Q_4 controls the bias voltage of the current source made of Q_3.

The sum of the collector currents of Q_4 and Q_5 is set by resistor R_8 and is given by:

$$I_{C_{Q4}} + I_{C_{Q5}} = \frac{(15 - V_{be})}{R_8} \tag{5.1}$$

The voltage onto the base of Q_3, V_d, is given by:

$$V_d = -15 + I_{Q4} R_5 \tag{5.2}$$

An increased in the voltage at the base of Q_5 will cause a reduction in the collector current through Q_5, let's say of ΔI_{Q5} . This will lead to an increase in the collector current through Q_4:

$$i_{C_{Q4}} = I_{C_{Q4}} + \Delta I_{Q5} \tag{5.3}$$

The increased current will lead to an increase in the voltage V_d and a bigger base current flows into Q_3. This causes the collector current through Q_3 to increase and less base current flows into Q_2 which also reduces Q_2's collector current. The reduced current through Q_2 prompt a decrease in the voltage on it's emitter, which is also connected to the base of Q_5. This feedback action tries to ensure that the base voltage of Q_5, which is nearly the same as the output voltage, is the same as that of Q_4, which is 0 V. A similar explanation applies for a reduction in the base voltage of Q_5.

The local feedback reduces the DC gain. The frequency response of the feedback path is shown in Figure 5.6. A pole given by the RC constant of C_2 and R_5 is seen around 40 Hz. This pole appears as a zero in the frequency response of the CSP. The response falls at -20 dB/Dec after the pole. The DC gain at the low frequency is consistent with what one would expect and the pole around 5 MHz is due to the R_3 and the base-to-collector capacitance of Q_5.

A feedback capacitance of 0.21 pF was achieved with a surface mount ceramic 0603-packaged 0.18 pF capacitor sourced from Micross. The capacitor was soldered by hand onto the PCB. The PCB was milled such that there was a gap between the back of the capacitor

and the PCB substrate as illustrated in Figure 5.5. After soldering, the capacitance was measured with an LCR meter.

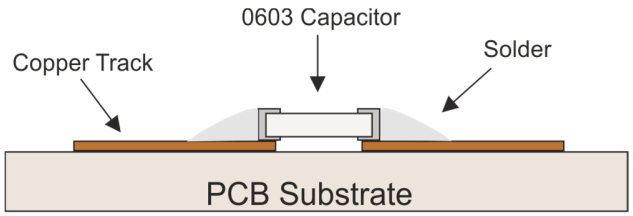

Figure 5.5: Illustration on how the feedback capacitor is mounted

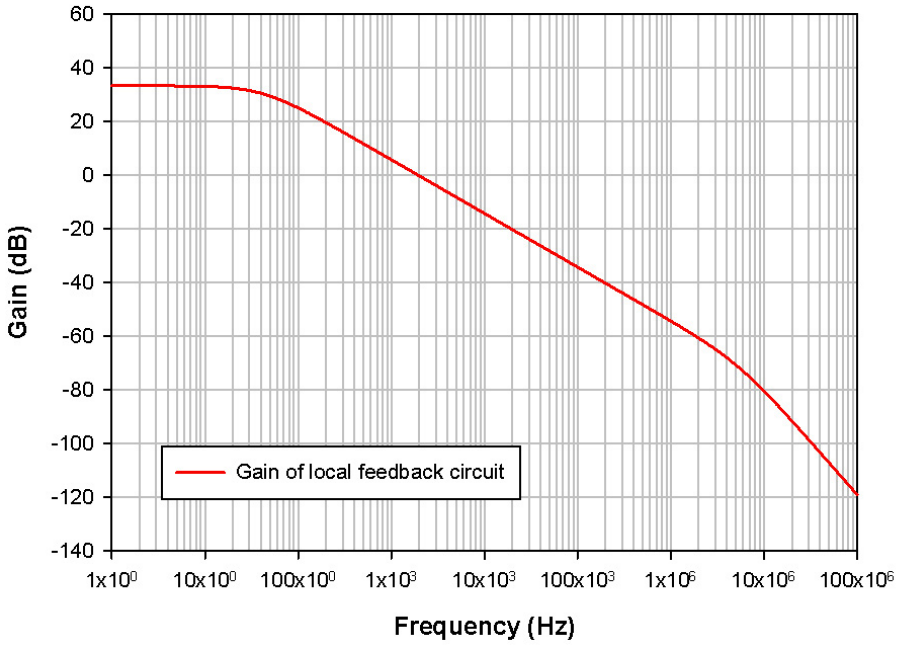

Figure 5.6: SPICE-simulated (red line) frequency response of the local feedback path

5.3.1 Characterisation of CSP

The simulated frequency response of the circuit for several values of dark current is shown in Figure 5.7. The input signal (from a network analyser) is applied via a 0.5 pF capacitor to the amplifier input. The responses exhibit an increasing gain peaking at the lower bandwidth limit as dark current is increased, an effect that was described and explained in [138]. As dark current increases, the incremental resistance of the FET gate decreases and

the input node time constant reduces. The damping can be controlled by C_2. Figure 5.8 shows the response of the circuit with a C_2 value of 10 nF and 100 nF.

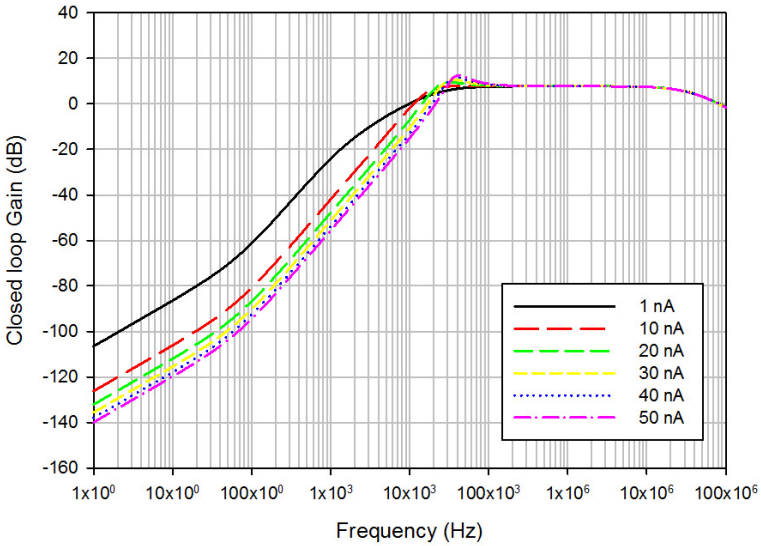

Figure 5.7: Simulated frequency response of the circuit for several values of dark current

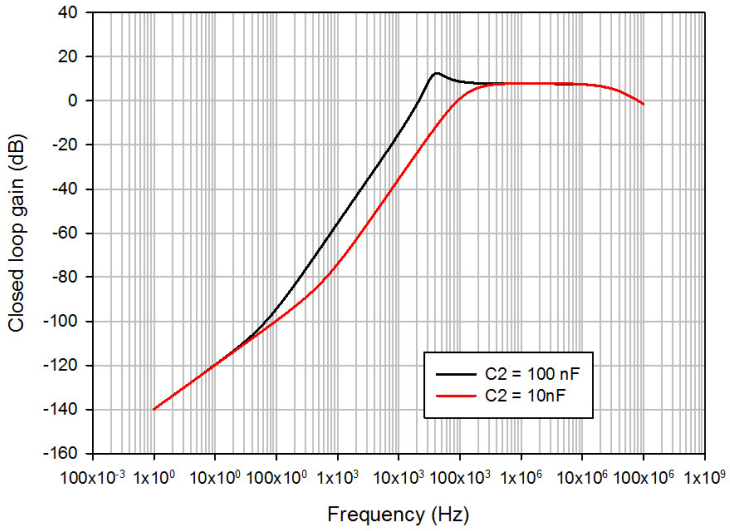

Figure 5.8: Simulated frequency response of the circuit for two values of C2 and dark current of 50 nA

The simulated response to a δ function charge input is shown in Figure 5.9 for various values of dark current. The δ function was generated by applying voltage pulses, ranging from 0 to 0.1 V, to the amplifier input via a 0.5 pF capacitor. A 100 mV pulse amplitude into a 0.5 pF will replicate 312,500 electron-hole pairs. The pulse duration was long compared to the time constants in the circuit. The rise time of the amplifier output is constant at around 14 ns but the shape of the fall shows increasing signs of underdamped behaviour as dark current increases. The reduction in circuit damping as input current increases is clear.

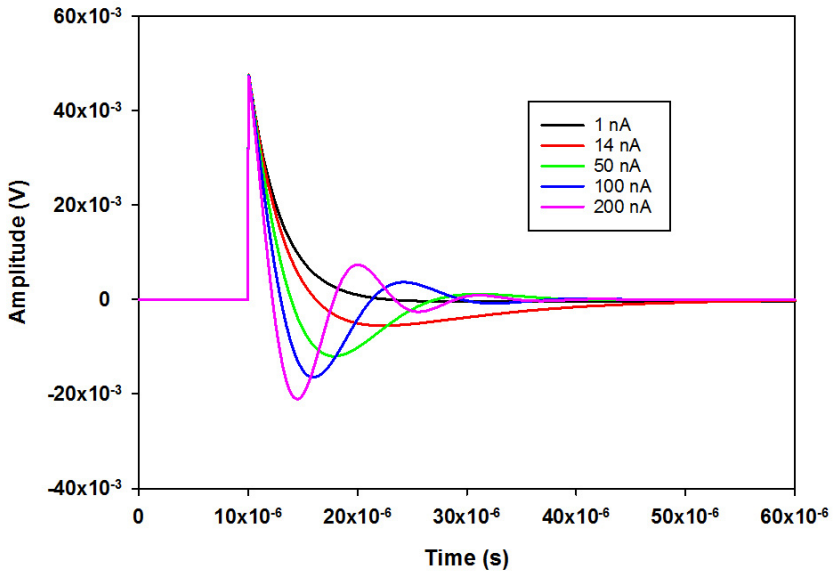

Figure 5.9: SPICE-simulated Transient response of CSP with varying input current

The circuit was built on RogerCorp RO4350B PCB substrate and characterised. RogerCorp substrate was used due to its low dielectric constant and thus minimising the dielectric noise contribution. The transient response was measured with a Si BPX65 connected at the input and biased at 10V with a source-measure unit (SMU). Pulses of 100 ns durations from a generator with a 50 Ω impedance and a 5 ns rise time were injected via a 0.5 pF capacitor also connected to the input. In order to determine the CSP behaviour with respect to dark current, an LED with varying power was shone on the BPX65 in order to provide DC current into the input of the CSP. The photocurrent of the BPX65 was

monitored with the SMU. Figure 5.10 shows the transient response of the CSP for “dark” current ranging from 14 nA to 2 uA. As dark current increases, the output of the CSP showed increasingly underdamped behaviour, as observed in the SPICE simulations. However, the underdamped behaviour is not as severe as that observed in SPICE simulations. The fall rate of the transient increases with increased dark current. This suggests a change in time constant of the circuit with increasing dark current. As dark current flowing into the gate of the input JFET increases, which would cause the incremental gate source resistance to fall. A fall of two orders of magnitude would be expected for an I_G change from 20 nA to 2 µA. The increase in gate source voltage caused by the increase in gate current also causes an increase in gate source capacitance. These two dependencies have opposing effects on the input time constant so the time constant reduction due to increases in dark current is smaller than would be expected by considering gate source resistance changes alone.

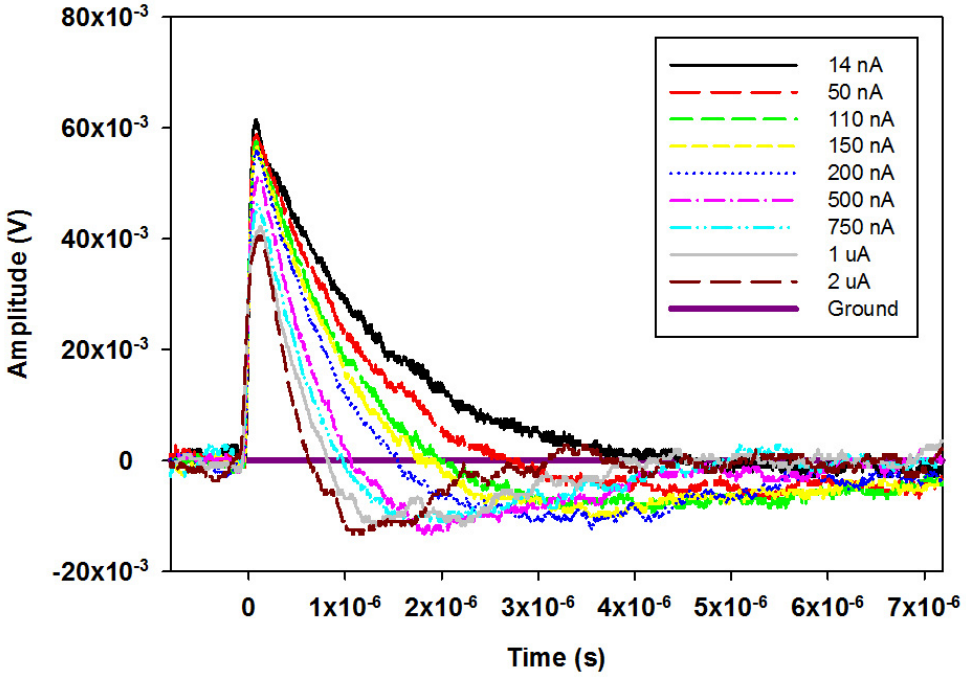

Figure 5.10: Transient response of CSP with varying input current

The frequency response of the CSP was also measured with the same range of “dark” current and is presented in Figure 5.11. Full sized version of the responses are presented in appendix10.6.

The measured responses show only slight peaking with increasing dark current. The distinct peaking seen in the simulation responses are not observed in the measured responses. One reason for the differences between the SPICE and measured results may be that the manufacturer’s JFET SPICE model used do not appear to model accurately the behaviour of gate-source capacitance in the region 0 V < V_{GS} < 0.7 V – a region not used in most applications.

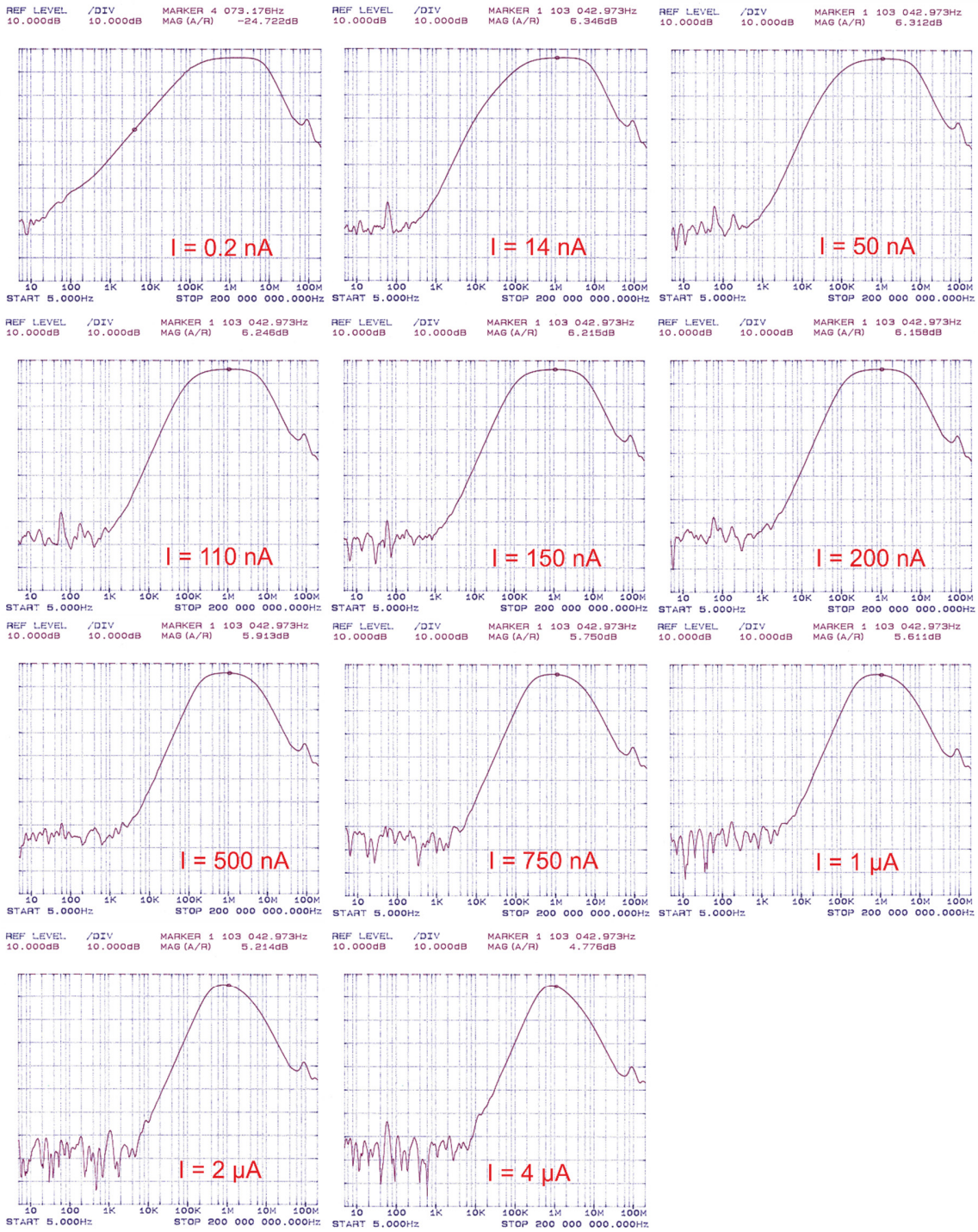

Figure 5.11: Frequency response of circuit with varying detector dark current

To investigate the relationship between forward gate-source voltage and input capacitance, an LCR with an oscillator voltage of 3.1 mV was used to measure the input

capacitance between the gate and the source. The JFET's drain was left open-ended during the measurement. The results, shown in Figure 5.12, indicate that capacitance increases rapidly as the gate-to-source voltage approached 0.7 V.

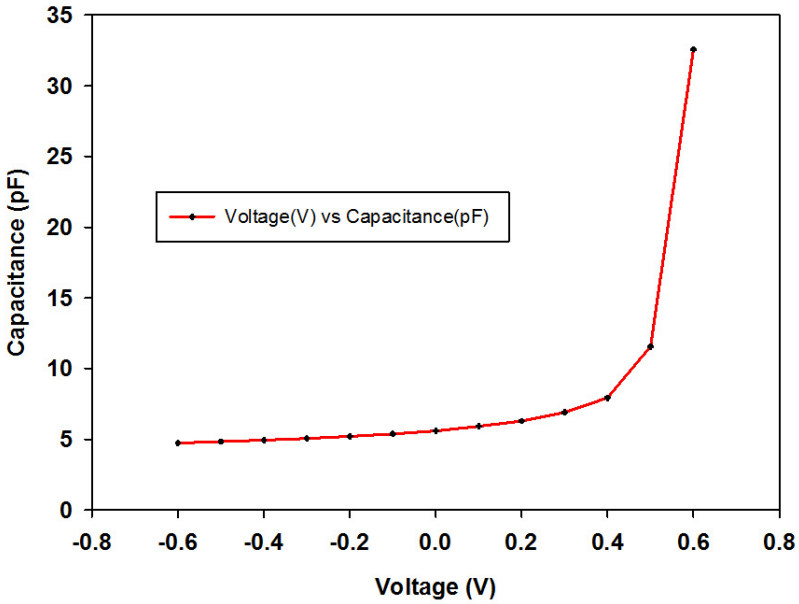

Figure 5.12: Input Capacitance of 2N4416 FET vs Gate-to-Source Voltage

To investigate if this behaviour is modelled by the 2N4416 SPICE model parameter, the gate-source junction was simulated as part of a resonant circuit in SPICE as shown in Figure 5.13. Voltage source V1 is a dc variable power supply that sets the voltage on the gate of the FET, V2 is a signal source. An open drain measurement was desired and to keep SPICE happy, a 1 GΩ was connected between the drain and ground. A frequency .AC sweep was perform in SPICE to determine the resonant frequency for different values of voltages on the gate.

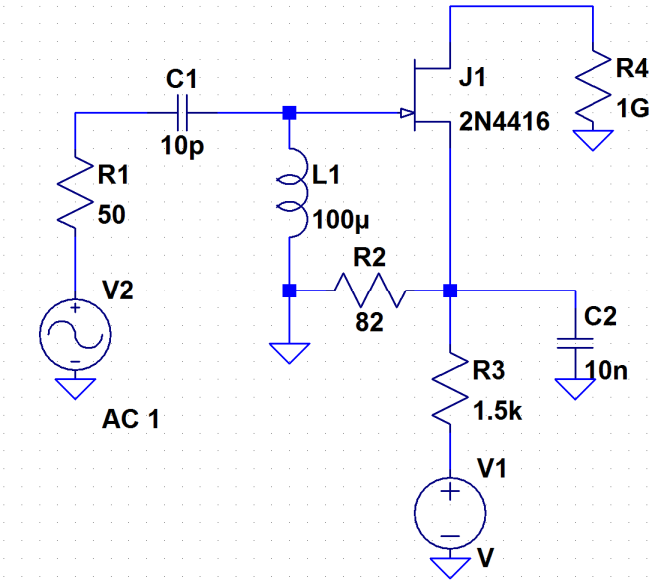

Figure 5.13: Circuit to aid the measurement of FET input capacitance in SPICE

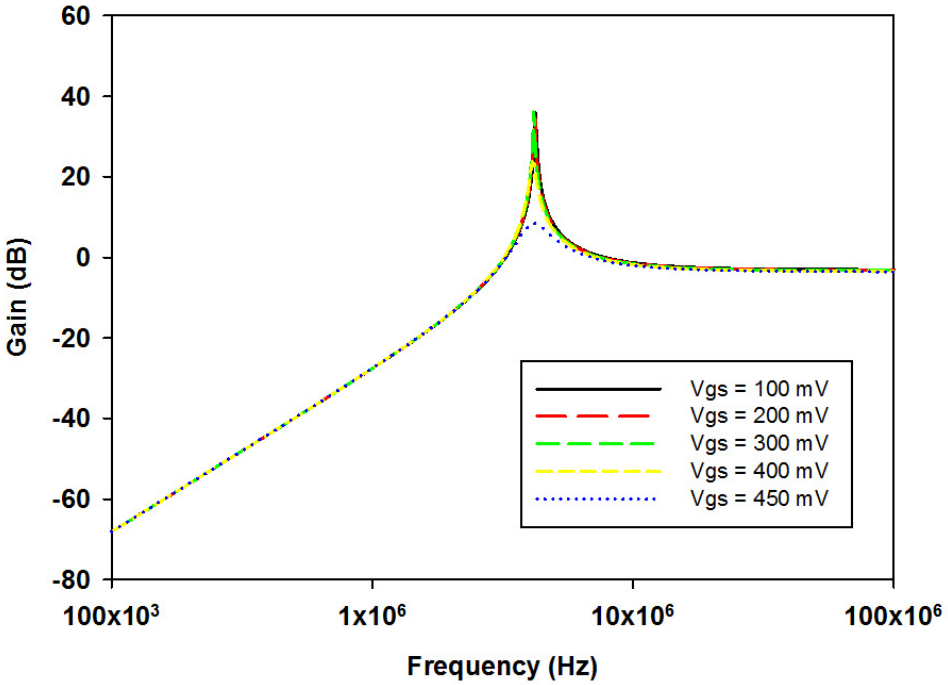

Figure 5.14: Frequency responses of test circuit in SPICE with varying Gate-to-Source Voltage

The virtually constant resosnant frequency in Figure 5.14 indicates that the positive V_{GS} JFET

input capacitance voltage dependence is not modelled accurately by the 2N4416 SPICE model as it implies that the change in the gate-source capacitance with varying positive gate-to-source voltage is virtually non-existent. The initial experimental evidence of Figure 5.12 and Figure 5.14 casts doubts on the reliability of a constant C_{GS} in the forward V_{GS} region.

The circuit shown in Figure 5.13 was modified as shown in Figure 5.15 so that measurements could be made on a real FET. A JFET from InterFET and packaged in a TO-can was used for this experiment. The drain was fed directly by V_3. As in Figure 5.13, the aim was to measure capacitance by resonating CGS with a known inductance. The gate current was controlled by V_1 and R_1 and V_2 was the signal source. The case of the FET was connected to the source. The results are presented in Table 5-1.

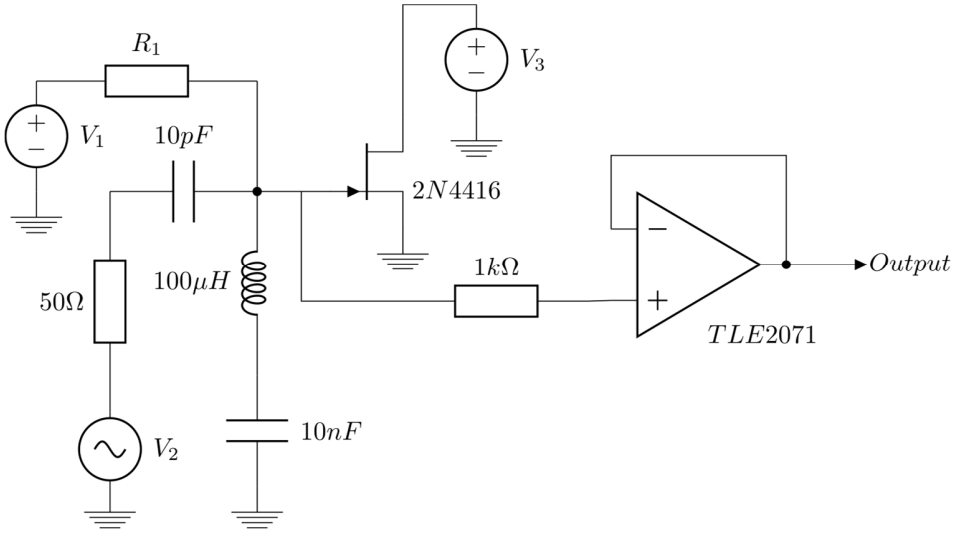

Figure 5.15: Circuit used for the measurement of FET input capacitance

	V_{DS} = 3.3 V				V_{DS} = 0 V		
V_{GS} V	I_G µA	f_r MHz	C_T pF	$C_{GS\ est}$ pF	f_r MHz	C_T pF	$C_{GS\ est}$ pF
0	0	3.312	23.1	4	3.24	24.1	5
+ 0.52	0.1	3.040	27.4	8.3			
+ 0.55	0.2	2.900	30.1	11.0	2.62	36.9	17.8
+ 0.58	0.5	2.570	38.4	19.3			
+ 0.60	1	2.250	50.0	30.9	1.97	65.3	46.2
+ 0.625	2	1.880	71.7	52.6			
+ 0.65	5	1.430	124	105			
+ 0.66	10	1.110	205	186			
+ 0.68	20	0.860	342	323			

Table 5-1: Experimental results from the circuit of Figure 5.15

Being able to measure the capacitance behaviour for positive gate-to-source voltages precisely helps in understanding and improving the noise performance of charge sensitive preamplifiers. This will also help to identify parameters that will model this behaviour in SPICE. However, this is not part of the scope of this work and provides a foundation for future work.

5.4 Noise Performance of CSP

The noise of the CSP was assessed according to the steps provided in section 0 with no detector connected to the input. The shaping time of the shaping amplifier was varied from 0.5 µs to 10 µs. The results are shown in Figure 5.16.

The noise performance of a commercial CSP, the CoolFET from Amptek, was also assessed using the same method and equipment, and is presented in Figure 5.17. The minimum

electronic noise charge (ENC) of 46 electrons RMS was obtained with a shaping time of 6 µs for the CSP designed in this work. The commercial CoolFet CSP showed an ENC of 123 electrons RMS at 2 µs.

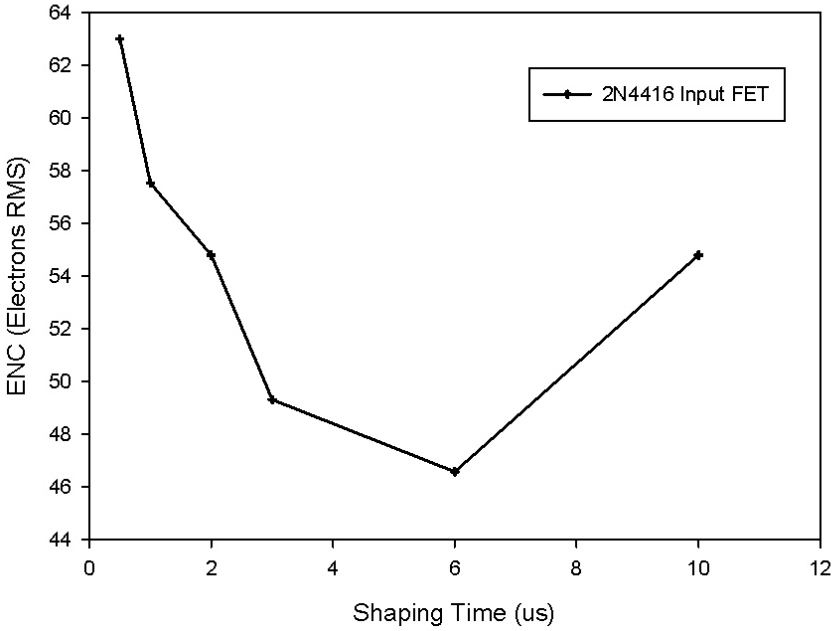

Figure 5.16: ENC vs Shaping Time for CSP

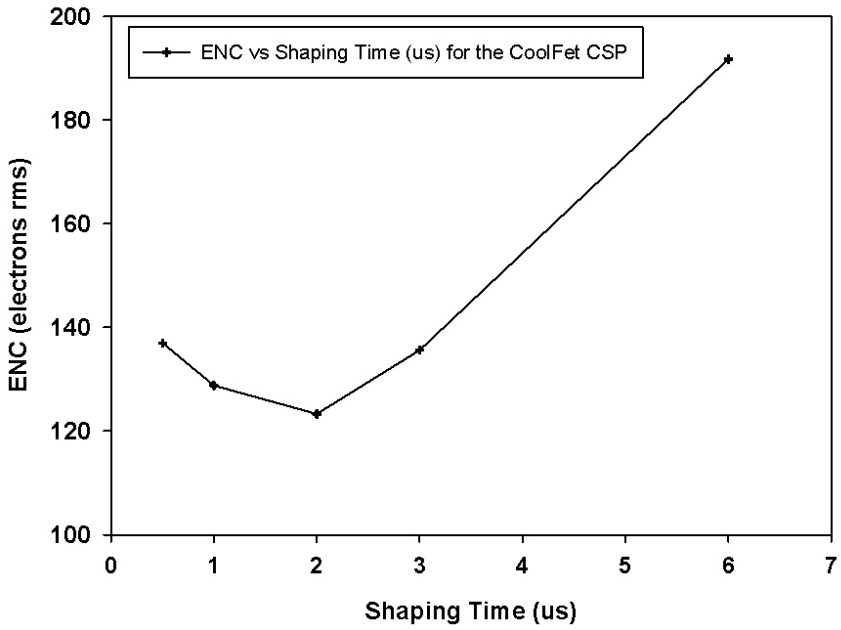

Figure 5.17: ENC vs Shaping Time for CoolFet CSP

5.5 Voltage Gain of CSP

For charge sensitive preamplifiers, one of the most important factors, apart from noise, is the charge gain. For a well-designed CSP with a large voltage gain, the charge gain is solely dependent on the feedback capacitor and can be controlled with good precision.

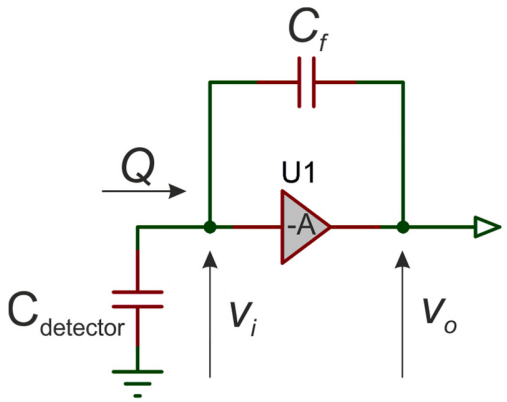

Figure 5.18: CSP Circuit

Consider Figure 5.18:

The voltage gain is given by:

$$\frac{dv_o}{dv_i} = -A \tag{5.4}$$

such that $v_o = -Av_i$

The charge deposited on the feedback capacitor C_f is given by:

$$Q_f = C_f v_f \tag{5.5}$$

where $v_f = (A+1)v_i$

With an input impedance $Z_i = \infty$, the input charge Q is equal to the charge Q_f on the feedback capacitor. This gives an effective input capacitance of:

$$C_{i\_effective} = \frac{Q}{v_i} = C_f(A+1) \tag{5.6}$$

This effective capacitance is dynamic as it is dependent on A. The charge gain of the CSP can then be represented as:

$$Charge\ Gain = \frac{dV_o}{dQ} = \frac{Av_i}{C_{i\_effective}\, v_i} = \frac{A}{C_{i\_effective}} = \frac{A}{A+1}\frac{1}{C_f} \tag{5.7}$$

If the voltage gain A of the CSP is large ($A >> 1$), the charge gain reduces to:

$$Charge\ Gain \approx \frac{1}{C_f} \tag{5.8}$$

It is highly desirable to be able to precisely control the charge gain of a CSP, and this is possible if the voltage gain is large. To evaluate the voltage gain on the CSP presented in this work, the following setup shown in Figure 5.19 was used.

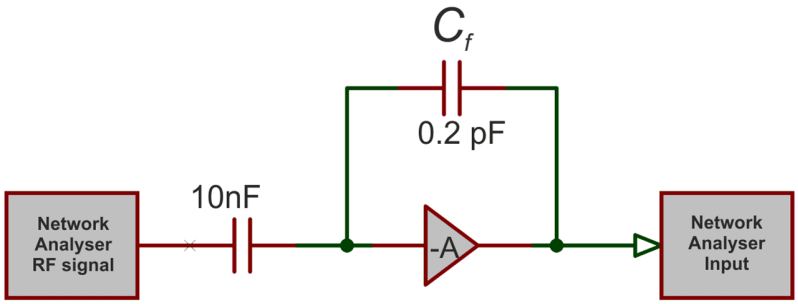

Figure 5.19: Setup for measuring Voltage Gain of CSP

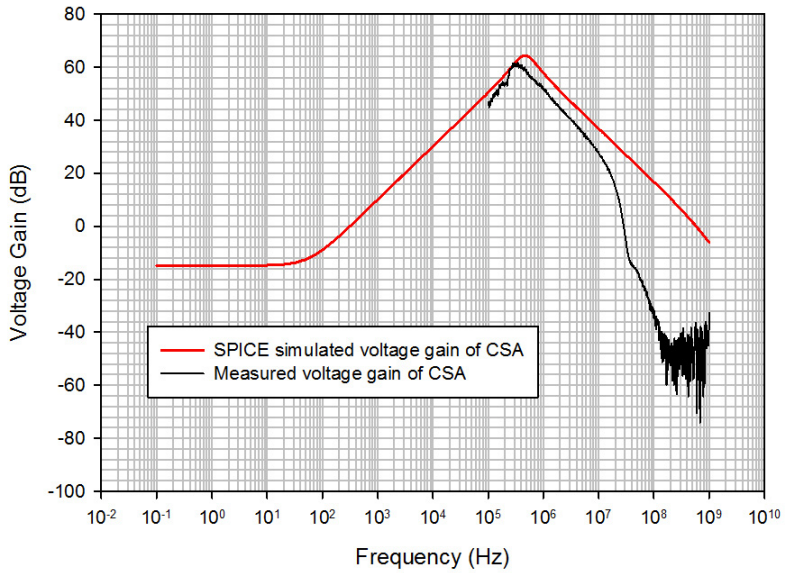

Figure 5.20: SPICE simulated (red line) and measured (black line) voltage gain of CSP

Figure 5.20 shows the simulated and measured voltage gain of the CSP. A 50 Ω matched network analyser capable of measuring between 100 kHz and 1 GHz was used. The measured voltage gain confirmed a peak gain of 60 dB or 1000 V/V in linear terms at around 2 MHz.

5.5.1 Analysis of CSP voltage gain

Considering the CSP circuit presented Figure 5.4, approximately $1\ mA$ flows through *Q1* and *Q3*. The early voltage of *Q3* is ≈ 120 and ≈ 40 for *Q1*; making their output resistances equal to $3M\Omega$ and $600k\Omega$ respectively. The input resistance of *Q2* is about $500k\Omega$, ignoring the negligible contribution of *Q2*'s r_{be}. The three resistances given above are effectively in parallel and the voltage gain is given by $g_m(J1) \times$ $the\ parallel\ combination\ of\ the\ three\ resistance$. With a typical g_m of $4.5mS$ for the 2N4416 JFET, the open loop gain can be found to be 1125, which correspond to 61 dB. This is in agreement with the SPICE and measured voltage gain. The transconductance of $4.5mS$ is the value specified by the manufacturer with the JFET operated in a reverse biased gate-to-source junction. In the case presented in this thesis where the gate-to-

source junction is forward biased, the transconductance of the JFET will be higher.

However, although the voltage gain of CSP is large enough such that the charge gain is dependant on the feedback capacitor C_f, but it may still impact on the charge transfer from the detector to the CSP. The effective CSP input capacitance is the capacitance seen at the point where the detector is connected. Any charge inject at the input of the CSP will be divided between the CSP's effective input capacitance and the detector capacitance. A higher effective CSP input capacitance compared to the detector capacitance means that more charge will end up across the feedback capacitor.
The fraction of signal charge is given by the following:

$$\frac{Q}{Q_t} = \frac{C_{i\_effective}\, v_i}{Q_{detector}+Q} = \frac{C_{i\_effective}}{Q_t} \cdot \frac{Q_t}{C_{i\_effective}+C_{detector}} = \frac{1}{1+\frac{C_{detector}}{C_{i\_effective}}} \qquad (5.9)$$

With a CSP voltage gain *A* of 1000, the effective input capacitance is 0.2 nF. Considering a detector of capacitance of 6 pF, the effective charge transfer fraction into the preamplifier is 0.97; meaning that 3% of the charge remains on the detector. It is of course ideal for most of the charge to be transferred into the the preamplifier to maximise the signal-to-noise ratio, especially for low energy detection.

With a JFET g_m of ten times the g_m of the 2N4416, the charge transfer can be increased to 0.997. The BF862 JFET, which was discounted at the start of this work due to its relatively high capacitance, has the ability to provide a higher voltage gain due to its large g_m of 45 *mS.*

The CSP circuit was built with the BF862 JFET and a value of 600 Ω for R1. Figure 5.21, which shows the simulation voltage gain, confirms a gain of 10 times higher than the CSP with the 2N4416 JFET, i.e a voltage gain of 80 dB (10000 V/V).

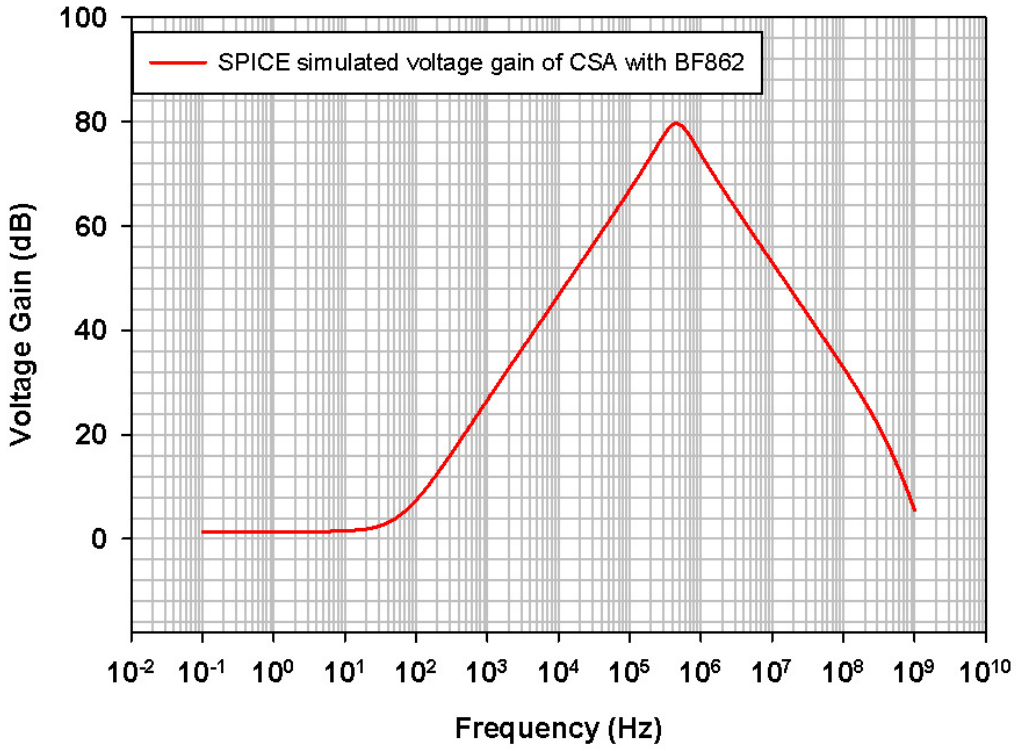

Figure 5.21: SPICE simulated (red line) voltage gain of CSP with BF862 JFET

The CSP with BF862 was characterised for its noise performance and is presented in Figure 5.23. The CSP with the BF862 shows higher noise values than the CSP with the 2N4416. The higher noise could be attributed to the higher input capacitance of the BF862, leading to higher series white noise; but since the g_m of the BF862 is much higher than the 2N4416, the series white are comparable. In fact, the higher noise is due to the parallel white noise; with the BF862 having a larger gate leakage current compared to the 2N4416.

The gate-to-source capacitance versus gate-to-source voltage for the BF862 is shown in Figure 5.22 and Table 5-2 compares the noise contributions of the 2N4416 and the BF862 JFET. It is important to point out that the values of transconductance, $g_{m,}$ specified in Table 5-2 were not obtained experimentally and are from the manufacturers' datasheet.

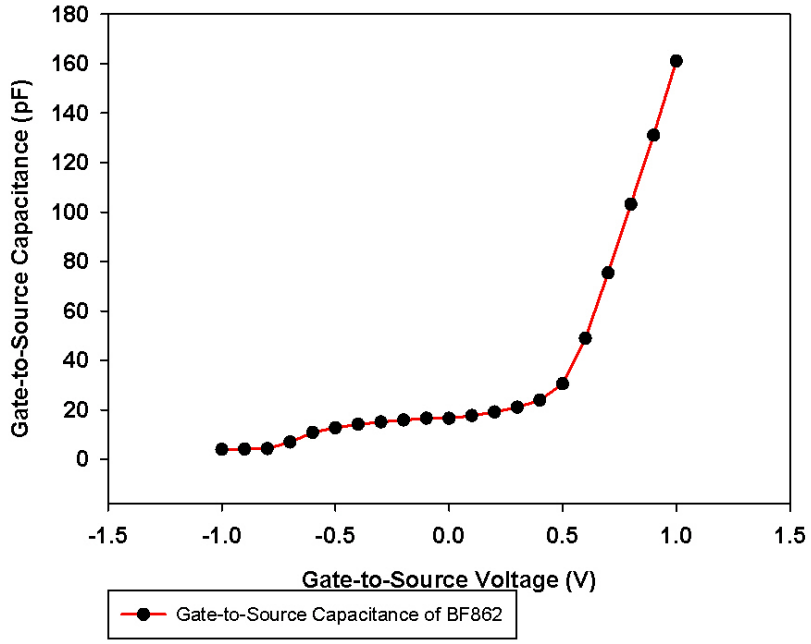

Figure 5.22: Gate-to-source capacitance versus gate-to-source voltage for the BF862

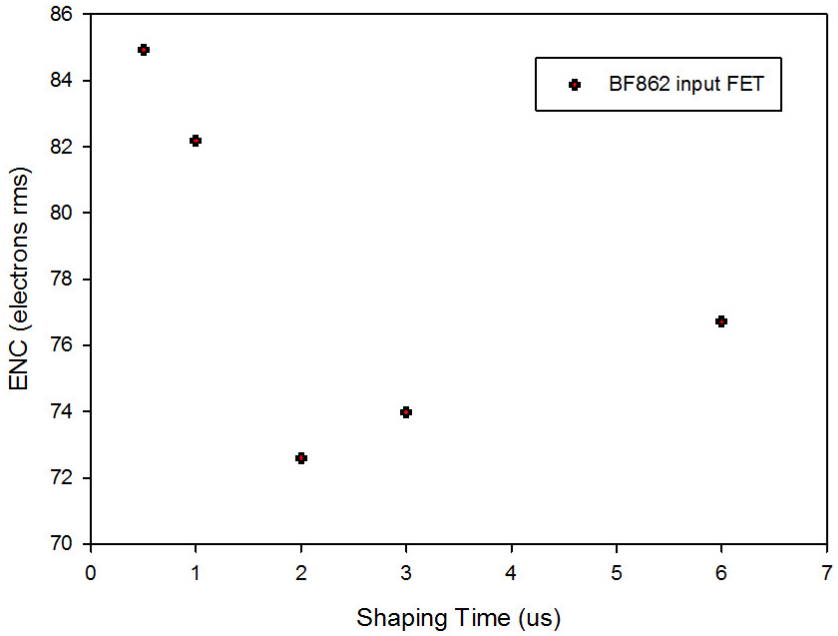

Figure 5.23: ENC vs Shaping Time for CSP with BF862 JFET

Shaping Time = 2 µs	g_m (mS)	Capacitance (pF)	Gate Current (pA)	Series noise (e^- r.m.s)	Parallel Noise (e^- r.m.s)
2N4416	4.5	5	2	20	8
BF862	45	18	20	23	25

Table 5-2: Comparison of noise contributions due to BF862 and 2N4416

5.6 Conclusion

A resistor-less low noise charge sensitive preamplifier was designed with a local feedback topology. The CSP achieved better noise performance than commercially available CSP such as the CoolFET. Although the CSP did not achieve noise performance as low as the best published circuit [57], this work provided the groundwork in building the electronics suitable to characterise Sheffield-grown detectors. Lower noise performance can be achieved by using better layout techniques such as utilizing a JFET on die like Bertuccio[57] used in his work.

The CSP frequency responses were measured with increased input current and results showed that the CSP was well-behaved for current up to 4 µA. Discrepancies between SPICE simulated results and measured results were addressed by analysing the input capacitance behaviour of the circuit.

Preliminary measurements suggest that the SPICE models supplied by the manufacturers of the JFET devices used do not model C_{GS} accurately in the forward bias V_{GS} region. The increased CGS for larger leakage currents will degrade the CSP noise performance and this degradation has been noticed by other workers in the field but has not been reported or explained.

Further experimental work is needed to quantify accurately the real C-V behaviour in this region.

The following chapter presents soft X-ray spectroscopy measurements carried out with novel Sheffield-grown AlInP APDs and the CSP discussed in this chapter.

Chapter 6 $Al_{0.52}In_{0.48}P$ APD for soft X-ray spectroscopy

The previous chapter presented a low noise CSP with a novel local feedback topology and the performance of the CSP is assessed with novel $Al_{0.52}In_{0.48}P$ APD for soft X-ray spectroscopy in this chapter.

6.1 Introduction

Detectors without cryogenic cooling are desired in all application due to operational cost. Wide band gap compound semiconductors meet this criteria and can also tolerate harsh environment, particularly high temperature and radiation in some cases. Wide band gap compound semiconductors such as GaAs, SiC and AlGaAs have been investigated for room temperature X-ray detection and comprehensive reviews can be found in [139, 140]. Bertuccio et al. have reported SiC X-ray detectors with sub-keV energy resolution operating in a wide temperature range [141] and some of the best results were achieved with ultra-low noise electronics. SiC detectors with a pulser peak FWHM of 315 eV were demonstrated [141], which were later improved to 113 eV [142]. An energy FWHM of 196 eV at 5.9 keV was also presented.

Most of the III-V X-ray research detectors reported in literature are based on GaAs [51, 104, 105]. GaAs offers lower leakage current than Ge for instance while providing a better absorption coefficient compared to Si. An energy resolution of 530 eV at energy peak of 5.9 keV was reported by Yatsu *et. al* for a Si reach-through Avalanche photodiode at room temperature [91].

For wide bandgap semiconductors the total charge created for each absorbed photon can be low, making it challenging to measure. Ultra-low noise electronics, usually a charge sensitive preamplifier, can be used to integrate, amplify and convert the total created charge into a voltage signal. Detecting X-ray less than 10 keV can still be challenging even with low noise electronics as it can be difficult to resolve all the different detected energies or often the detected energies peaks are too close to the noise floor to be resolved. In addition to using low noise electronics, the internal gain of an Avalanche photodiode

(APD) can be used to detect and to resolve the different energy peaks for low energy X-rays as the internal gain increases the amount of charge created for each absorbed X-ray photon. The gain from an APD is the end result of successive impact ionization process whereby an energetic electron (or a hole) gives up its energy to create another electron and a hole. The combination of an APD and low noise electronics can, in these cases, provide the gain and the noise performance desired to amplify and pull the detected energies away from the noise floor, thus improving the signal-to-noise ratio. However, this does not necessarily improve the energy FWHM as was pointed out by Tan *et. al* [143]. Tan *et. al* concluded that a material with a small ratio of ionization coefficients is required to achieve a small energy FWHM for low energy X-ray photons (when the number of electron-hole pair is small).

Gomes et al. have reported a GaAs/AlGaAs Separate Absorption and Multiplication region Avalanche Photodiode (SAM-APD) with a resolution of 1.08 keV when exposed to $^{55}\mathrm{Fe}$ source [51]. The effect of the avalanche gain improved the energy resolution.

This chapter presents results of the first soft X-ray spectroscopy measurements performed on novel $Al_{0.52}In_{0.48}P$ APD.

$\mathrm{Al_{0.52}In_{0.48}P}$ is the widest band material that can be grown lattice-matched on a GaAs substrate. Due to its wide bandgap, AlInP can offer reverse dark current of less than $2\,\mathrm{pA}$ at gain of 100 for a $200\mu\mathrm{m}$ device, making it desirable for room temperature operation [144]. This dark current is limited by surface leakage. In this work, we report a $\mathrm{p^+ - i - p^- - n^+}$ AlInP APD coupled to the CSPs presented in Chapter 5 and their characterisation for soft X-ray detection at room temperature. The effects of avalanche gain on the energy resolution of the detected X-ray peak and the noise of the system were experimentally obtained at room temperature.

6.2 APD Details

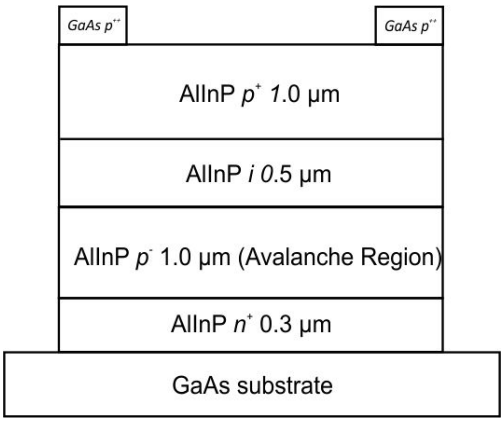

Figure 6.1: Details of the AlInP APD wafer

The APDs used in this work were fabricated from a wafer which, whilst was intended to be a $\mathrm{p^+ - i - p - i - n^+}$ structure, actually transpired to have a non-uniform $\mathrm{p^-}$ doping in the 4th layer. This resulted in the structure shown in Figure 6.1. The wafer was grown lattice-matched on a GaAs substrate by Metal Organic Vapour Phase Epitaxy. A highly doped thin 50 nm GaAs cap was grown on the top of the p^+ AlInP cladding to ensure good ohmic contact. Standard photolithography process and chemical wet-etching were used to fabricate circular mesa diodes with diameters ranging from 50 to $400\mu m$. To ensure the incident X-ray photons are fully injected from the top AlInP p^+ cladding layer only, These devices were initially made for optical applications and to ensure that the incident optical photons are fully injected from the top AlInP p^+ cladding layer only, the GaAs cap was etched off, with mesa walls being passivated by SU-8 photoresist. Au/Zn/Au annular contacts were deposited on the top GaAs p^+ layer of the diode to form ohmic p^+ contact and the n^+ contacts were formed by using In/Ge/Au on the substrate. The fabricated APDs are shown in Figure 6.2. A photograph of one of the measured APDs is shown in Figure 6.3. The SU-8 that is visible on the photograph will lead to an increase in dielectric capacitance which will increase the dielectric noise contribution to the total ENC.

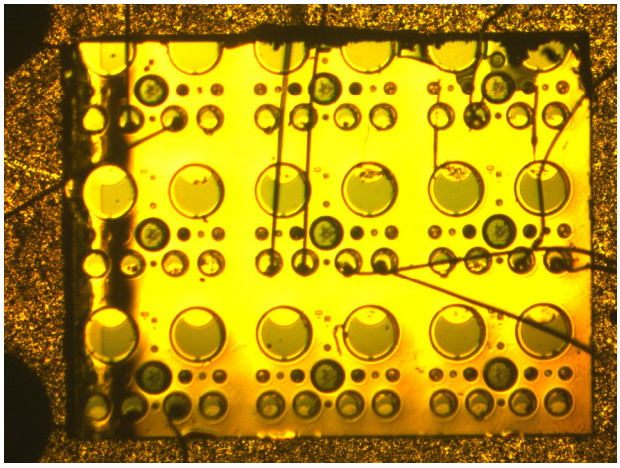

Figure 6.2: Photograph of the fabricated APDs

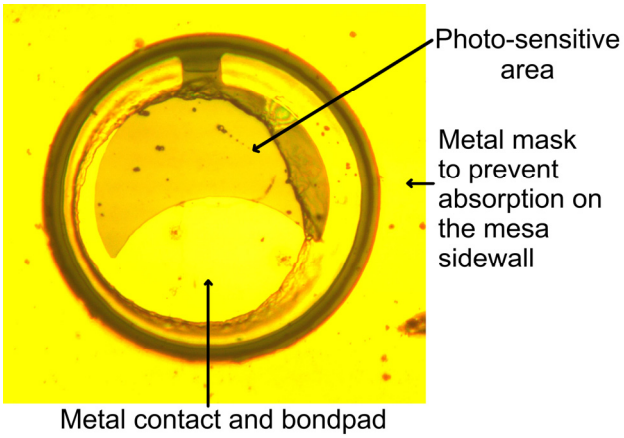

Figure 6.3: Photograph of one of the measured APDs

Capacitance-Voltage (C-V) measurements were performed on two of the $200\mu\mathrm{m}$ diameter devices, and these are shown in Figure 6.4. The minimum voltage required to fully deplete the APD (punch-through voltage) is indicated by the sudden decrease in capacitance at $\sim 41\mathrm{V}$ and at $\sim 45\mathrm{V}$ for D1 and D2 respectively. Between 0 and 41 V or 45 V for D2, the depletion region exists in the bottom $n^+ - p^-$ junction only. Information of the doping density and thickness of the avalanche region can therefore be deduced from the slope of $d(1/C^2)/dV$ and the values of C, respectively [112]. Beyond this voltage range, the device 'punches-through' with the depletion reaching the top p^+ contact layer. The final capacitance of $\sim 4\mathrm{pF}$ allows the total depletion width of the i

region and the avalanche region ($1.5\mu m$) to be estimated. The doping density and thickness of the avalanche region were estimated to be $5.4 \times 10^{16} cm^{-3}$ and $1.0\mu\text{m}$ respectively. The thickness and doping density of the *i* region was estimated to be $0.5\mu\text{m}$ and $1.5 \times 10^{15} cm^{-3}$ respectively.

A breakdown voltage of 72 V was obtained in the dark reverse current-voltage (I-V) measurement for diode D1 as illustrated in Figure 6.5. An earlier breakdown of 67 V is observed for D2. The measured dark current is mainly dominated by surface leakage current.

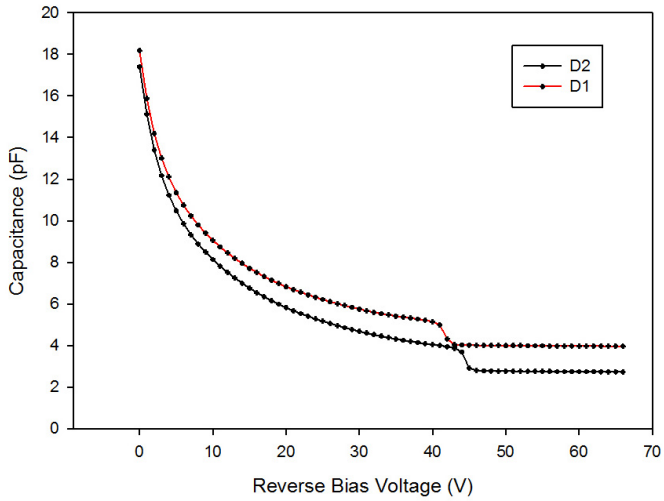

Figure 6.4: Graph of capacitance versus reverse bias data of Diode D1 and D2

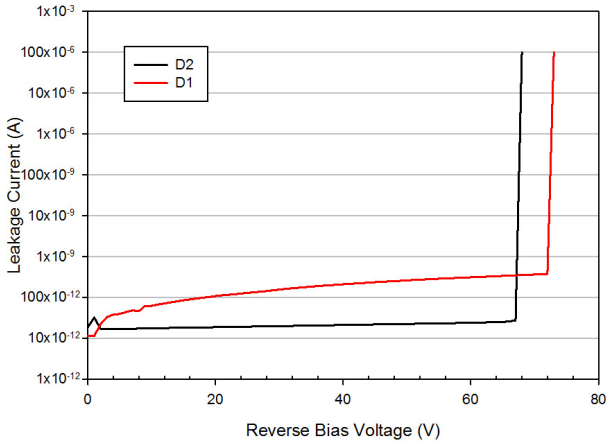

Figure 6.5: Graph of dark current versus reverse bias data of Diode D1 and D2

6.3 X-ray measurements

6.3.1 Experiment and method

To facilitate X-ray measurements, the $200\mu\mathrm{m}$ diameter APDs were packaged into TO-5 headers using a gold wire bonder. The TO-5 headers were housed with, and connected to, the CSPs presented inChapter 5. The CSP was powered by a $\pm 15\mathrm{V}$ linear power supply and its output was connected to an Ortec 570 shaping amplifier (SA). The shaping amplifier also provided some voltage gain to the signal from the CSP. The amplified signal was then digitized with an Ortec EasyMCA-8k multichannel analyzer (MCA) interfaced to a computer yielding pulse height spectra. Shaping times of $0.5\mu s$, $1\mu s$ and $2\mu s$ were used.

The reverse bias for the APD was applied with a Keithley 2400 Source-Measure unit through a biasing resistor of $330M\Omega$ and a high voltage $10nF$ capacitor to ground. A 55 MBq $^{55}\mathrm{Fe}$ radioisotope source with characteristic Mn K_α and K_β peaks at 5.9 and 6.49 keV respectively was placed 1 cm away from the APD. Pulse height spectra for different reverse bias voltages were collected at room temperature. For each set of bias voltage, the spectra was collected for a duration of 60 minutes.

6.3.2 X-ray spectra

Figure 6.6 and Figure 6.7 shows D1 energy spectra for reverse bias voltage ranging from 15 to 45 V and 45 to 69 V, respectively and shaping time of $0.5\mu s$. Figure 6.9 and Figure 6.10 shows D2 energy spectra for reverse bias voltage ranging from 35 to 50 V and 50 to 65 V, respectively.

Increasing the reverse bias voltage causes the 5.9 keV and 6.49 keV peaks to move away from the noise floor and hence improving the signal-to-noise ratio. The shift of the 5.9 keV and 6.4 keV peaks can be observed more easily in Figure 6.8, which plots peak position versus reverse bias voltage for diode D1. The slope of the curve changes gradually with reverse bias voltage, from even the smallest voltage of the data range because of increase in depletion region. For this type of $\mathrm{p}^+ - \mathrm{i} - \mathrm{p}^- - \mathrm{n}^+$ structure, at low bias voltage, it is not possible to determine whether the shift of the energy peak is due to avalanche gain, M, or increase in carrier collection efficiency. The higher number of counts registered at bias voltage of 45V for D1 indicates that the APD is operating around punch-through

(~41V), when the depletion region has widened to include both the $0.5\mu m$ i-layer and the $1\mu m$ avalanche region and this increases the charge collection efficiency. Although the increased reverse bias increases M, it also increases the APD leakage current which can in some cases has a detrimental effect on the noise performance. The area under the peaks increases from 15 V to 45 V as the APD depletes, increasing its active volume. After punch-through, the areas under the peaks shown in Figure 6.7 is expected to stay the same as the total active volume of the APD is the same. However, in reality, the area will change as part of the signals from the CSP is filtered out by the non-linear shaping amplifier.

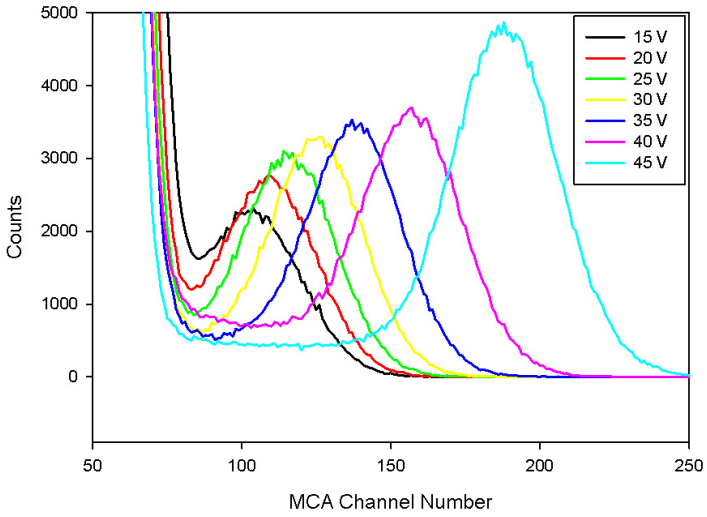

Figure 6.6: Pulse height spectra collected by the diode D1 irradiated with a ^{55}Fe source with shaping time of 0.5μs, Reverse bias of 15 to 45V

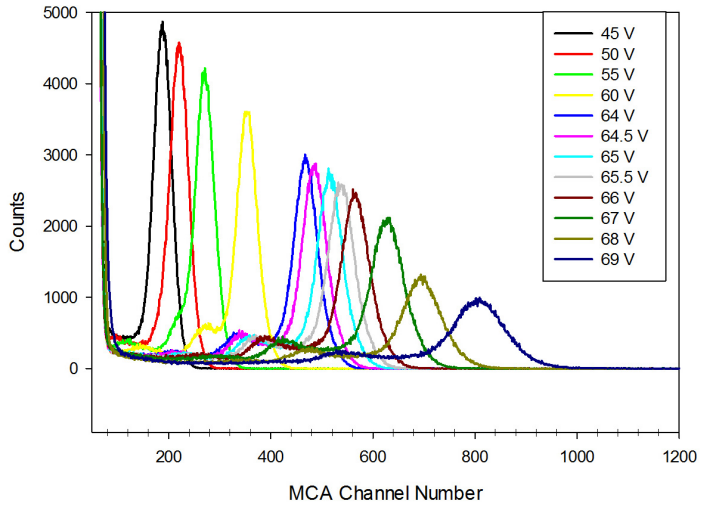

Figure 6.7: Pulse height spectra collected by the diode D1 irradiated with a ^{55}Fe source with shaping time of 0.5µs, Reverse bias of 45 to 69V

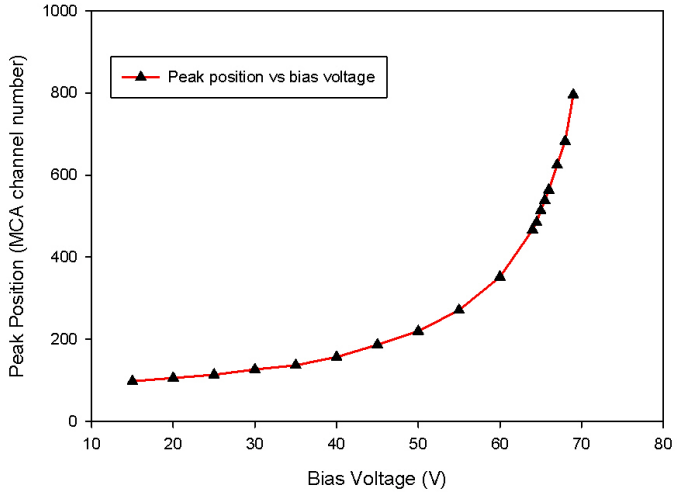

Figure 6.8: Peak position (in MCA channel number) vs Bias voltage for D1

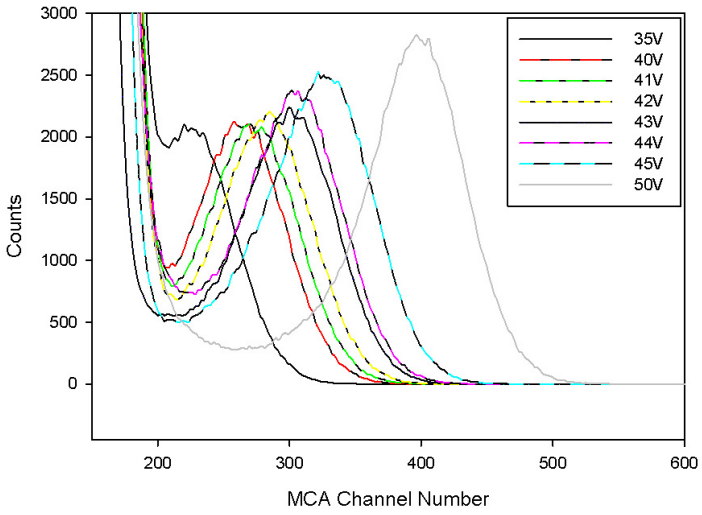

Figure 6.9: Pulse height spectra collected by the diode D2 irradiated with a ^{55}Fe source with shaping time of 0.5µs, Reverse bias of 35 to 50V

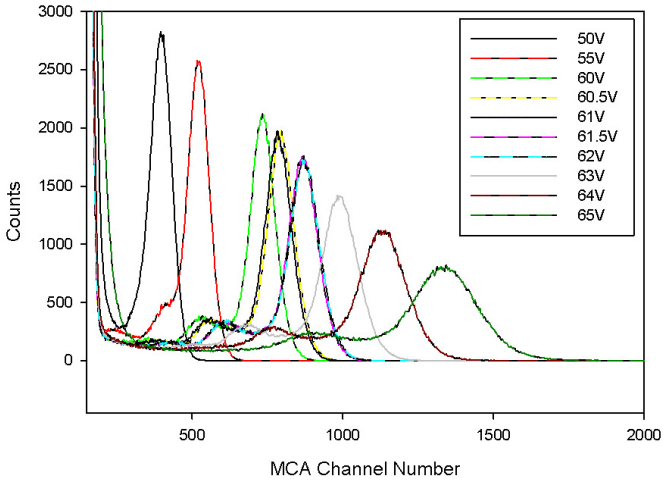

Figure 6.10: Pulse height spectra collected by the diode D2 irradiated with a ^{55}Fe source with shaping time of 0.5µs, Reverse bias of 50 to 65V

The Full Width Half Maximum (FWHM) energy resolution of a semiconductor X-ray APD can be expressed as a semi empirical expression, given by:

$$(FWHM_{total})^2 = \frac{(2.36\varepsilon)^2(f+F-1)E}{\varepsilon} + (FWHM_{EN})^2 \quad (6.10)$$

where *f* is the Fano factor [95], ε is the electron-hole pair creation energy, *E* is the energy of the incident X-ray, *F* is the excess noise factor that characterises the gain fluctuation in the APD and $FWHM_{EN}$ accounts for the noise due to the pre-amplifier, detector's leakage current, capacitance and the signal processing.

The total FWHM is usually degraded by $FWHM_{EN}$ and the effect of gain distribution of the APD if the absorbed photons obey Poissonian statistics (represented by $\frac{(F-1)E}{\varepsilon}$ from equation 6.10). For most modern semiconductor crystals, $\frac{(F-1)E}{\varepsilon}$ is small compared to $FWHM_{EN}$ [94, 145] and when $\frac{(F-1)E}{\varepsilon}$ and $FWHM_{EN}$ are negligible, the spectral resolution is said to be Fano limited. From Figure 6.5, it can be observed that the leakage current of the detector is in the region of 40 pA for D1 before breakdown and this is smaller than other research III-V APDs presented in literature [146-149]. Thus the contribution of the leakage current of the detector to the term $FWHM_{EN}$ is expected to be small.

The electronic noise performance was assessed the method described in section 0 with the detector connected to the input of the CSP and biased. A pulse generator together with a test capacitor C_{test} was used to simulate charges at the input of the CSP. The pulser line was acquired after the MCA was calibrated using the $^{55}\mathrm{Fe}$ 5.9 keV line obtained for a given bias voltage. The FWHM of the peak produced by the pulse generator was measured to determine the noise contribution of the APD and the electronics, excluding the noise contribution due to fluctuation of the charge generated by absorbed photons, Fano noise and charge trapping noise since the APD is not exposed to the $^{55}\mathrm{Fe}$ source under those measurements. The measured pulser line FWHM, which includes contribution from the APD leakage current and capacitance, the CSP, SA and any stray capacitances between the diode and the CSP input, versus bias is presented in Figure 6.11, labelled "Circuit Noise 0.5us".

The FWHM of the combined 5.9 keV and 6.49 keV energy peaks in the collected

spectra, with the APD exposed to the $^{55}\mathrm{Fe}$, is used to quantify the energy resolution of the detector spectroscopy system. The channel number information from raw X-ray spectra was converted into energy by using the 0 eV noise peak and the detected 5.9 keV X-ray peak as references. A Gaussian fitting was then used on the combined 5.9 keV and 6.49 keV peaks in order to determine the FWHM. The counts for the energy peak was normalised to facilitate its Gaussian fitting. Secondary peaks is also observed at that bias and their origin is discussed in the next section. Figure 6.11 also shows the experimental detected energy FWHM at 5.9 keV as a function of reverse bias voltage for the collected spectra for diode D1 with a shaping time of $0.5\mu s$, $1\mu s$, $2\mu s$ and $3\mu s$. The energy FWHM decreases with increasing reverse bias voltage up to 65 V whereby increasing the bias voltage beyond, leads to an increase of leakage current and hence contributes to an increase in the FWHM. The measured pulser line FWHM for a shaping time of $0.5\mu s$ is also presented.

Charge trapping noise can also be present in compound semiconductors and can lead to a non-Gaussian distribution with quasi exponential tails appearing on the low energy side of the spectral lines [150].

The plot of measured FWHM versus bias for diode D2 is presented in Figure 6.12. Table 6-1 summarises the best energy resolution obtained with both diodes.

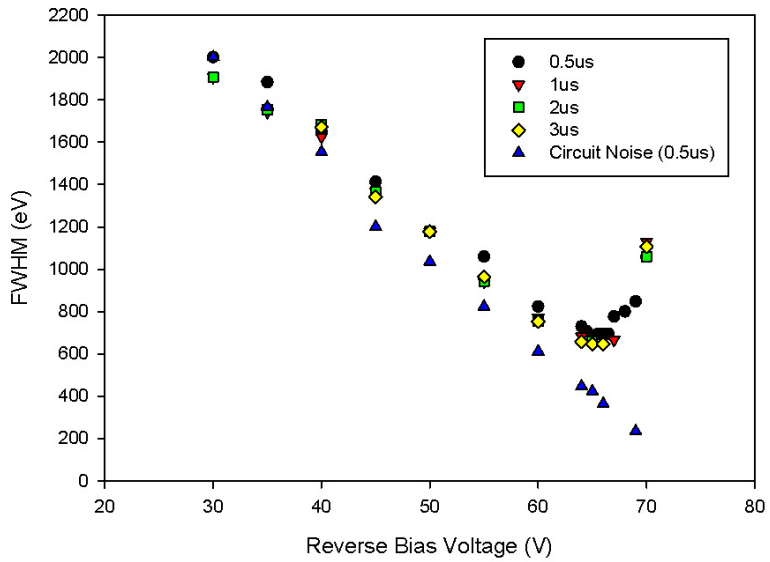

Figure 6.11: FWHM versus reverse bias Voltage of the 200 µm diameter APD D1 exposed to ^{55}Fe source and the circuit noise FWHM versus APD bias

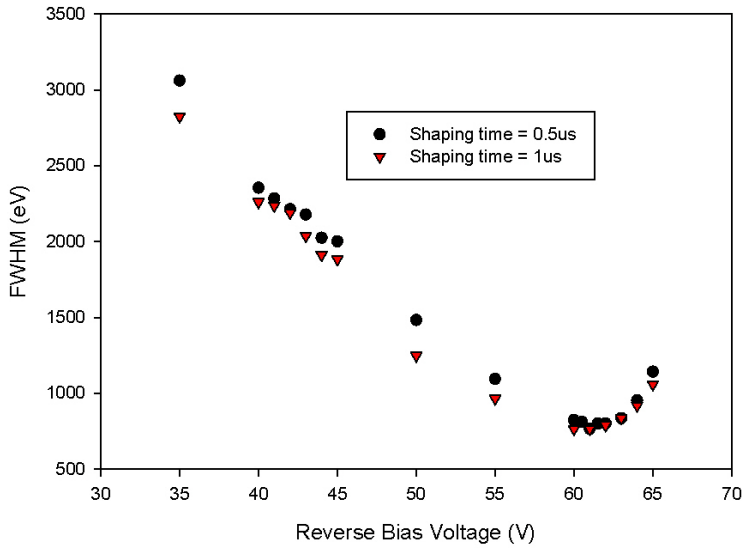

Figure 6.12: FWHM versus reverse bias Voltage of the 200 µm diameter APD D2 exposed to ^{55}Fe source

	0.5µs	1µs	2µs	3µs	Bias
D1	682eV	666eV	659eV	647eV	65 V
D2	765eV	765eV	-	-	61 V

Table 6-1: Best measured energy resolution at 5.9 keV

6.4 Discussion

The APD internal gain can help to pull the signal away from the electronic noise floor level allowing improvement in the measured FWHM energy resolution. Carriers created by absorbed X-ray photons experience avalanche gain, improving the overall signal-to-noise ratio of the system.

Linear absorption coefficient, calculated using data from [151] (weighted average of linear absorption coefficients for each element) and using equation 2.131 from section 2.4.2, was used to define the X-ray photon absorption profile within the device. The absorption of 6 keV X-ray for a total device thickness of $2.8\mu m$ was calculated and it was estimated that 32% of the incident X-ray photons will be absorbed.

When an X-ray photon is absorbed in the diode, a number of electron-hole pairs, dependant on the initial energy of the absorbed photon, are created. The position at which the electron-hole pair is created and the electron (α) and hole (β) ionisation coefficients determines the avalanche multiplication factor M. Photons absorbed in the low field absorption layer will lead to pure electron initiated multiplication, M_e. For photons absorbed in the n^+ layer, pure hole initiated multiplication, M_h, will occur. Photons absorbed within the p^- (avalanche) region will produce mixed injection. If α is greater than β, electron initiated multiplication will lead to a higher gain than hole initiated multiplication. Hence, holes in the n^+ layer that do undergo impact ionisation, will experience a lower avalanche gain. This will result in two peaks in the spectrum, which increases at a different channel number rate.

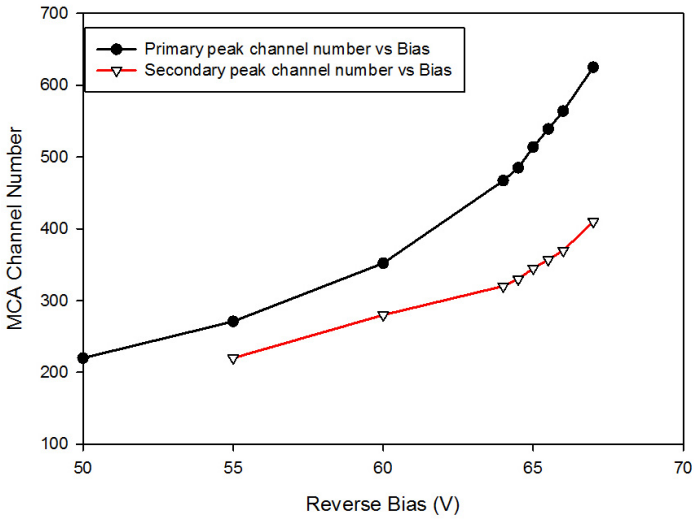

Figure 6.13: Experimental plot of channel number rate for primary and secondary peaks

For bias voltage greater than 50V, a secondary peak is observed in the lower channel numbers. This peak is attributed to X-ray photons that are absorbed in the n^+ cladding or the substrate. Such photons will experience the lower avalanche gain of M_h instead of the higher gain of M_e (the main peak). As the n^+ layer is much thinner than the combined thickness of all the layer above it, fewer electron-hole pairs will be created in that layer making the secondary peak smaller in magnitude compared to the primary peak. As the reverse bias increases, the seperation between the two peaks is seen to increase as illustrated in Figure 6.13, because of the increasing difference between the pure electron and pure hole multiplication factors. The relative height of the secondary peak can be reduced by increasing the thickness of the absorption layer, which will also reduce the device capacitance. Dependence of avalanche gain on the carrier injection position for X-ray detectors was clearly illustrated in [152], which pointed out that the secondary peaks are present if electrons and holes have unequal impact ionisation coefficient. The origins of secondary peak for X-ray detectors are also illustrated in [51].

6.5 Conclusion

$Al_{0.52}In_{0.48}P$ APDs were demonstrated as soft X-ray photon detector at room temperature. Although quantum efficiency is low for this semiconductor compound, the effect of the avalanche gain was shown to provide the desired gain which pulled the energy peak away from the noise floor and hence provided higher energy resolution. The best energy resolution (FWHM) of 647 eV was achieved for the 5.9 keV peak. A thicker absorber region would not only reduce the significance of the unwanted secondary peaks in the low channel numbers but also lead to higher detection efficiency.

The measurement in this chapter was carried out using the CSP from chapter 5 and a commercial Keithley SMU. The SMU is known to couple noise in the signal and can be filtered out partially with external RC filters. A better biasing source such as lead-acid batteries should provide a quieter system, in terms of circuit noise and provides improvement in the measured energy resolution.

The following chapter presents GaAs / $Al_{0.8}Ga_{0.2}As$ APDs as soft X-ray photon detector at room temperature.

Chapter 7 GaAs / $Al_{0.8}Ga_{0.2}As$ SAM APD for soft X-ray detection

The previous chapter presented soft X-ray spectroscopy results with novel $Al_{0.52}In_{0.48}P$. This chapter reports improved results from the SAM-APDs processed from the same wafer as those presented in [51] by Gomes *et. al*. A commercial CoolFET [67] CSP from Amptek was used by Gomes *et. al*. The new measurements were carried out with the charge sensitive preamplifier reported in Chapter 5.

7.1 Layer details and device characteristics

The SAM-APD structure was grown on a GaAs substrate by Molecular Beam Epitaxy and is presented in Table 7-1. A GaAs absorber was used due to its higher absorption coefficient compared to AlGaAs, so that a higher detection efficiency can be achieved for the same absorber thickness. The lower creation pair energy of 4.184 eV in GaAs also leads to a better spectral resolution due to a smaller fano factor of 0.12. A thin AlGaAs multiplication region was used to minimise absorption of X-ray in the multiplication region, to achieve low dark current and to reduce statisctical fluctuation in the avalanche gain process, as evidenced by the lower avalanche noise factor [153].The top p^+ and bottom n^+ layers are highly doped such that there is minimum depletion in these layers. The Multiplication region and Absorber was seperated by a p-doped charge sheet which reduces the strength of the electric field in the absorption region, allowing the carriers generated in the latter region to drift into the multiplication region.

Circular mesa diodes were fabricated and processed by using photolithographic techniques by Yu Ling Goh at the National III-V centre, Sheffield in 2010. Annular contacts were formed on the top p^- layer by depositing Au/Zn/Au. In/Ge/Au were used to form the n^+ contacts. The devices have been stored at room temperature in a laboratory

environment since being fabrication.

Capacitance-voltage (C-V) measurements are shown in Figure 7.1. The C-V measurement, shown in Figure 7.1, indicates that the device is fully depleted at bias above 12, which is intepreted as the punchthrough voltage.

Using the C-V data, the depletion width versus bias voltage and the doping profile of the SAM APD were obtained and are shown in Figure 7.2 and Figure 7.3 respectively. The bottom n^+ layers is highly doped such that there is minimum depletion in those layers. The dielectric constant of GaAs is 12.9 and the dielectric constant of $Al_{0.8}Ga_{0.2}As$ is 10.6. Assuming a one-sided depletion model and an average dielectric constant of 12, the device depletes from the bottom up, as observed in the doping profile in Figure 7.3.. The undoped avalanche region is fully depleted at 0V and a doping density lower than expected is observed for the AlGaAs charge sheet ($1.5 \times 10^{17}\ cm^{-3}$). An unexpected high doping is also observed at the boundary between the GaAs charge sheet and the absorber.

The device was packaged in a TO-5 can and current-voltage (I-V) measurements were performed prior to the X-ray spectroscopy measurement, presented in Figure 7.4. The I-V data from Gomes *et. al* is also presented for comparison. The dark current is marginally higher than those reported by Gomes *et. al* and a higher breakdown voltage (22.1 V as opposed to 22 V) is observed.

Layer	Thickness (nm)	Material	Type	Doping (cm^{-3})
Cladding	50	GaAs	p^+	1×10^{19}
	200	GaAs	p^+	2×10^{18}
Absorber	400	GaAs	i	-
Charge sheet	50	GaAs	p^-	2.6×10^{17}
	80	$Al_{0.8}Ga_{0.2}$ As	p^-	2.6×10^{17}
Avalanche	100	$Al_{0.8}Ga_{0.2}$ As	i	-
Cladding	100	$Al_{0.8}Ga_{0.2}$ As	n^+	2×10^{18}

Buffer	200	GaAs	n^+	2×10^{18}
Substrate		GaAs	n^+	

Table 7-1: Details of the GaAs / $Al_{0.8}$ $Ga_{0.2}$ As SAM APD structure

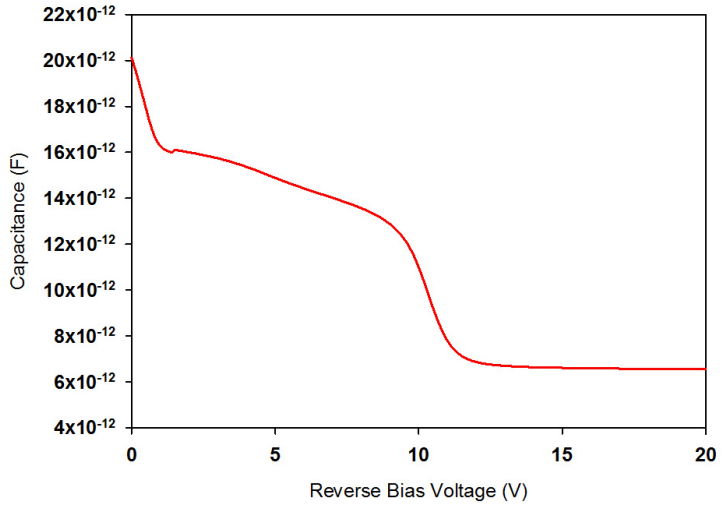

Figure 7.1: Capacitance vs Reverse Bias Voltage of the GaAs / Al0.8Ga0.2 As SAM APD

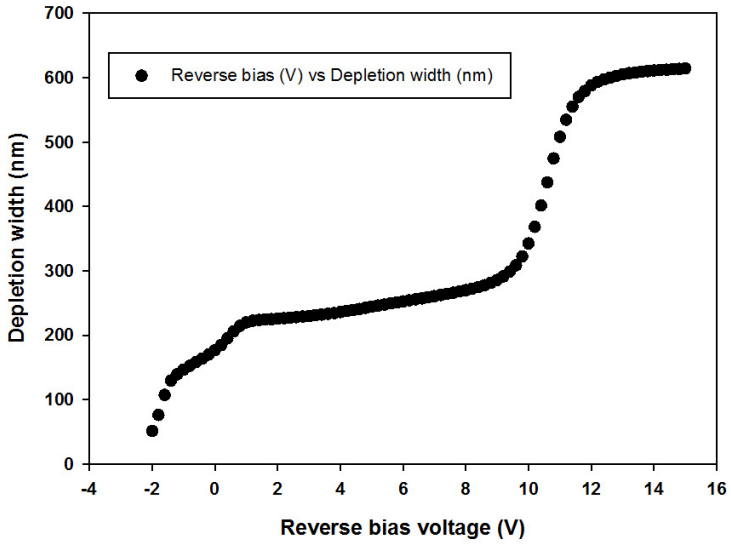

Figure 7.2: Depletion width versus bias voltage (from 2V forward to reverse voltage)

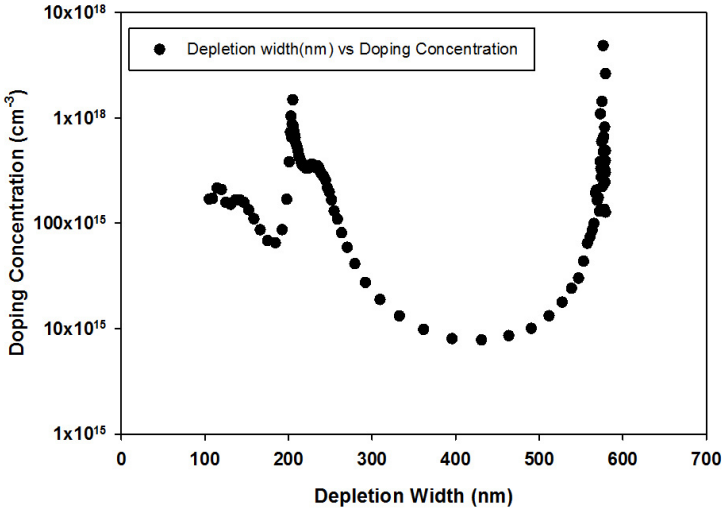

Figure 7.3: Doping density versus depletion width of the SAM APD

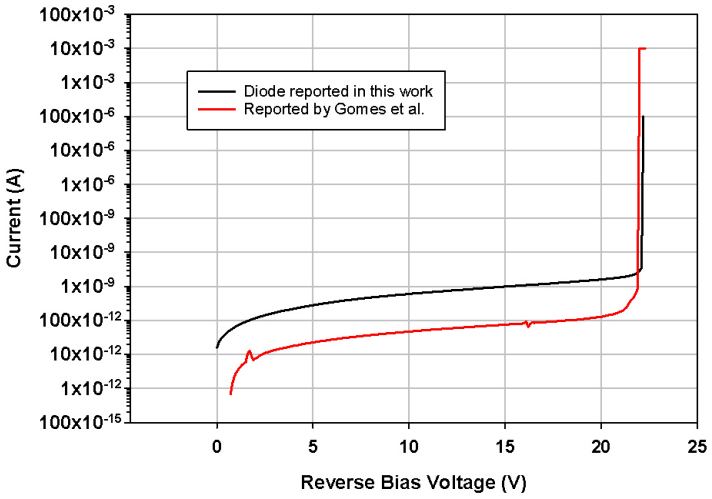

Figure 7.4: Leakage current vs Reverse Bias Voltage of the GaAs / Al0.8Ga0.2As SAM APD

7.2 X-ray response

The TO-5 can was housed with and connected to, the CSP and a 55 MBq ^{55}Fe radioisotope source was placed 0.5 cm away from the TO-5 package. The SAM-APD was biased with an external voltage source for a voltage range of 10 to 21 V and X-ray spectra were collected for each bias voltage at room temperature. The output of the CSP was shaped at $2\,\mu s$ with an Ortec 570 semi-Gaussian shaping amplifier. The X-ray measurements were performed at biases above the punchthrough to ensure that the device is fully depleted.

The collected spectra for reverse bias voltage ranging from 10 to 21 V is shown in Figure 7.5. The data was not collected for same amount of time for each bias voltage and has been normalised to facilitate comparison and fitting. The quantum, efficiency can be seen to increase with increasing bias as the peak is registered at higher channel numbers. The increase from 10 to 12 V can be attributed to increasing depletion width as shown by the decreasing capacitance in Figure 7.1. When the device is fully depleted at the punchthrough voltage of 12 V, the increase in the pulse height is attributed to the onset of avalanche gain. Therefore by taking the ratio of the peaks to that at the punchthrough voltage, the avalanche gain can be extracted, with the assumption that the gain is unity at 12 V.

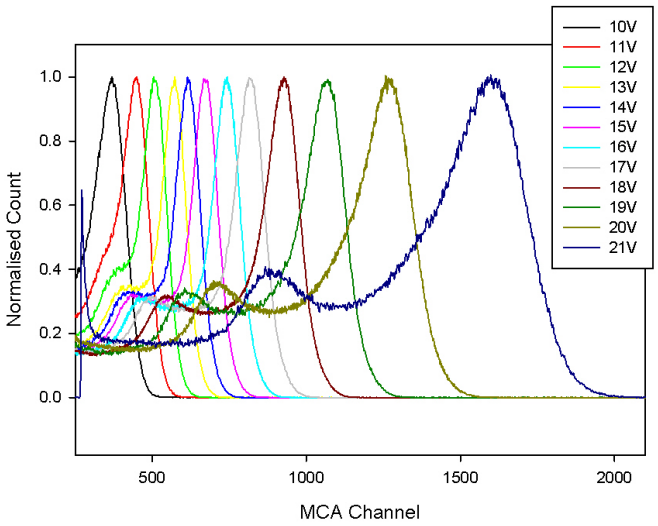

Figure 7.5: 5.9 keV spectra with different reverse bias voltage of the GaAs / Al0.8Ga0.2As SAM APD

The gain of the APD was also measured using a 442 nm laser. Unity gain is assumed to be at 12V. The SAM APD gain curves is shown in Figure 7.6. The gain obtained from X-ray measurements is lower than the gain obtained with the laser. The difference increases with increasing reverse bias voltage. The difference in gain could be attributed to space charge effect due to the point-like nature of the X-rays interaction. At high bias voltage, space charge effect may take place when absorbed X-rays results in high signal current densities, resulting in a reduced electric field and in the avalanche region [154, 155]. However, without further investigations, it is difficult to speculate the reason(s) for the difference in gain.

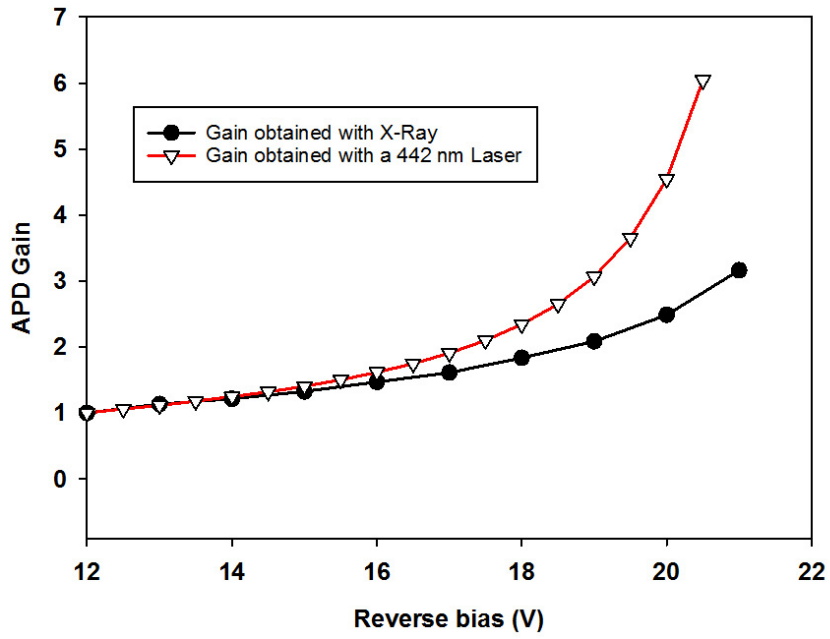

Figure 7.6: Effective avalanche multiplication factor deduced from X-ray measurements and from photocurrent measurements

The MCA was calibrated in terms of energy by using the 0 and 5.9 keV peaks as references and the FWHM was extracted from the collected spectra by performing Gaussian fittings. A comparison between the energy FWHM obtained by Gomes *et al.* and this work is shown in Figure 7.9. Despite higher dark current, a much improved FWHM of 847 eV was

achieved at a bias of 18 V compared to 1.08 keV reported by Gomes *et al.* The energy FWHM decreases with increase in reverse bias voltage up to 18 V, thereafter, the increased reverse bias voltage causes an increase in the measured FWHM. This could be attributed to an increase of leakage current, as well as a small increase the excess avalanche noise, and hence contributes to an increase in the FWHM.

The fano factor for GaAs is 0.12 according to [156] and the creation pair energy ε is 4.21 eV. Using equation 2.18, the fano limited energy resolution for an incident photon energy of 5.9 keV can be calculated to be 129 eV. The fano limited resolution is significantly smaller that the FWHM energy resolution of 847 eV obtained. This suggests a significant noise contribution from the diode or/and the measurement setup.

7.2.1 Noise measurement

To measure the noise of the system, a pulser was fed into a capacitor to create charges at the input. The pulser line was acquired together the ^{55}Fe spectrum and the FWHM in eV of the pulser line was determined after the calibration of the MCA channel scale using the 5.9 keV line, exactly as it was done for the 5.9 keV X-ray spectra. This allowed the use of the same channel calibration for the pulser and the ^{55}Fe line. This also meant that a calibrated capacitor and a calibrated voltage pulser were not needed.

The reverse bias voltage on the APD was varied from 9V to 20V and the pulser FWHM was obtained for each bias voltage. The pulser channel number remain almost the same since the system noise in mV r.m.s. does not depend significantly on the reverse bias voltage.

Since the MCA is calibrated for each APD bias voltage, the effect of the APD gain M is also taken into account for the pulser line. By performing a gaussian fitting on the pulser line, the FWHM of the pulser is obtained.

The FWHM of the pulser represents the noise of the system, which is composed of the parallel, series, 1/f and dielectric noise. The noise associated with the pulser itself will also contributes to the pulser line FWHM but it is assumed to be negligible.

Figure 7.7 shows a screenshot of the acquisition of data for one bias voltage. The 0 keV peak is only acquired for a short amount of time and then the built-in discriminator of

the MCA is set to ignore the 0 keV peak. The ^{55}Fe line was also collected to allow the MCA to be calibrated. The ^{55}Fe source was then removed and the pulser line was collected. The data collected with the pulser for different bias voltages was normalised and is presented in Figure 7.8 in terms of MCA channel number. The data shows a reduction in the channel number FWHM for a bias voltage of 9V to 10 V due to a reduction of the diode capacitance from ~14 pF to ~7 pF, which leads to a reduction in the contribution of the series noise. The FWHM in terms of MCA channels increases thereafter with increasing bias which can only be attributed to increased dark current. However, due to the effect of the APD gain when the MCA is calibrated in terms of energy (in keV), the 5.9 keV is represented by higher channel numbers and the number of MCA channels per keV is reduced which leads to a smaller keV FWHM with increasing bias.

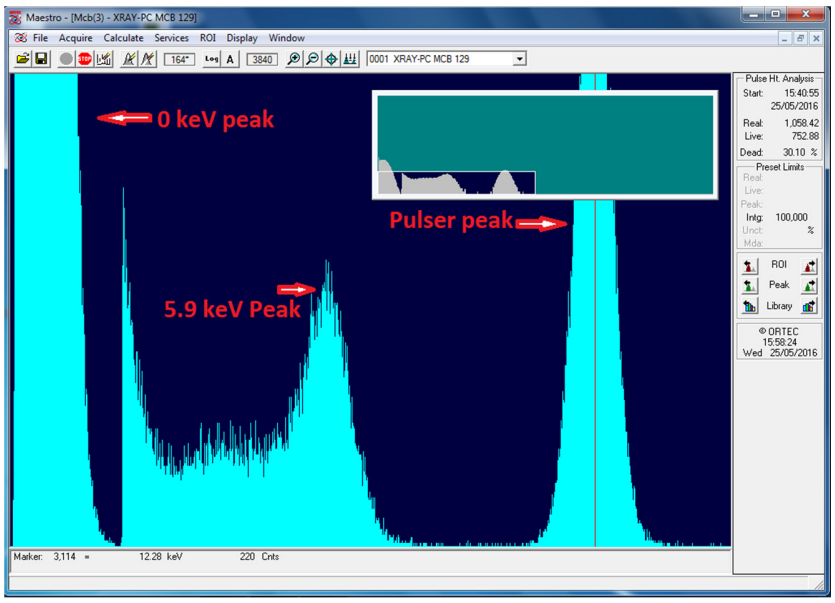

Figure 7.7: Pulser Spectrum during acquisition

The noise and energy resolution data reported by Gomes et al. are also presented in Figure 7.9 for comparison. Gomes *et al.* data also shows a decrease in both energy FWHM and noise FWHM as the bias voltage increases and the APD capacitance reduces. The reduction in FWHM from 9V to 12V is however less abrupt than that observed in this work. This indicates that the noise of the setup used by Gomes *et al.* is dominated by circuit noise contributions other than those due to the APD capacitance and leakage

current. Gomes *et al.* also observed their best energy resolution at a higher bias voltage which could be a point where the combination of the APD gain, capacitance and leakage current offers the best operating conditions for their circuit noise performance. The pulser noise is lower than the 5.9 keV energy FWHM as the pulser noise does not include Fano noise and charge trapping noise.

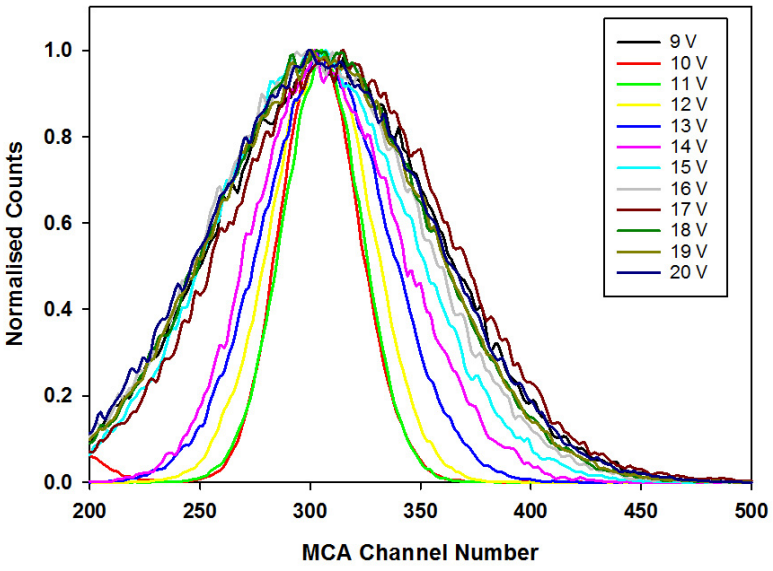

Figure 7.8: Normalised noise data acquired with the pulser

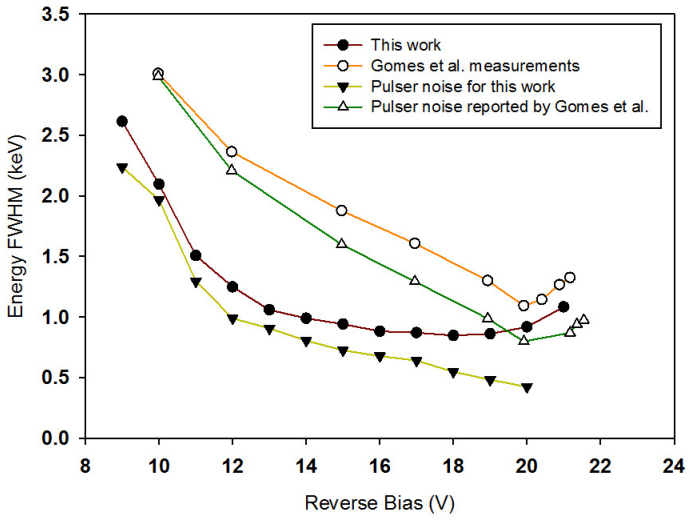

Figure 7.9: 5.9 keV FWHM vs Reverse Bias Voltage for the GaAs / Al0.8Ga0.2As SAM APD

7.2.2 Secondary Peak

For bias voltage above 12 V, a distinct secondary peak at the lower channel numbers is observed. This secondary peak was also observed for the devices discussed in chapter **6**. The secondary peak originates from avalanche multiplication initiated by holes generated by photons absorbed in the n^+ $Al_{0.8}Ga_{0.2}As$ cladding layer. Photons absorbed in the latter layer, relies on holes to undergo impact ionization and will experience a lower avalanche gain since $\beta < \alpha$ in $Al_{0.8}Ga_{0.2}As$. The detector will produce smaller signals, resulting in the secondary peak at lower energy. As the thickness of the n+ $Al_{0.8}Ga_{0.2}As$ layer is much thinner than the combined thickness of all layers above it, fewer electron-hole pairs are created in the n+ $Al_{0.8}Ga_{0.2}As$ layer than in the layers above. Thus the secondary peak is smaller in magnitude compared to the main peak.

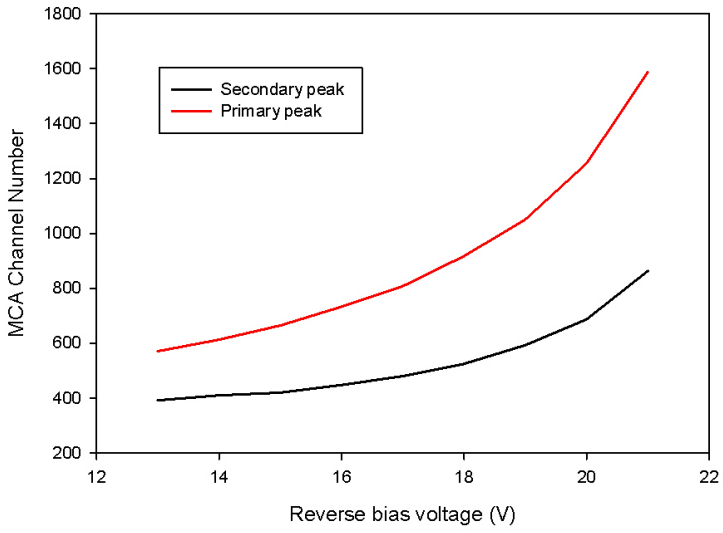

Figure 7.10: Comparison of primary and secondary peak channel numbers as a function of reverse bias

The separation between the primary and secondary peak increases as the reverse bias is increased, shown in Figure 7.10. This is because of increasing difference between the pure electron and pure hole multiplication factors, M_e and M_h respectively. Dependence of avalanche gain on the carrier injection position for X-ray detectors was clearly illustrated

in [152], which pointed out that the secondary peaks are present if electrons and holes have unequal impact ionisation coefficient. The origin of secondary peak for the same detectors reported here was discussed in [51].

7.3 Discussion

Despite the lower dark current, Gomes *et al.* report a higher FWHM energy resolution of 1.08 keV for the same devices. This suggests the SAM APD in combination with the CSP reported in this work, considerably improves the energy resolution. The initial rapid improvement in energy resolution from 10 to 12 V, is attributed to drop in capacitance as the depletion width increases. Avalanche gain can be assumed to be negligible at this point. The effect of the avalanche gain can be clearly observed from the decreasing FWHM beyond 12 V in the pulser noise. In fact the energy FWHM from this SAM-APD is smaller than a non-avalanche devices. Ng *et al.* reported a thick GaAs pin device with 6.7 μm of i-region and achieved 1 keV, measured using a CSP made by Dave Bassford, Leicester University and with similar electronic noise performance as the one used here, despite a substantially lower dark current of 0.3 pA and lower capacitance of ~2 pF [157]. The result of the GaAs pin device has however been improved with a better performing CSP and better experimental techniques[158], with an energy FWHM 745 eV at 5.9 keV.

The spectra reported by Ng *et al.* is presented in Figure 7.11 along with a spectrum obtained in this work. The smaller FWHM at 5.9 keV is a clear demonstration of the benefit of incorporating avalanche gain. The downside of using the SAM APD presented here is that the secondary peak could increase the complexity of spectral analysis when multiple energies need to be determined. In other words, in a collected spectrum, it might be difficult to determine whether the seen peaks are due to an unknown collected radiation energy or due to secondary peaks due to the SAM APD.

However insufficient suppression of mixed and hole injection leads to artifical broadening of the spectrum at lower energies. A SAM APD with a thicker absorption region is necessary to achieve pure electron injection which will in turn reduce the broadening.

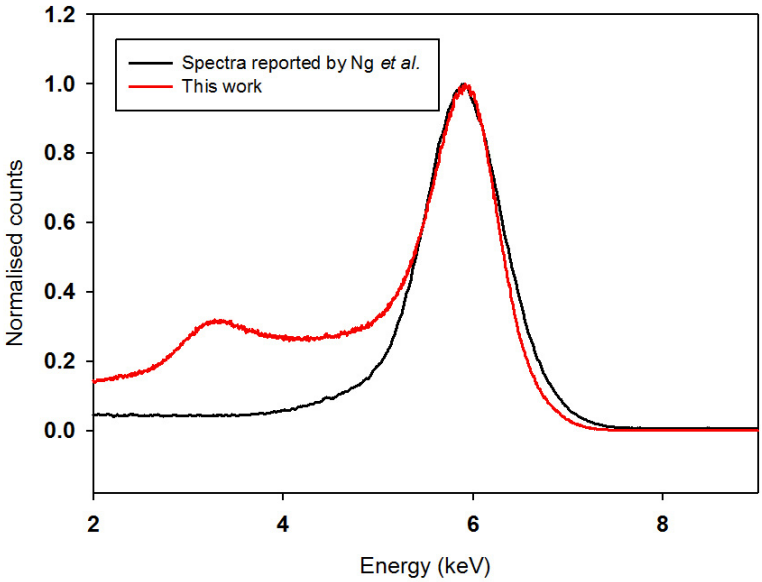

Figure 7.11: 5.9 keV spectra of GaAs detector reported by Ng (black) et al. [157] and spectra from this work (red)

7.4 Conclusion

Previously reported devices are presented here with improved performance. The improvement is due to better electronics with an FWHM energy resolution of 847 eV obtained in this work, compared to 1.08 keV obtained by Gomes *et al.* with a commercial CSP.

Additional improvement is possible by reducing the diodes' leakage current with optimised fabrication processes. An APD design with a much thicker GaAs absorber region would lead to a reduction in the APD's capacitance and would increase the quantum efficiency. It would also reduce the unwanted secondary peak at low channel numbers.

A difference between optical and X-ray gain shown in Figure 7.6 may be attributed to space charge. Further work is necessary to investigate whether space charge effect occurs in this heterojunction device.

The APDs measured in this work were fabrication by Yu Ling Goh in August 2010 and have degraded over time, which resulted in the higher dark current reported here. A

fresh batch of the APDs would give a lower dark current as reported by Gomes *et al*. and may give an even better energy resolution.

The following chapter concludes this thesis and ideas to improve the front ends are presented.

Chapter 8 Conclusion

The objectives of this work were to design low noise electronics for the characterisation and use of Avalanche photodiodes.

A transimpedance amplifier was designed, built and characterised as part of an ESA contract. The TIA was systematically characterised and benchmarked against the ESA's specifications. The TIA was also analysed numerically in addition to SPICE simulations. Despite the challenges associated with InAs, a TIA-InAs module was put together by ISDEFE, Spain. This work has been broadly successful. Additional InAs-TIA modules should be manufactured to allow the NEP to be explored.

A charge sensitive preamplifier with a noise performance better than commercially available preamplifiers such as the CoolFET from Ametek and the preamplifier previously used in Sheffield was designed. The CSP presented here gives more flexibility in terms of connecting and biasing Sheffield-grown detectors. Furthermore, the use of local feedback in the presented circuit differs from Bertuccio's circuit such that the output operating voltage is close to zero, meaning that minimum baseline restoration is required. Differences between SPICE simulations and measurement of the CSP frequency and transient responses were found to be due to a forward bias dependent gate source capacitance not modelled by the available SPICE models. Experimental evidence for significant changes in C_{GS} has been presented. Suggestions for further improvements beyond the scope of this work are provided in the next chapter.

Using the CSP designed as part of this work, the first ever AlInP room-temperature X-ray spectroscopy measurements were carried out. A resolution of 647 eV was obtained despite unwanted secondary peak in the spectra. Improvements in the device structure are required to improve the obtained results. The measurements presented in Chapter 6 were carried out at an early stage of this work. The APDs were externally biased using a commercial SMU through a *biasing resistor* and the SMU was found to couple some level of noise to the output signal. By using an electronically cleaner source, the obtained energy resolution could be further improved.

Previously reported GaAs/AlGaAs SAM APD were also characterised for X-ray detection using the CSP. Comparison between published data and data obtained in this work shows that there is a considerable improvement in energy resolution due to lower electronic contribution. Despite degradation in the APDs, an FWHM energy resolution of 847 eV was obtained. Discrepancies between X-ray and optical gain were observed and could be attributed to space charge but it is beyond the scope of this work and should form part of the future direction of this work.

In the next chapter, some ideas are presented regarding improvements to the work presented here. Some of these ideas are fully formed and some have undergone initial testing, while others are speculative and will require a great deal of effort and ingenuity to realise.

Chapter 9 Future work

The aim of this thesis was to develop front-end circuits for optical devices. In this section, ideas to improve the front ends are presented. Over the course of this work, several ideas to improve the work have been collected and some of them have been implemented with varying degree of success. The ideas presented here can provide a foundation for future work.

9.1 JFET C_{GS} dependence on dark current

The observed changes in C_{GS} in chapter 5 as dark current is changed from 14 nA to 2 µA have a significant influence on the CSP circuit's frequency and time domain behaviour and possibly also on its noise performance. To get to the bottom of what is going on, a few JFET samples should be characterised in terms of their forward biased C_{GS} behaviour and then used for measurement. Some effort will be needed to find a way of modelling the behaviour in SPICE so that prediction and measurement agree. When this has been achieved, it may be possible accurately to predict CSP noise performance for various levels of dark current using SPICE.

9.2 Improved Input stage of the Charge Sensitive preamplifier

In Figure 9.1, the Input FET is circled in red. In the current layout, the distance between the detector and the input of the FET is significant such that dielectric noise contribution is major. The proximity of lossy dielectric materials at the preamplifier input can also lead to an increase in the parallel noise contribution. To minimize the parallel and dielectric noise contributions, which can be some situations quite significant in magnitude, the circuit design can be altered to keep the input traces on the circuit board as short as possible. The circuit substrate is itself the lossy source introducing these noises.

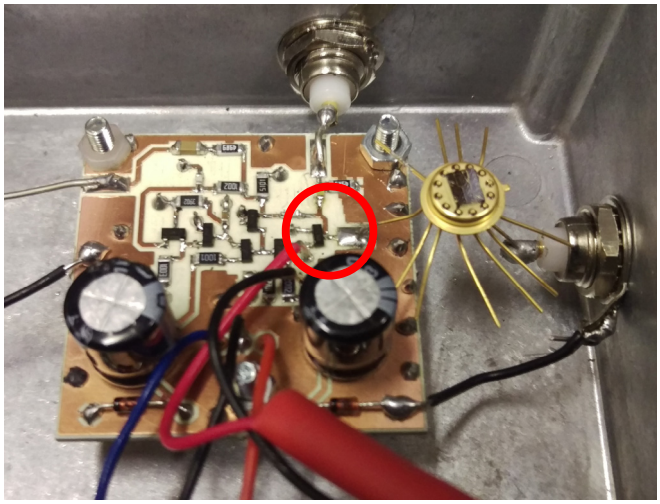

Figure 9.1: CSP circuit with detector at input

In order to improve the setup, the legs on the detector should be shortened and soldered directly on the JFET's gate pad.

From private conversation with Dr Anna Barnett, University of Sussex, it was concluded that a surface mount JFET can but not always contribute more dielectric noise compared to a JFET packaged in a TO-can. These claims have not been proven scientifically yet and should form part of the future experiments for this work.

The dielectric losses of the epoxy encapsulated JFET devices also affects the noise performance and was discussed by Radeka [100]. InterFET Corp sells the 2N4416 JFET in a TO-Can without any epoxy encapsulation. To reduce the dielectric noise contribution, the JFET can be "decanned". An attempt to "decan" an InterFET 2N4416 is shown in Figure 9.2. The epoxy used to secure the JFET die to the TO-can can also contribute to more dielectric noise.

Figure 9.2: Decanned FET

An altered layout of the circuit is shown in Figure 9.3. The circuit shown makes use of an input JFET packaged in a TO-Can. This circuit would enable the noise due to JFET packaging techniques to be analysed.

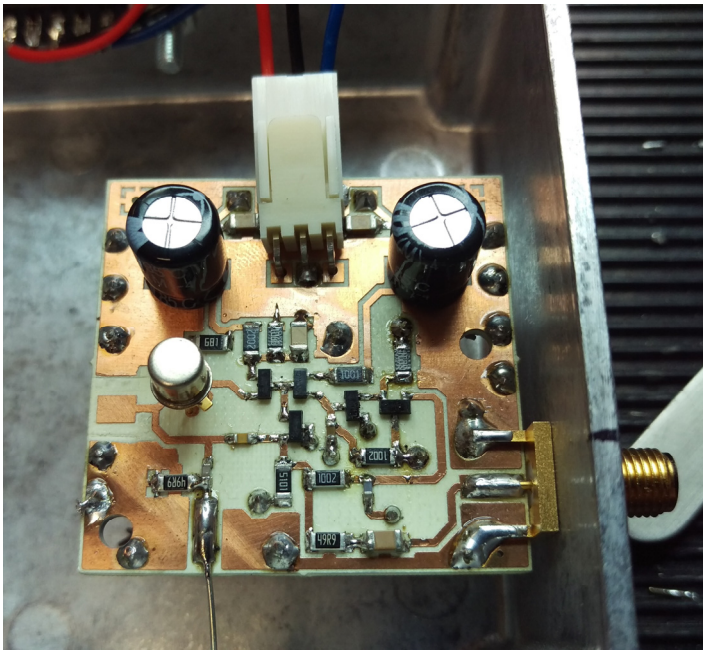

Figure 9.3: CSP with a TO-Can input JFET

To further reduce the distance between the detector and the input JFET, they can both be packaged on the same TO-can and linked together with a wire bonder. One downside is

that the exposed JFET may also be radiated by radioactive source during spectroscopy measurement. The JFET dies will also need to be fully characterised with the help of a probe station prior to being packaged with detectors.

9.3 Peltier-cooled input JFET for Charge Sensitive preamplifier

Commercially available CSP such as the CoolFET from Amptek makes use of a Peltier-cooled input JFET. Cooling the JFET reduces the series and parallel noise contribution, providing a lower total electronic noise. The JFET on die shown in Figure 9.4 can be easily mounted on a Peltier cooler with the detector. Cooling the JFET would reduce the gate-to-source leakage current leading to a lower parallel noise contribution. The JFET's transconductance should also increase, improving the signal to noise ratio. Pullia *et al.* achieved a noise performance of 41 rms electrons (350 eV) at 25 °C. They improved the noise resolution to 22 rms electron (190 eV) with a Peltier cooled JFET packaged directly under the detector [85]. However this is still higher that the noise performance of 17 electrons r.m.s that was achieved by Bertuccio without cooling [133].

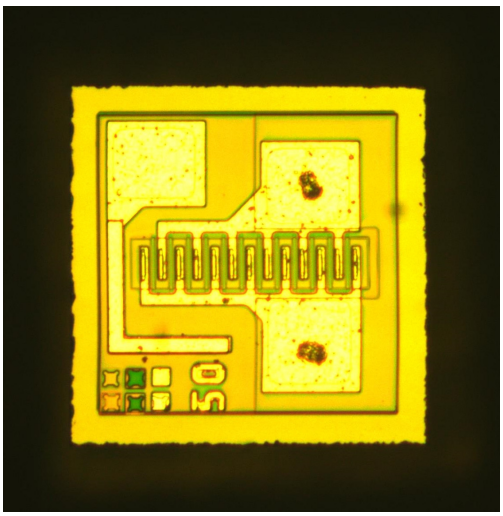

Figure 9.4: 2N4416 Die

Chapter 10 Appendices

10.1 Typical InAs APD Characteristics and ESA's Specifications

Parameter	Value	Comments
Operating wavelength range	500-3500 nm	
Spectral response	To be measured over the operating wavelength range at M = 1 and M=10.	
Reference wavelength	2000 nm	Wavelength for performance verification and LIDAR mode measurements.
Detector quantum efficiency	>60%	At reference wavelength, including AR coating.
Active area diameter	≥200 μm	Detector must have single pixel functionality
Excess noise factor (F)	<2.0	At M = 10
Operating temperature	>200 K	Performance between 150 to 250 K shall be evaluated.
Input signal/dynamic range	Maximum pulse repetition frequency: 1kHz (TBC) Minimum: 8000 Maximum: $2x10^6$	To be used for LIDAR mode measurements. Number of photons arriving in 50-200 ns period. Useful dynamic range over which specified performance is to be achieved.
Bandwidth	>20 MHz	Refers to detector-pre-amplifier combination. Persistence effects shall also be investigated.
NEP	<100fW/$\sqrt{Hz}$	At operating wavelength. Input radiant power for a signal to noise ratio of unity at the output of pre-amplifier at operating bandwidth. (Includes detector and pre-amplifier contributions, at operating bandwidth).
Gain stability	0.1% r.m.s.	Over 60 s period. Target: <0.01% over 10 s. At the output of pre-amplifier.
Linearity	5% r.m.s.	Deviation from best linear fit over useful dynamic range, at the output of pre-amplifier.
Total ionising dose	5 krad (Si) minimum	No performance change.
Proton irradiation	$1x10^{10}$ p/cm^2	At 10 MeV equivalent. Dark current increase < 10%.

10.2 TIA approximate transfer function with a 1st Order opamp model

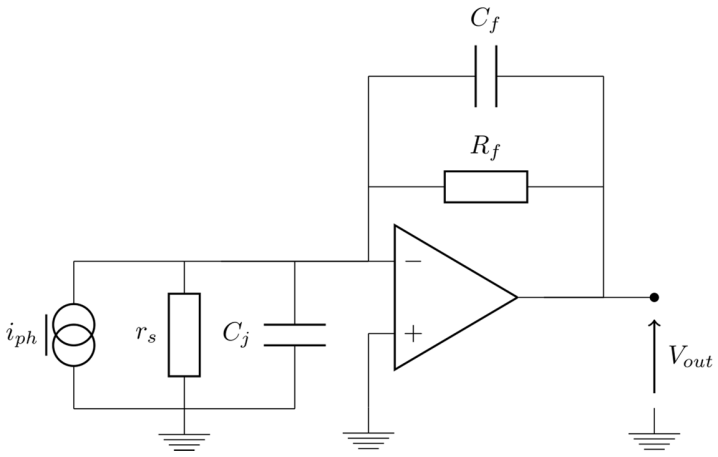

Figure 10.1: APD Small Signal model with TIA

Summing currents at inverting node of the opamp:

$$\frac{V_{out}-v^-}{Z_f} = \frac{v^-}{Z_s} - i_{ph} \tag{10.1}$$

where Z_f is the combined impedance of $R_f//C_f$ and Z_s is the combined impedance of $r_s//C_j$.

The opamp equation is given by:

$$V_{out} = A_v(v^+ - v^-) \tag{10.2}$$

A first order opamp model equation is given by:

$$A_v = \frac{A_0}{1+s\tau_0} \tag{10.3}$$

Substituting equation 10.2 and 10.3 in 10.1 with $v_+ = 0$, V_{out} can be shown to equate to:

$$V_{out} = -\frac{A_0 R_f r_s i_{ph}}{R_f r_s \tau_0 (C_f+C_j)s^2+(A_0 C_f R_f r_s+C_f R_f r_s+R_f C_j r_s+R_f \tau_0+r_s \tau_0)s+A_0 r_s+R_f+r_s} \tag{10.4}$$

The transimpedance of the circuit can be written as:

$$\frac{V_{out}}{i_{ph}} =$$

$$-R_f\left[\frac{A_0 r_s}{A_0 r_s + R_f + r_s}\right]\left[\frac{1}{\frac{(C_f R_f r_s \tau_0 + R_f C_j r_s \tau_0)s^2}{A_0 r_s + R_f + r_s} + \frac{(A_0 C_f R_f r_s + C_f R_f r_s + R_f C_j r_s + (R_f + r_s)\tau_0)s}{A_0 r_s + R_f + r_s} + 1}\right] \quad (10.5)$$

... and factorised:

$$\frac{V_{out}}{i_{ph}} = -R_f\left[\frac{A_0 r_s}{A_0 r_s + R_f + r_s}\right]\left[\frac{1}{1 + \frac{(A_0 C_f R_f + C_f R_f + R_f C_j + \frac{R_f \tau_0}{r_s} + \tau_0)s}{A_0 + \frac{R_f}{r_s} + 1} + \frac{(C_f R_f \tau_0 + R_f C_j \tau_0)s^2}{A_0 + \frac{R_f}{r_s} + 1}}\right] \quad (10.6)$$

If r_s is much bigger than R_f, $\frac{R_f}{r_s}$ will be very small and can be ignored. A_0 is about 6300 for the LMH6624 Opamp. Therefore this term, $A_0 + \frac{R_f}{r_s} + 1$, can be reduced to A_0.

$$\frac{V_{out}}{i_{ph}} = -R_f\left[\frac{A_0 r_s}{A_0 r_s + R_f + r_s}\right]\left[\frac{1}{1 + \frac{(A_0 C_f R_f + C_f R_f + R_f C_j + \frac{R_f \tau_0}{r_s} + \tau_0)s}{A_0} + \frac{(C_f R_f \tau_0 + R_f C_j \tau_0)s^2}{A_0}}\right] \quad (10.7)$$

$$\frac{V_{out}}{i_{ph}} = -R_f\left[\frac{A_0 r_s}{A_0 r_s + R_f + r_s}\right]\left[\frac{1}{1 + \left(C_f R_f + \frac{(C_f + C_j)R_f}{A_0} + \frac{\tau_0}{A_0}\left(1 + \frac{R_f}{r_s}\right)\right)s + \frac{R_f \tau_0 (C_f + C_j)s^2}{A_0}}\right] \quad (10.8)$$

$\left[\frac{A_0 r_s}{A_0 r_s + R_f + r_s}\right]$ is approximately equal to 1 if r_s is bigger than R_f which gives:

$$\frac{V_{out}}{i_{ph}} = -R_f\left[\frac{1}{1 + \left(C_f R_f + \frac{(C_f + C_j)R_f}{A_0} + \frac{\tau_0}{A_0}\left(1 + \frac{R_f}{r_s}\right)\right)s + \frac{R_f \tau_0 (C_f + C_j)s^2}{A_0}}\right] \quad (10.9)$$

$$\omega_n = \sqrt{\frac{A_0}{(C_j+C_f)R_f\tau_0}} \tag{10.10}$$

$$\xi = \frac{\sqrt{R_f}}{2\sqrt{(C_f+C_j)\tau_0}}\left(C_f + \frac{C_j}{A_0}\right) \tag{10.11}$$

if C_f is 0:

$$\frac{V_{out}}{i_{ph}} = -R_f\left[\frac{1}{1+\left(\frac{R_fC_j}{A_0}+\frac{\tau_0}{A_0}\left(1+\frac{R_f}{r_s}\right)\right)s+\frac{R_fC_j\tau_0s^2}{A_0}}\right] \tag{10.12}$$

From equation 10.5, an exact equation for the damping factor ξ can be found to equal to:

$$\xi = \frac{C_fR_fr_s(A_0+1)+R_fC_jr_s+(R_f+r_s)\tau_0}{2(A_0r_s+R_f+r_s)\sqrt{\frac{R_fr_s\tau_0(C_f+C_j)}{A_0r_s+R_f+r_s}}} \tag{10.13}$$

10.3 TIA noise analysis

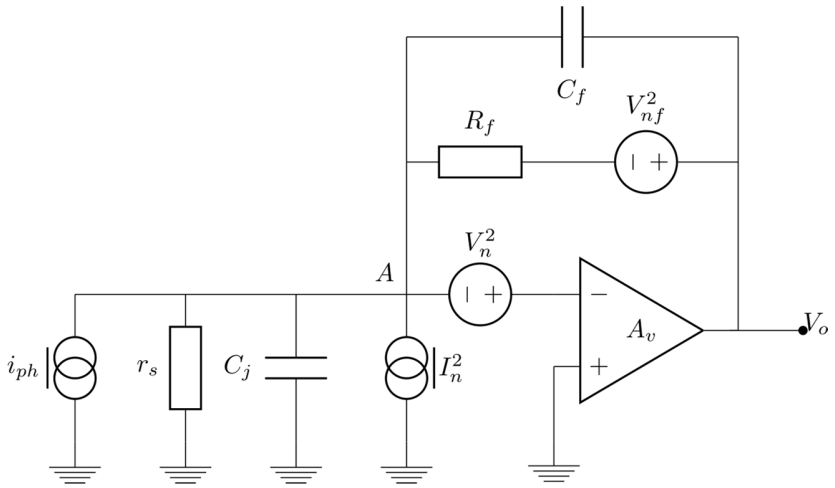

Figure 10.2: TIA Noise model

Consider Figure 10.2:

Looking at the effect of V_n;

Summing current at node A:

$$\frac{V^- - V_n}{Z_s} = \frac{V_o - V^- + V_n}{Z_f} \tag{10.14}$$

$$V^- = -\frac{V_o}{A_f} \tag{10.15}$$

Substituting equation 10.15 into equation 10.14 gives:

$$\frac{-\frac{V_o}{A_f} - V_n}{Z_s} = \frac{V_o + \frac{V_o}{A_f} + V_n}{Z_f} \tag{10.16}$$

Isolating V_o...

$$V_o = \frac{-A_f Z_f V_n - A_f Z_s V_n}{A_f Z_s + Z_f + Z_s} \tag{10.17}$$

Simplifying...

$$\frac{V_o}{V_n} = -\frac{A_f(Z_f+Z_s)}{A_f Z_s+Z_f+Z_s} \tag{10.18}$$

Z_s and Z_f are given by:

$$Z_s = \frac{r_s}{1+sC_j r_s} \tag{10.19}$$

$$Z_f = \frac{R_f}{1+sC_f R_f} \tag{10.20}$$

Substituting into 10.18:

$$\frac{V_o}{V_n} = -\frac{A_f\left(\frac{R_f}{C_f R_f s+1}+\frac{r_s}{C_j r_s s+1}\right)}{\frac{A_f r_s}{C_j r_s s+1}+\frac{R_f}{C_f R_f s+1}+\frac{r_s}{C_j r_s s+1}} \tag{10.21}$$

$$\frac{V_o}{V_n} = -\frac{A_f\left(R_f+r_s+sR_f r_s(C_j+C_f)\right)}{sR_f r_s(A_f C_f+C_f+C_j)+A_f r_s+R_f+r_s} \tag{10.22}$$

Assuming a first order open loop gain transfer function for the opamp given by:

$$A_f = \frac{A_0}{1+s\tau_0} \tag{10.23}$$

$$\frac{V_o}{V_n} = -\frac{A_0\left(R_f+r_s+sR_f r_s(C_j+C_f)\right)}{(1+s\tau_0)\left(R_f r_s\left(\frac{A_0 C_f}{1+s\tau_0}+C_f+C_j\right)s+\frac{A_0 r_s}{1+s\tau_0}+R_f+r_s\right)} \tag{10.24}$$

Looking at the effect of V_{nf}; Summing current at node A:

$$(V_o - V^-)sC_f + \frac{(V_o - v_{nf} - V^-)}{R_f} = \frac{V^-}{Z_s} \tag{10.25}$$

Substituting equation 10.15 in 10.25 and isolating $\frac{V_o}{v_{nf}}$:

$$\frac{V_o}{v_{nf}} = \frac{A_f Z_s}{(A_f C_f R_f Z_s+C_f R_f Z_s)s+A_f Z_s+R_f+Z_s} \tag{10.26}$$

Substituting A_f with a first order opamp model and Z_s by equation 10.19:

$$\frac{V_o}{v_{nf}} = \frac{A_0 r_s}{\left(A_0 r_s + R_f + r_s\right)\left(1 + \frac{R_f r_s \tau_0 \left(C_f + C_j\right)s^2}{A_0 r_s + R_f + r_s} + \frac{\left(C_f R_f r_s (A_0+1) + C_j R_f r_s + \left(R_f + r_s\right)\tau_0\right)s}{A_0 r_s + R_f + r_s}\right)} \quad (10.27)$$

10.4 Measurement with AlInP APD

A 400 µm diameter $Al_{0.52}In_{0.48}P$ APD coupled to the TIA circuit was characterised as illustrated in Figure 10.3. Details of the device structure are presented in chapter 6. The AlInP homojunction SAM-APD grown on lattice matched
GaAs has a peak response at 480 nm with a narrower FWHM of 22 nm and a responsivity of 20 A/W. The following test were carried out to show the effect on a signal in the presences of a white light source.

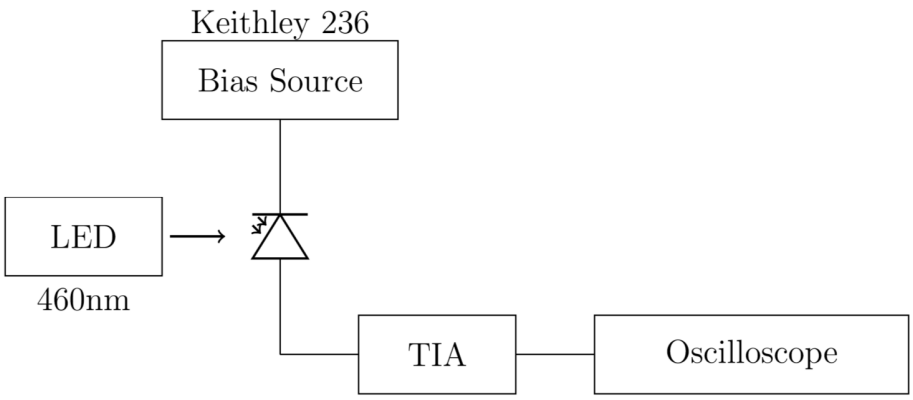

Figure 10.3 : System block diagram of measurement system

Photocurrent versus bias measurement was carried out on the setup using a 480nm LED and a white light source. For comparison, the same tests were carried out on a silicon APD S2381 from Hamamatsu. The results are shown in Figure 10.4.

To evaluate the AlInP APD as a detector in the presence of ambient light, a tungsten light bulb, with an irradiance of $1kWm^{-2}$, was shone on both the AlInP APD and the Si APD and a modulated 480 nm LED was also focused on the them. Both devices were reversed biased to give similar multiplication. Waveforms collected on the oscilloscope are shown in Figure 10.5. At low gain, the Si APD shows it superiority over the AlInP APD but at higher gain, the signal

from the AlInP-TIA setup was retrieved while the Si-TIA setup was dominated by the white light source. The photocurrent induced due to the white light source on the the Si APD was found to be 30 times higher than the one induced due to the 480 nm LED signal as illustrated in Figure 10.5.

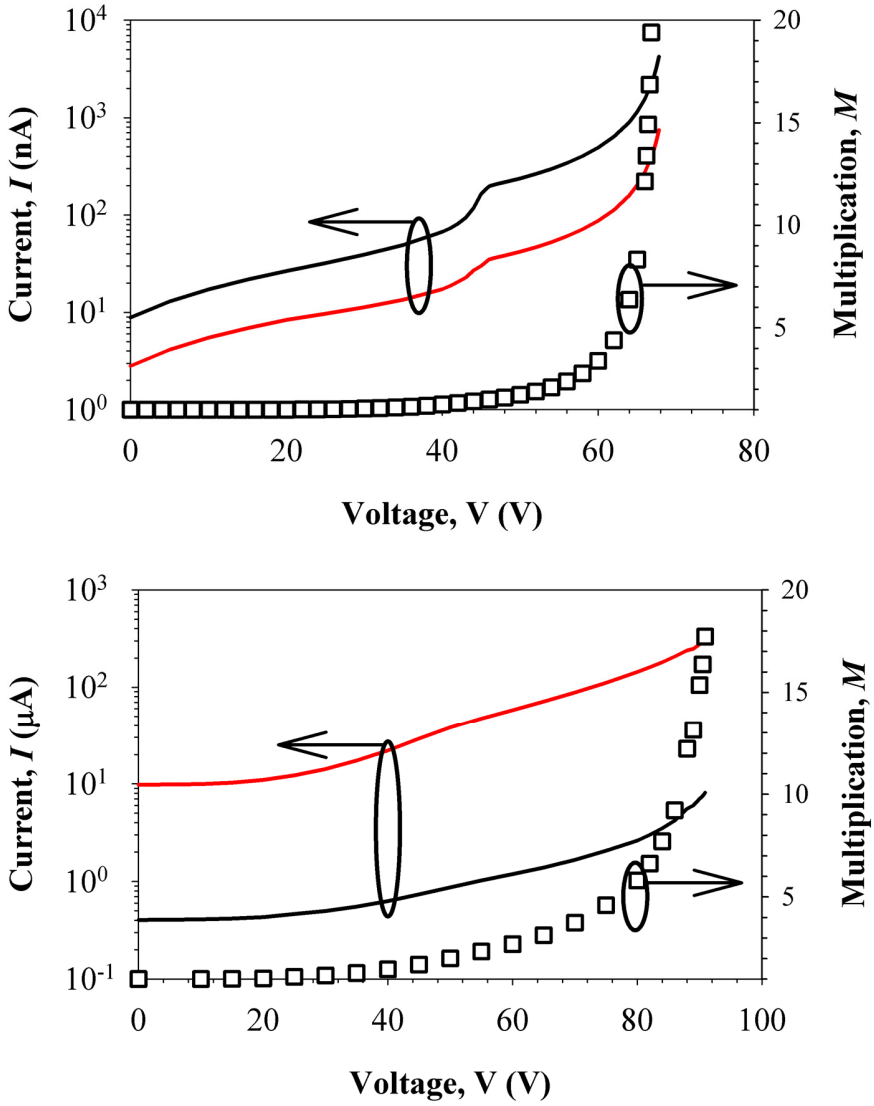

Figure 10.4: Multiplication (symbols) and photocurrent vs reverse bias voltage under illumination of 480 nm (black) and under the presence of white light source (red) measured in AlInP APD (top) and silicon APD S2381 (bottom).

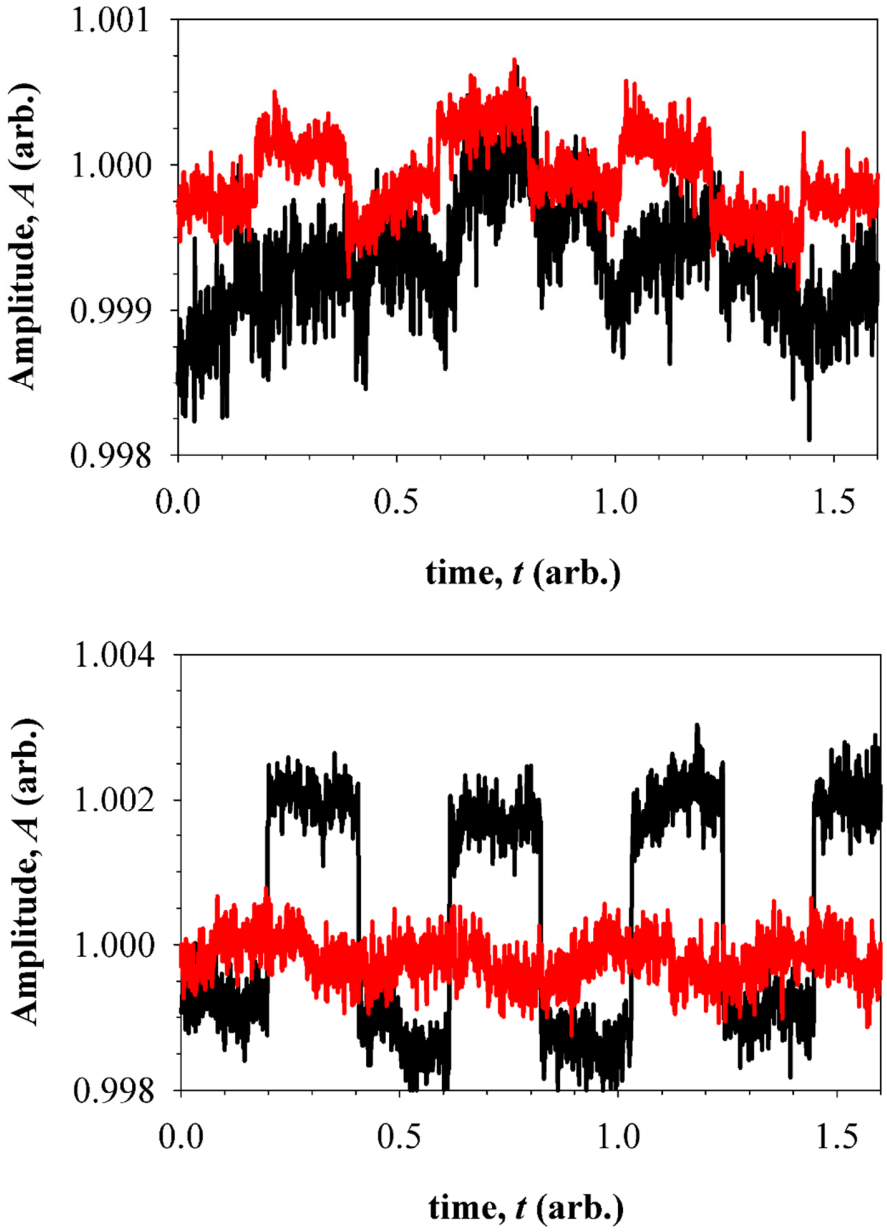

Figure 10.5: Waveform retrieved by AlInP APD (black) and S2381 (red) at an avalanche gain of ~2 (top) and ~20(bottom) under illumination of 480 nm signal and irradiance of 1kWm^{-2}

10.5 CSP SPICE schematic

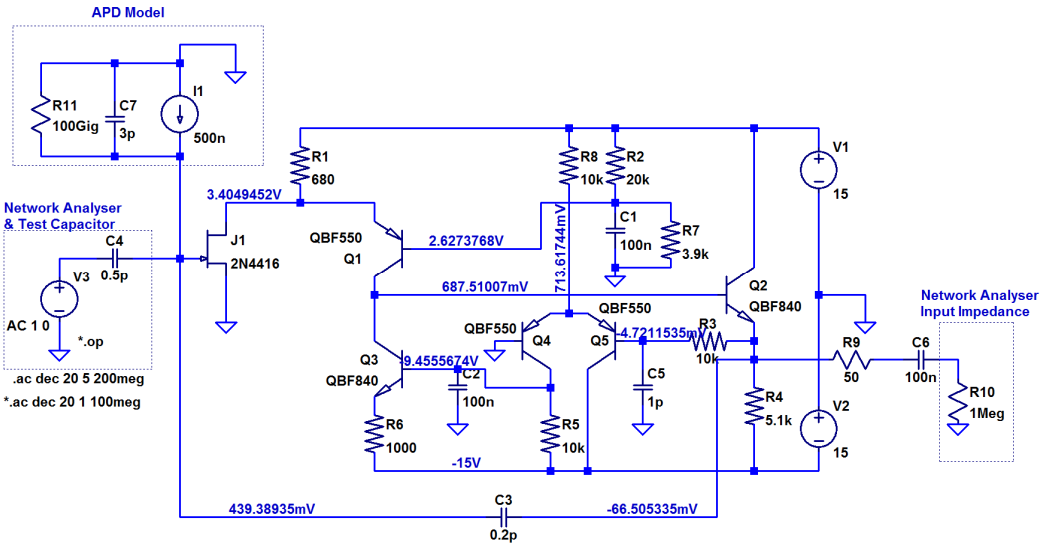

10.6 CSP frequency responses

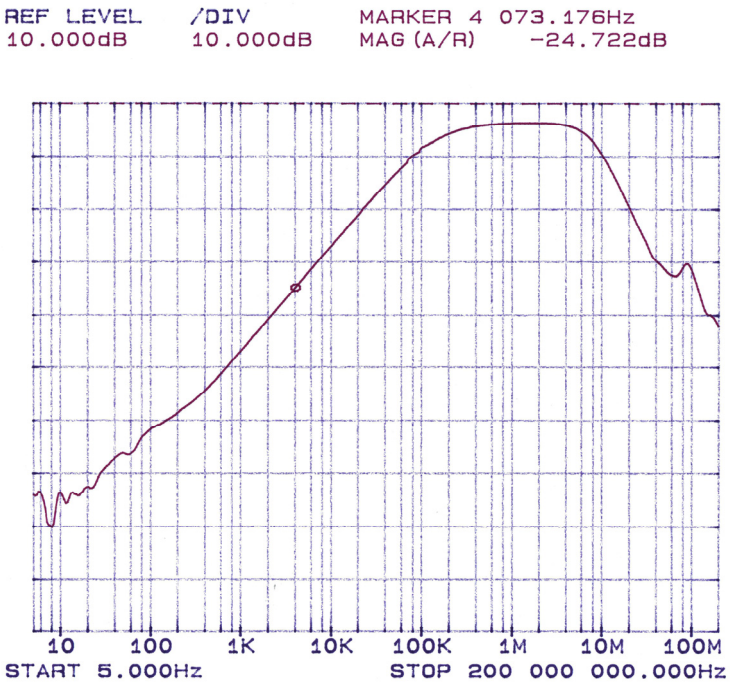

Figure 10.6: Frequency response of CSP with a dark current of 0.1 nA

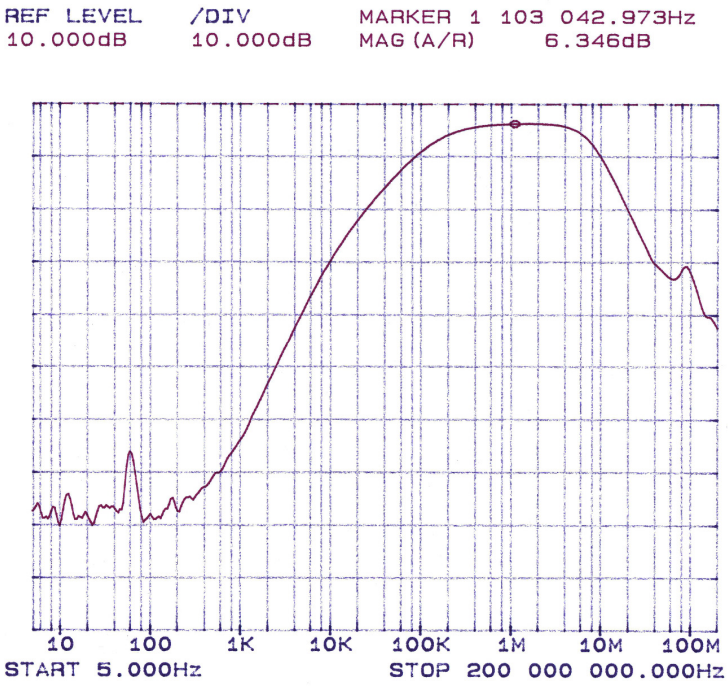

Figure 10.7: Frequency response of CSP with a dark current of 14 nA

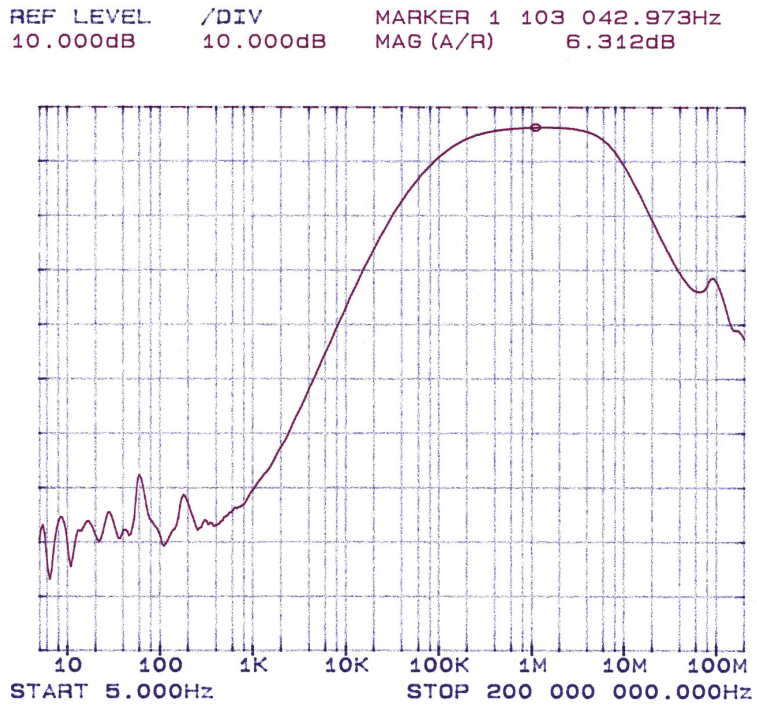

Figure 10.8: Frequency response of CSP with a dark current of 50 nA

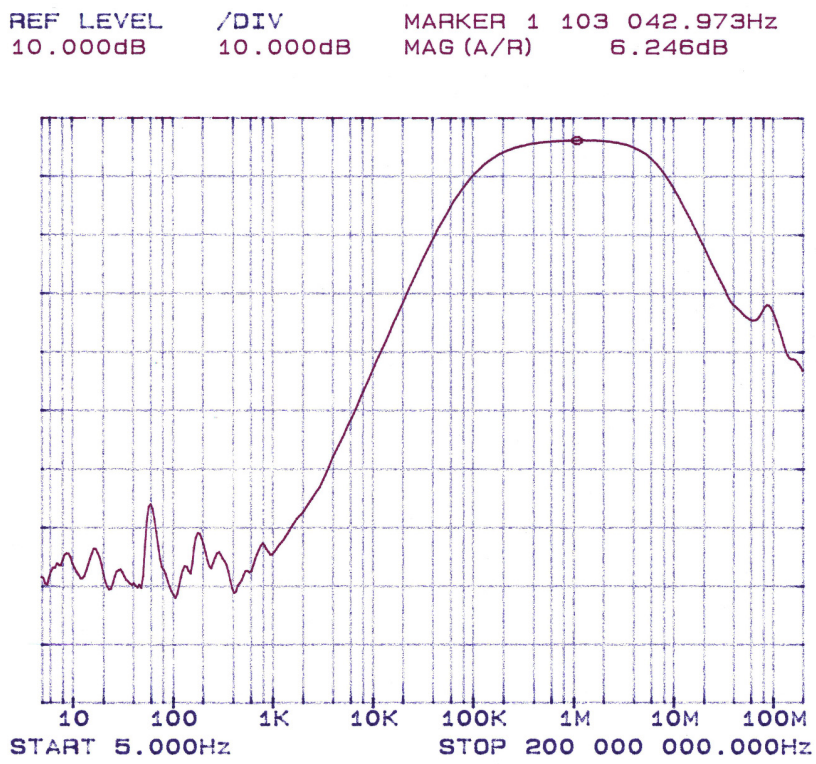

Figure 10.9: Frequency response of CSP with a dark current of 110 nA

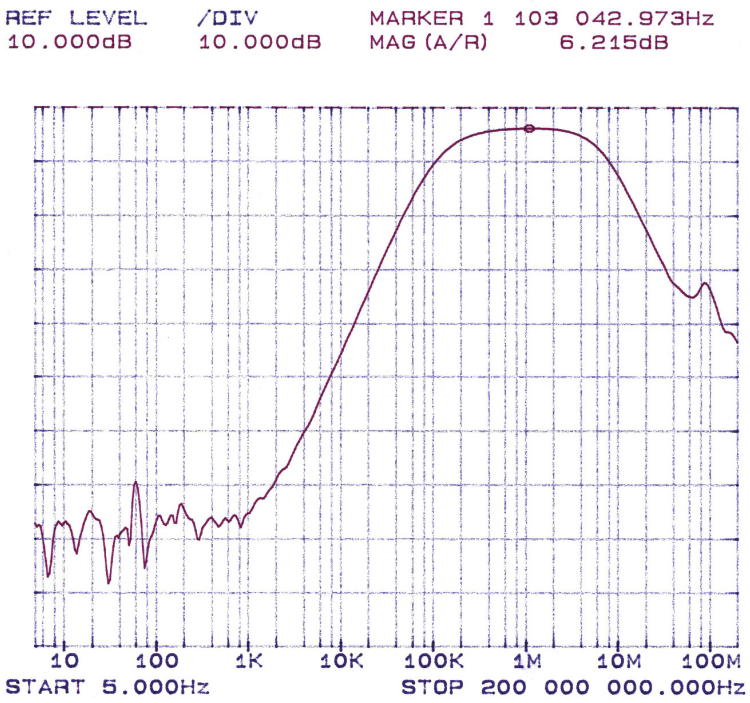

Figure 10.10: Frequency response of CSP with a dark current of 150 nA

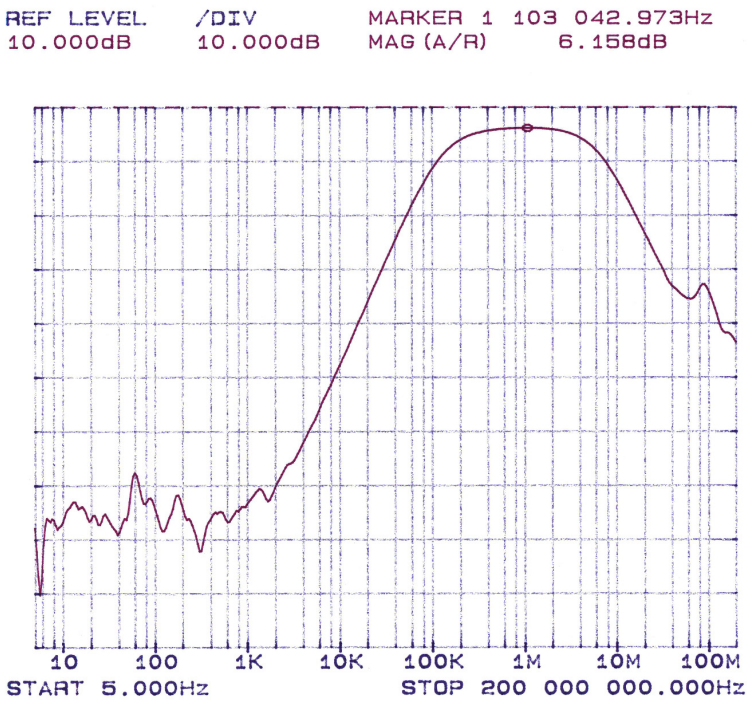

Figure 10.11: Frequency response of CSP with a dark current of 200 nA

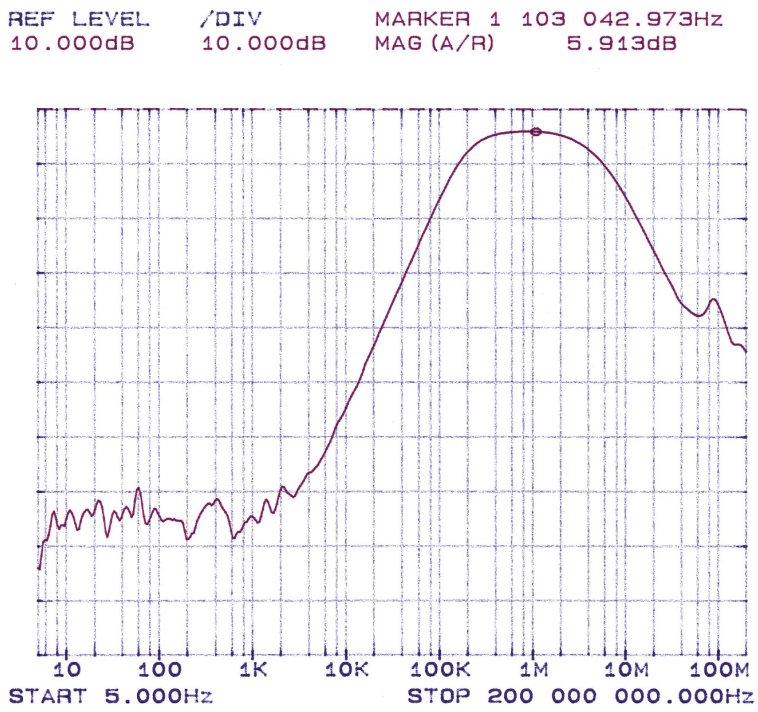

Figure 10.12: Frequency response of CSP with a dark current of 500 nA

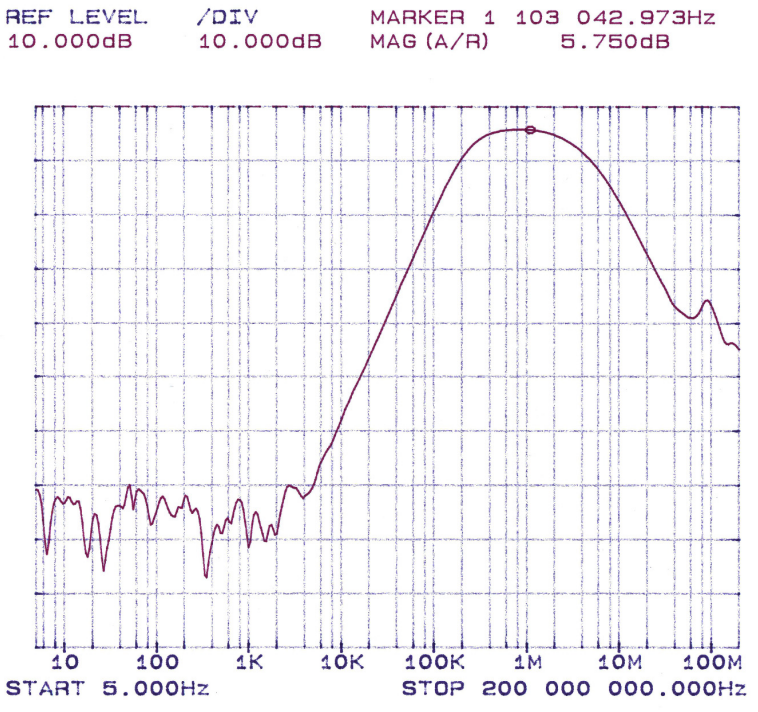

Figure 10.13: Frequency response of CSP with a dark current of 750 nA

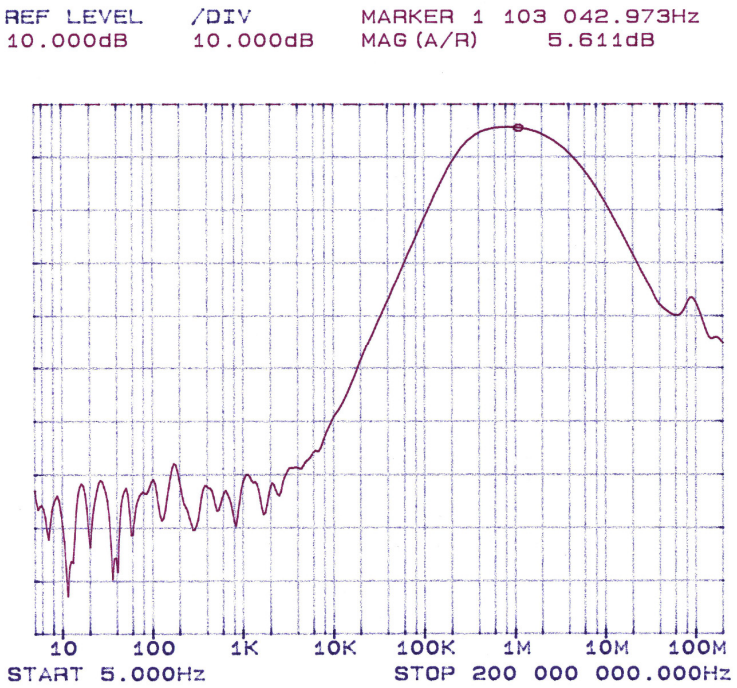

Figure 10.14: Frequency response of CSP with a dark current of 1 uA

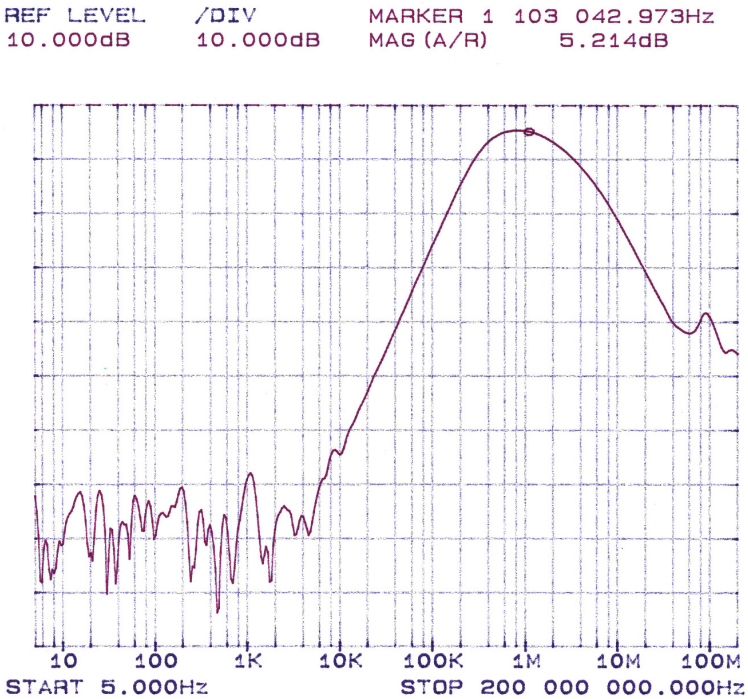

Figure 10.15: Frequency response of CSP with a dark current of 2 uA

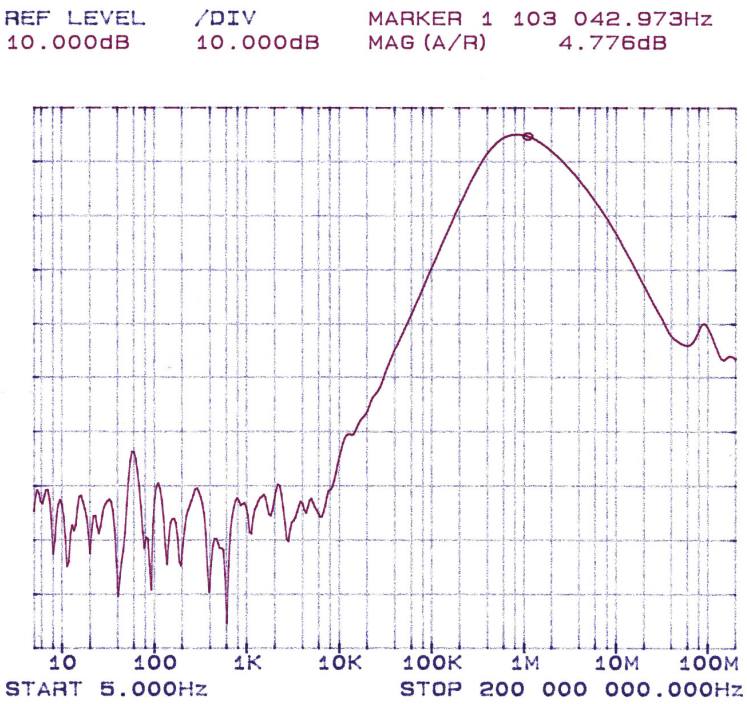

Figure 10.16: Frequency response of CSP with a dark current of 4 uA

References

[1] M. Rast, J. L. Bezy, and S. Bruzzi, "The ESA Medium Resolution Imaging Spectrometer MERIS a review of the instrument and its mission," *International Journal of Remote Sensing,* vol. 20, pp. 1681-1702, 1999.

[2] E. A. Johnson, R. C. Meyer, R. E. Hopkins, and W. H. Mock, "The Measurement of Light Scattered by the Upper Atmosphere from a Search-Light Beam," *J. Opt. Soc. Am.,* vol. 29, pp. 512-517, 1939.

[3] E. H. Synge, "XCI. A method of investigating the higher atmosphere," *The London, Edinburgh, and Dublin Philosophical Magazine and Journal of Science,* vol. 9, pp. 1014-1020, 1930.

[4] M. A. Tuve, E. A. Johnson, and O. R. Wulf, "A new experimental method for study of the upper atmosphere," *Terrestrial Magnetism and Atmospheric Electricity,* vol. 40, pp. 452-454, 1935.

[5] R. Bureau, "La Météorologie 3," *Terrestrial Magnetism and Atmospheric Electricity,* pp. 292-292, 1946.

[6] E. O. Hulburt, "Observations of a Searchlight Beam to an Altitude of 28 Kilometers," *J. Opt. Soc. Am.,* vol. 27, pp. 377-382, 1937.

[7] F. J. McClung and R. W. Hellwarth, "Giant Optical Pulsations from Ruby," *Journal of Applied Physics,* vol. 33, 1962.

[8] E. E. Uthe and W. B. Johnson, "Lidar observations of the lower tropospheric aerosol structure during BOMEX. Final report," 1971.

[9] NASA, "Science objectives of the Atmospheric, Magnetospheric and Plasmas in Space (AMPS) Payload for Spacelab/Shuttle," 1973.

[10] ESRO, "Atmospheric Research Using Spacelab-borne Lasers, ESRO MS(74)5, NewYork," 1974.

[11] NASA, "Shuttle Atmospheric Lidar Research Program, NASA SP-433," 1979.

[12] ESA, "Space Laser Applications and Technology (SPLAT) Workshop, ESA SP-202," 1984.

[13] NASA, "Lidar AtmosphericWind Sounder and Altimeter (LASA) Instrument Panel Report, NASA TM 86129, IId," 1987.

[14] NASA, "Laser AtmosphericWind Sounder (LAWS) Instrument Panel Report, NASA TM 86129, IIg," 1987.

[15] ESA, "Laser Sounding from Space, ESA SP-1108," 1989.

[16] ESA, "ALADIN, Atmospheric Laser Doppler Instrument, ESA SP-1112," 1989.

[17] R. Moore, "Using Light to Probe the Heights of the Atmosphere and the Depths of the Ocean," ed.

[18] NASA, "Jet Propulsion Laboratory," ed.

[19] NASA, "Lidar Applications Group," ed.

[20] NASA, "Goddard's LiDAR, Hyperspectral and Thermal Imager," ed.

[21] NASA, "Lidar In-space Technology Experiment," ed.

[22] P. E. Ross, "Cheap Lidar for Automatic Braking," ed.

[23] C. W. Hsu, T. H. Hsu, and K. J. Chang, "Implementation of car-following system using LiDAR detection," pp. 165-169.
[24] F. Gibert, P. H. Flamant, D. Bruneau, and C. Loth, "Two-micrometer heterodyne differential absorption lidar measurements of the atmospheric CO2 mixing ratio in the boundary layer," *Appl. Opt.,* vol. 45, pp. 4448-4458, 2006.
[25] U. N. Singh, J. Yu, M. Petros, T. F. Refaat, R. G. Remus, J. J. Fay*, et al.*, "Airborne 2-micron double-pulsed integrated path differential absorption lidar for column CO2 measurement," pp. 924602-924611.
[26] J. Yu, M. Petros, S. Chen, Y. Bai, P. J. Petzar, B. C. Trieu*, et al.*, "A two micron coherent differential absorption lidar development," pp. 786006-786006.
[27] T. F. Refaat, S. Ismail, G. J. Koch, L. Diaz, K. Davis, and M. Rubio, "Field Testing of a Two-Micron DIAL System for Profiling Atmospheric Carbon Dioxide."
[28] S. Upendra, Y. Jirong, P. Mulugeta, T. Refaat, R. Remus, F. James J*, et al.*, "Airborne Pulsed 2-Micron Direct Detection Lidar for CO2 Column Measurement," ed.
[29] S. Ismail, G. Koch, N. Abedin, T. Refaat, M. Rubio, and U. Singh, "Development of Laser, Detector, and Receiver Systems for an Atmospheric CO2 Lidar Profiling System," pp. 1-7.
[30] T. F. Refaat, M. N. Abedin, O. V. Sulima, S. Ismail, and U. N. Singh, "AlGaAsSb/InGaAsSb phototransistors for 2-μm remote sensing applications," *Optical Engineering,* vol. 43, pp. 1647-1650, 2004.
[31] J. Yu, B. C. Trieu, E. A. Modlin, U. N. Singh, M. J. Kavaya, S. Chen*, et al.*, "1 J/pulse Q-switched 2 μm solid-state laser," *Opt. Lett.,* vol. 31, pp. 462-464, 2006.
[32] P. F. Ambrico, A. Amodeo, P. D. Girolamo, and N. Spinelli, "Sensitivity analysis of differential absorption lidar measurements in the mid-infrared region," *Appl. Opt.,* vol. 39, pp. 6847-6865, 2000.
[33] M. Uchiumi, N. J. Vasa, M. Fujiwara, S. Yokoyama, M. Maeda, and O. Uchino, "Development of DIAL for CO2 and CH4 in the atmosphere," pp. 141-149.
[34] G. J. Koch, B. W. Barnes, M. Petros, J. Y. Beyon, F. Amzajerdian, J. Yu*, et al.*, "Coherent differential absorption lidar measurements of CO2," *Appl. Opt.,* vol. 43, pp. 5092-5099, 2004.
[35] A. K. Dharmadhikari, H. Bharambe, J. A. Dharmadhikari, J. S. D'Souza, and D. Mathur, "DNA Damage by OH Radicals Produced Using Intense, Ultrashort, Long Wavelength Laser Pulses," *Phys. Rev. Lett.,* vol. 112, pp. 138105-138105, 2014.
[36] J. D. Spinhirne, "Micro pulse lidar," *Geoscience and Remote Sensing, IEEE Transactions on,* vol. 31, pp. 48-55, 1993.
[37] X. Zhou, X. Meng, A. B. Krysa, J. R. Willmott, J. S. Ng, and C. H. Tan, "InAs Photodiodes for 3.43 μm Radiation Thermometry," *Sensors Journal, IEEE,* vol. 15, pp. 5555-5560, 2015.
[38] A. R. J. Marshall, P. Vines, S. Xie, J. P. R. David, and C. H. Tan, "High gain InAs electron-avalanche photodiodes for optical communication," pp. 1-4.
[39] "Nobel Lectures,Nobelprize.org. Nobel Media AB 2014. Web. 15 Nov 2015," ed.
[40] R. E. Franklin and R. G. Gosling, "Molecular Configuration in Sodium Thymonucleat," *Nature,* vol. 171, pp. 740-741, 1953.

[41] J. D. Watson and F. H. C. Crick, "Molecular Structure of Nucleic Acids: A Structure for Deoxyribose Nucleic Acid," *Nature,* vol. 171, pp. 737-738, 1953.
[42] B. M. Swinyard, K. H. Joy, B. J. Kellett, I. A. Crawford, M. Grande, C. J. Howe*, et al.*, "X-ray fluorescence observations of the moon by SMART-1/D-CIXS and the first detection of Ti Kα from the lunar surface," *Planetary and Space Science,* vol. 57, pp. 744-750, 6// 2009.
[43] J. O. Goldsten, "The x-ray/gamma-ray spectrometer on the near earth asteroid rendezvous mission," *Space Science Reviews,* vol. 82, pp. 169-216, 1997.
[44] I. Adler, J. Trombka, J. Gerard, P. Lowman, R. Schmadebeck, H. Blodget*, et al.*, "Apollo 15 geochemical x-ray fluorescence experiment: Preliminary report," *Science,* vol. 175, pp. 436-440, 1972.
[45] M. Grande, B. J. Kellett, C. Howe, C. H. Perry, B. Swinyard, S. Dunkin*, et al.*, "The D-CIXS X-ray spectrometer on the SMART-1 mission to the Moon—First results," *Planetary and Space Science,* vol. 55, pp. 494-502, 3// 2007.
[46] P. P. Webb and R. J. McIntyre, "Large Area Reach-Through Avalanche Diodes for X-Ray Spectroscopy," *Nuclear Science, IEEE Transactions on,* vol. 23, pp. 138-144, 1976.
[47] M. R. Squillante, R. Farrell, J. C. Lund, F. Sinclair, G. Entine, and K. R. Keller, "Avalanche Diode Low Energy X-Ray and Nuclear Particle Detector," *Nuclear Science, IEEE Transactions on,* vol. 33, pp. 336-339, 1986.
[48] E. M. Gullikson, E. Gramsch, and M. Szawlowski, "Large-area avalanche photodiodes for the detection of soft x rays," *Appl. Opt.,* vol. 34, pp. 4662-4668, 1995.
[49] M. Moszyński, M. Kapusta, M. Balcerzyk, M. Szawlowski, and D. Wolski, "Large Area Avalanche Photodiodes in X-rays and scintillation detection," *Nuclear Instruments and Methods in Physics Research Section A: Accelerators, Spectrometers, Detectors and Associated Equipment,* vol. 442, pp. 230-237, 2000.
[50] M. Moszynski, M. Kapusta, J. Zalipska, M. Balcerzyk, D. Wolski, M. Szawlowski*, et al.*, "Low energy gamma;-ray scintillation detection with large area avalanche photodiodes," pp. 142-147 vol.1.
[51] R. B. Gomes, C. H. Tan, X. Meng, J. P. R. David, and J. S. Ng, "GaAs/Al0.8Ga0.2As avalanche photodiodes for soft X-ray spectroscopy," *Journal of Instrumentation,* vol. 9, pp. P03014-P03014, 2014.
[52] "www.minicircuits.com," ed.
[53] S. B. Alexander, *Optical Communication Receiver Design*: SPIE, 1997.
[54] E. Sackinger, "The Transimpedance Limit," *IEEE Transactions on Circuits and Systems I: Regular Papers,* vol. 57, pp. 1848-1856, 2010.
[55] E. Gatti and P. F. Manfredi, "Processing the signals from solid-state detectors in elementary-particle physics," *La Rivista del Nuovo Cimento,* vol. 9, pp. 1-146, 2008.
[56] Ortec, "Preamplifier Introduction," ed, 2009.
[57] G. Bertuccio, P. Rehak, and D. Xi, "A novel charge sensitive preamplifier without the feedback resistor," *Nuclear Instruments and Methods in Physics Research Section A: Accelerators, Spectrometers, Detectors and Associated Equipment,* vol.

326, pp. 71-76, 1993.
[58] D. A. Landis, C. P. Cork, N. W. Madden, and F. S. Goulding, "Transistor Reset Preamplifier for High Rate High Resolution Spectroscopy," *IEEE Transactions on Nuclear Science,* vol. 29, pp. 619-624, 1982.
[59] D. A. Landis, N. W. Madden, and F. S. Goulding, "Bipolar pulsed reset for AC coupled charge-sensitive preamplifiers," pp. 887-891 vol.1.
[60] M. Dahoumane, D. Dauvergne, J. Krimmer, H. Mathez, C. Ray, E. Testa*, et al.*, "A low noise and high dynamic charge sensitive amplifier-shaper associated with Silicon Strip Detector for compton camera in hadrontherapy," pp. 1445-1451.
[61] X. Wei, Z. Wang, and H. Xu, "A Low-Noise, Wideband CMOS Charge Sensitive Preamplifier for the High Precision Pixel Detector," *INTERNATIONAL JOURNAL ON Advances in Information Sciences and Service Sciences,* vol. 4, pp. 99-105, 2012.
[62] J. F. Pratte, G. De Geronimo, S. Junnarkar, P. O'Connor, Y. Bo, S. Robert*, et al.*, "Front-end electronics for the RatCAP mobile animal PET scanner," *IEEE Transactions on Nuclear Science,* vol. 51, pp. 1318-1323, 2004.
[63] C. Fiorini, "A charge sensitive preamplifier for high peak stability in spectroscopic measurements at high counting rates," *IEEE Transactions on Nuclear Science,* vol. 52, pp. 1603-1610, 2005.
[64] A. Pullia and F. Zocca, "An auto-zero charge preamplifier with discharge mechanism for ionising radiation sensors," pp. 2084-2086.
[65] P. O'Connor and G. De Geronimo, "Prospects for charge sensitive amplifiers in scaled CMOS," *Nuclear Instruments and Methods in Physics Research Section A: Accelerators, Spectrometers, Detectors and Associated Equipment,* vol. 480, pp. 713-725, 2002.
[66] "Cremat: Detect pulses above the noise," ed.
[67] "A250CF CoolFET Charge Sensitive Preamplifier," ed.
[68] R. Bassini, C. Boiano, and A. Pullia, "A low-noise charge amplifier with fast rise time and active discharge mechanism," *IEEE Transactions on Nuclear Science,* vol. 49, pp. 2436-2439, 2002.
[69] T. V. Blalock, "A Low-Noise Charge-Sensitive Preamplifier with a Field-Effect Transistor in the Input Stage," *IEEE Transactions on Nuclear Science,* vol. 11, pp. 365-372, 1964.
[70] V. Radeka, "Signal, Noise and Resolution in Position-Sensitive Detectors," *IEEE Transactions on Nuclear Science,* vol. 21, pp. 51-64, 1974.
[71] M. Sampietro, L. Fasoli, E. Gatti, C. Guazzoni, A. Fazzi, P. Lechner*, et al.*, "Bipolar feedback transistor integrated on detector with JFET for continuous reset," *Nuclear Instruments and Methods in Physics Research Section A: Accelerators, Spectrometers, Detectors and Associated Equipment,* vol. 439, pp. 368-372, 2000.
[72] O. V. Ignatyev, A. I. Kosse, A. D. Pulin, Y. A. Shevchenko, and N. F. Shkola, "An updated system of electronic modules for X-ray spectrometers with cooled semiconductor detectors," *Nuclear Instruments and Methods in Physics Research Section A: Accelerators, Spectrometers, Detectors and Associated Equipment,* vol. 282, pp. 734-738, 1989.

[73] C. L. Britton, T. H. Becker, T. J. Paulus, and R. C. Trammell, "Characteristics of High-Rate Energy Spectroscopy Systems Using HPGe Coaxial Detectors and Time-Variant Filters," *IEEE Transactions on Nuclear Science,* vol. 31, pp. 455-460, 1984.
[74] D. A. Landis, F. S. Goulding, R. H. Pehl, and J. T. Walto, "Pulsed Feedback Techniques for Semicondctor Detector Radiation Spectrometers," *IEEE Transactions on Nuclear Science,* vol. 18, pp. 115-124, 1971.
[75] V. Radeka, "Overload Recovery Circuit for Charge Amplifiers," *IEEE Transactions on Nuclear Science,* vol. 17, pp. 269-275, 1970.
[76] F. S. Goulding, J. Walton, and D. F. Malone, "An opto-electronic feedback preamplifier for high-resolution nuclear spectroscopy," *Nuclear Instruments and Methods,* vol. 71, pp. 273-279, 1969.
[77] F. S. Goulding and D. A. Landis, "Signal Processing for Semiconductor Detectors," *IEEE Transactions on Nuclear Science,* vol. 29, pp. 1125-1141, 1982.
[78] D. A. Landis, N. W. Madden, and F. S. Goulding, "Energy-Dependent Losses in Pulsed-Feedback Preamplifiers," *IEEE Transactions on Nuclear Science,* vol. 26, pp. 428-432, 1979.
[79] F. S. Goulding and D. A. Landis, "Some Electronic Aspects of Energy Measurements with Solid-State Detectors," *IEEE Transactions on Nuclear Science,* vol. 25, pp. 896-901, 1978.
[80] F. S. Goulding, J. T. Walton, and R. H. Pehl, "Recent Results on the Optoelectronic Feedback Preamplifier," *IEEE Transactions on Nuclear Science,* vol. 17, pp. 218-225, 1970.
[81] E. Funck, "Counting losses from pulsed optical-feedback preamplifiers used with semiconductor detectors," *The International Journal of Applied Radiation and Isotopes,* vol. 34, pp. 1123-1131, 1983.
[82] E. Elad, "Drain Feedback - A Novel Feedback Technique for Low-Noise Cryogenic Preamplifiers," *IEEE Transactions on Nuclear Science,* vol. 19, pp. 403-411, 1972.
[83] V. Radeka, "Charge Amplification without Charge Leak Resistor," *IEEE Transactions on Nuclear Science,* vol. 17, pp. 433-439, 1970.
[84] G. Bertuccio and A. Pullia, "Room temperature X-ray spectroscopy with a silicon diode detector and an ultra low noise preamplifier," *IEEE Transactions on Nuclear Science,* vol. 41, pp. 1704-1709, 1994.
[85] A. Pullia, H. W. Kraner, D. P. Siddons, L. R. Furenlid, and G. Bertuccio, "Silicon detector system for high rate EXAFS application," pp. 463-467 vol.1.
[86] A. Fazzi, P. Jalas, P. Rehak, and P. Holl, "Charge-sensitive amplifier front-end with an nJFET and a forward-biased reset diode," *IEEE Transactions on Nuclear Science,* vol. 43, pp. 3218-3222, 1996.
[87] H. P. K. K, *Photomultiplier Tubes: Basics and Applications, 3rd ed*: Hamamatsu Photonics K. K., 2006.
[88] M. Riordan and L. Hoddeson, "The origins of the pn junction," *Spectrum, IEEE,* vol. 34, pp. 46-51, 1997.
[89] J. Kataoka, T. Saito, Y. Kuramoto, T. Ikagawa, Y. Yatsu, J. Kotoku*, et al.*, "Recent progress of avalanche photodiodes in high-resolution X-rays and -rays detection,"

Nuclear Instruments and Methods in Physics Research Section A: Accelerators, Spectrometers, Detectors and Associated Equipment, vol. 541, pp. 398-404, 2005.

[90] T. Nakamori, T. Enomoto, T. Toizumi, K. Tokoyoda, Y. Yatsu, N. Kawai*, et al.*, "Development of X-ray/gamma-ray imaging spectrometers using reach-through APD arrays," *Journal of Instrumentation,* vol. 7, pp. C03038-C03038, 2012.

[91] Y. Yatsu, Y. Kuramoto, J. Kataoka, J. Kotoku, T. Saito, T. Ikagawa*, et al.*, "Study of avalanche photodiodes for soft X-ray detection below 20keV," *Nuclear Instruments and Methods in Physics Research Section A: Accelerators, Spectrometers, Detectors and Associated Equipment,* vol. 564, pp. 134-143, 2006.

[92] S. Tanaka, J. Kataoka, Y. Kanai, Y. Yatsu, M. Arimoto, M. Koizumi*, et al.*, "Development of wideband X-ray and gamma-ray spectrometer using transmission-type, large-area APD," *Nuclear Instruments and Methods in Physics Research Section A: Accelerators, Spectrometers, Detectors and Associated Equipment,* vol. 582, pp. 562-568, 2007.

[93] G. F. Knoll, *Radiation detection and measurement*: Wiley, 2000.

[94] A. Owens and A. Peacock, "Compound semiconductor radiation detectors," *Nuclear Instruments and Methods in Physics Research Section A: Accelerators, Spectrometers, Detectors and Associated Equipment,* vol. 531, pp. 18-37, 2004.

[95] U. Fano, "Ionization Yield of Radiations. II. The Fluctuations of the Number of Ions," *Physical Review,* vol. 72, pp. 26-29, 1947.

[96] G. Fraser, *X-ray Detectors in Astronomy*, 1989.

[97] G. Bertuccio, A. Pullia, and G. De Geronimo, "Criteria of choice of the front-end transistor for low-noise preamplification of detector signals at sub-microsecond shaping times for X- and γ-ray spectroscopy," *Nuclear Instruments and Methods in Physics Research Section A: Accelerators, Spectrometers, Detectors and Associated Equipment,* vol. 380, pp. 301-307, 1996.

[98] E. Gatti, P. F. Manfredi, M. Sampietro, and V. Speziali, "Suboptimal filtering of 1/ƒ-noise in detector charge measurements," *Nuclear Instruments and Methods in Physics Research Section A: Accelerators, Spectrometers, Detectors and Associated Equipment,* vol. 297, pp. 467-478, 1990.

[99] F. M. Klaassen, "Characterization of low 1/f noise in MOS transistors," *IEEE Transactions on Electron Devices,* vol. 18, pp. 887-891, 1971.

[100] V. Radeka, "State of the Art of Low Noise Amplifiers for Semiconductor Radiation Detector," *Proceedings of International symposium on Nuclear Electronics,* pp. 46-46, 1968.

[101] G. Bertuccio, L. Fasoli, C. Fiorini, and M. Sampietro, "Spectroscopy charge amplifier for detectors with integrated front-end FET," *IEEE Transactions on Nuclear Science,* vol. 42, pp. 1399-1405, 1995.

[102] A. Van Der Ziel, "Gate noise in field effect transistors at moderately high frequencies," *Proceedings of the IEEE,* vol. 51, pp. 461-467, 1963.

[103] G. V. Pallottino and A. E. Zirizzotti, "Noise measurements on junction field effect transistors," *Review of Scientific Instruments,* vol. 65, 1994.

[104] G. Bertuccio, A. Pullia, J. Lauter, A. Forster, and H. Luth, "Pixel X-ray detectors in

epitaxial gallium arsenide with high-energy resolution capabilities (Fano factor experimental determination)," *IEEE Transactions on Nuclear Science,* vol. 44, pp. 1-5, 1997.
[105] G. C. Sun, M. Lenoir, E. Breelle, H. Samic, J. C. Bourgoin, H. El-Abbassi*, et al.*, "X-ray detector with thick epitaxial GaAs grown by chemical reaction," pp. 362-365 vol.1.
[106] M. Alietti, C. Canali, A. Castaldini, A. Cavallini, A. Cetronio, C. Chiossi*, et al.*, "Performance of a new ohmic contact for GaAs particle detectors," *Nuclear Instruments and Methods in Physics Research Section A: Accelerators, Spectrometers, Detectors and Associated Equipment,* vol. 362, pp. 344-348, 1995.
[107] G. Bertuccio and A. Pullia, "An HEMT input charge preamplifier for nanoseconds signal processing time," *IEEE Transactions on Nuclear Science,* vol. 42, pp. 66-72, 1995.
[108] G. Bertuccio, G. de Geronimo, A. Longoni, and A. Pullia, "Low frequency gate current noise in high electron mobility transistors: experimental analysis," *IEEE Electron Device Letters,* vol. 16, pp. 103-105, 1995.
[109] G. Bertuccio, M. Cordoni, L. Fasoli, and M. Sampietro, "Low-power low-noise BJT amplifier for nuclear applications," pp. 470-473 vol.1.
[110] A. Pullia and G. Bertuccio, "Resolution limits of silicon detectors and electronics for soft X-ray spectroscopy at non cryogenic temperatures," *Nuclear Instruments and Methods in Physics Research Section A: Accelerators, Spectrometers, Detectors and Associated Equipment,* vol. 380, pp. 1-5, 1996.
[111] W. Shockley, "Problems related to p-n junctions in silicon," *Czechoslovak Journal of Physics,* vol. 11, pp. 81-121, 1961.
[112] S. M. Sze and K. K. Ng, *Physics of Semiconductor Devices, 3rd Edition*: Wiley, 2006.
[113] Texas Instrument, "LMH6624 and LMH6626 Single/Dual Ultra Low Noise Wideband Operational Amplifier (Rev. G)," 2011.
[114] Texas Instrument, "LMH6702 1.7-GHz Ultra-Low Distortion Wideband Op Amp," November 2002.
[115] Texas Instrument, "LMH6733 Single Supply, 1.0 GHz, Triple Operational Amplifier," January 2002.
[116] Texas Instrument, "LMH6629 Ultra-Low Noise, High-Speed Operational Amplifier with Shutdown," APRIL 2010.
[117] Texas Instrument, "LMP7717, 88 MHz, Precision, Low Noise, 1.8V CMOS Input, Decompensated Operational Amplifier," MARCH 2007.
[118] MAXIM, "MAX4225, 1GHz, Low-Power, SOT23, Current-Feedback Amplifiers with Shutdown," 1997.
[119] Intersil, "EL2125C, Ultra-Low Noise, Low Power, Wideband Amplifier," May 2007.
[120] Intersil, "EL5166, 1.4GHz Current Feedback Amplifiers with Enable," September 2010.
[121] Texas Instrument, "THS3202, 2-GHz, LOW DISTORTION, DUAL CURRENT-FEEDBACK AMPLIFIERS," January 2010.
[122] Analog Devices Inc, "AD8432, Dual-Channel Ultralow Noise Amplifier with Selectable Gain and Input Impedance," 2010.

[123] Analog Devices Inc, "AD8003, Triple, 1.5 GHz Op Amp," 2014.
[124] Analog Devices Inc, "ADA4899-1, Unity-Gain Stable, Ultralow Distortion,1 nV/Hz Voltage Noise, High Speed Op Amp," 2014.
[125] Texas Instrument, "OPA695 Ultra-Wideband, Current-Feedback Operational Amplifier With Disable," 2011.
[126] Texas Instrument, "OPA3691 Triple Wideband, Current-Feedback OPERATIONAL AMPLIFIER With Disable," 2008.
[127] Intersil, "EL5130 300MHz Low Noise Amplifiers," 2010.
[128] J. E. Green, J. P. R. David, and R. C. Tozer, "A transimpedance amplifier for excess noise measurements of high junction capacitance avalanche photodiodes," *Measurement Science and Technology,* vol. 23, pp. 125901-125901, 2012.
[129] F. Z. Xie, D. Kuhl, E. H. Böttcher, S. Y. Ren, and D. Bimberg, "Wide-band frequency response measurements of photodetectors using low-level photocurrent noise detection," *Journal of Applied Physics,* vol. 73, p. 8641, 1993.
[130] H. Ando and H. Kanbe, "Ionization coefficient measurement in GaAs by using multiplication noise characteristics," *Solid-State Electronics,* vol. 24, pp. 629-634, 1981.
[131] M. C. Brain, "Characterization and estimated performance of commercial n+-p Ge APDs for long-wavelength optical receivers," *Optical and Quantum Electronics,* vol. 13, pp. 353-367, 1981.
[132] K. S. Lau, C. H. Tan, B. K. Ng, K. F. Li, R. C. Tozer, J. P. R. David*, et al.*, "Excess noise measurement in avalanche photodiodes using a transimpedance amplifier front-end," *Measurement Science and Technology,* vol. 17, pp. 1941-1941, 2006.
[133] G. Bertuccio and P. Rehak, "Low noise charge sensitive preamplifier DC stabilized without a physical resistor," ed: Google Patents, 1994.
[134] M. Beikahmadi and S. Mirabbasi, "A low-power low-noise CMOS charge-sensitive amplifier for capacitive detectors," pp. 450-453.
[135] O. Gevin, A. Michalowska, O. Limousin, C. S. Tindall, S. Dubos, D. Renaud*, et al.*, "Low power, low noise, Charge Sensitive Amplifier in CMOS 0.18 $µm$ technology for the readout of fine pitch pixelated CdTe detector," pp. 848-853.
[136] P. O'Connor, G. Gramegna, P. Rehak, F. Corsi, and C. Marzocca, "CMOS preamplifier with high linearity and ultra low noise for X-ray spectroscopy," *IEEE Transactions on Nuclear Science,* vol. 44, pp. 318-325, 1997.
[137] G. Bertuccio and S. Caccia, "Progress in ultra-low-noise ASICs for radiation detectors," *Nuclear Instruments and Methods in Physics Research Section A: Accelerators, Spectrometers, Detectors and Associated Equipment,* vol. 579, pp. 243-246, 8/21/ 2007.
[138] L. Fasoli, C. Fiorini, and G. Bertuccio, "Feedback stability of charge amplifiers with continuous reset through forward-biased diode junctions," *IEEE Transactions on Nuclear Science,* vol. 43, pp. 2358-2364, 1996.
[139] D. S. McGregor and H. Hermon, "Room-temperature compound semiconductor radiation detectors," *Nucl. Instrum. Meth. A,* vol. 395, pp. 101-101, 1997.
[140] P. J. Sellin, "Recent advances in compound semiconductor radiation detectors,"

Nucl. Instrum. Meth. A, vol. 513, pp. 332-332, 2003.
[141] G. Bertuccio, R. Casiraghi, A. Cetronio, C. Lanzieri, and F. Nava, "Silicon carbide for high resolution {X}-ray detectors operating up to 100°{C}," *Nucl. Instrum. Meth. A,* vol. 552, pp. 413-413, 2004.
[142] G. Bertuccio, S. Caccia, D. Puglisi, and D. Macera, "Advances in silicon carbide X-ray detectors," *Nuclear Instruments and Methods in Physics Research Section A: Accelerators, Spectrometers, Detectors and Associated Equipment,* vol. 652, pp. 193-196, 2011.
[143] C. H. Tan, R. B. Gomes, J. P. R. David, A. M. Barnett, D. J. Bassford, J. E. Lees*, et al.*, "Avalanche Gain and Energy Resolution of Semiconductor X-ray Detectors," *IEEE Trans. Electron Dev.,* vol. 58, pp. 1696-1696, 2011.
[144] J. S. Cheong, J. S. L. Ong, J. S. Ng, A. B. Krysa, and J. P. R. David, "Al0. 52In0.48P SAM-APD as a Blue-Green Detector," vol. 20, pp. 0-4, 2014.
[145] A. Owens, *Compound Semiconductor Radiation Detectors*: CRC Press, 2016.
[146] M. Achouche, G. Glastre, C. Caillaud, M. Lahrichi, M. Chtioui, and D. Carpentier, "InGaAs Communication Photodiodes: From Low- to High-Power-Level Designs," *IEEE Photonics Journal,* vol. 2, pp. 460-468, 2010.
[147] D. S. Franco, K. Vaccaro, W. R. Clark, W. A. Teynor, H. M. Dauplaise, M. Roland*, et al.*, "High-performance InGaAs-InP APDs on GaAs," *IEEE Photonics Technology Letters,* vol. 17, pp. 873-874, 2005.
[148] M. Lahrichi, E. Derouin, D. Carpentier, N. Lagay, J. Decobert, G. Glastre*, et al.*, "Very low dark current AlInAs/GaInAs SAGM avalanche photodiodes for 10Gb/s applications," pp. 1-2.
[149] B. Li, Q.-Q. Lv, R. Cui, W.-H. Yin, X.-H. Yang, and Q. Han, "A Low Dark Current Mesa-Type InGaAs/InAlAs Avalanche Photodiode," *IEEE Photonics Technology Letters,* vol. 27, pp. 34-37, 2015.
[150] A. D. Holland, A. D. T. Short, and T. Cross, "X-ray detection using bulk GaAs," *Nuclear Instruments and Methods in Physics Research Section A: Accelerators, Spectrometers, Detectors and Associated Equipment,* vol. 346, pp. 366-371, 1994/07/15 1994.
[151] J. H. Hubbell and S. M. Seltzer, "Tables of X-Ray Mass Attenuation Coefficients and Mass Energy-Absorption Coefficients," *National Institute of Standards and Technology,* 2004.
[152] C. H. Tan, R. B. Gomes, J. P. R. David, A. M. Barnett, D. J. Bassford, J. E. Lees*, et al.*, "Avalanche Gain and Energy Resolution of Semiconductor {X}-ray Detectors," *IEEE Trans. Electron Dev.,* vol. 58, pp. 1696-1696, 2011.
[153] B. K. Ng, J. P. R. David, S. A. Plimmer, R. C. Tozer, G. J. Rees, and M. Hopkinson, "Al0.8Ga0.2As: a very low excess noise multiplication medium for avalanche photodiodes," *IEE Proceedings - Optoelectronics,* vol. 148, pp. 243-246, 2001.
[154] L. M. P. Fernandes, F. D. Amaro, A. Antognini, J. M. R. Cardoso, C. A. N. Conde, O. Huot*, et al.*, "Characterization of large area avalanche photodiodes in X-ray and VUV-light detection," *Journal of Instrumentation,* vol. 2, p. P08005, 2007.
[155] A. L. Gouvea, A. Antognini, F. Kottmann, R. Pohl, and L. M. P. Fernandes, "Reach-

Through Avalanche Photodiodes in Soft X-ray Detection," *IEEE Transactions on Nuclear Science,* vol. 61, pp. 2419-2424, 2014.

[156] G. Bertuccio, R. Casiraghi, D. Maiocchi, A. Owens, M. Bavdaz, A. Peacock*, et al.*, "Noise analysis of gallium arsenide pixel X-ray detectors coupled to ultra-low noise electronics," *IEEE Transactions on Nuclear Science,* vol. 50, pp. 723-728, 2003.

[157] J. S. Ng, X. Meng, J. E. Lees, A. Barnett, and C. H. Tan, "Fabrication study of GaAs mesa diodes for X-ray detection," *Journal of Instrumentation,* vol. 9, pp. T08005-T08005, 2014.

[158] G. Lioliou, X. Meng, J. S. Ng, and A. M. Barnett, "Characterization of gallium arsenide X-ray mesa p-i-n photodiodes at room temperature," *Nuclear Instruments and Methods in Physics Research Section A: Accelerators, Spectrometers, Detectors and Associated Equipment,* vol. 813, pp. 1-9, 3/21/ 2016.